NASA CONTRACTOR REPORT

NASA CR-649

FLIGHT TEST AERODYNAMIC HEATING DATA FOR THE AFTERBODY OF THE PROJECT MERCURY SPACECRAFT WITH COMPARISONS TO AVAILABLE PREDICTION METHODS

by J. D. Murphy

Prepared by
LOCKHEED MISSILES AND SPACE COMPANY
Sunnyvale, Calif.
for Manned Spacecraft Center

NATIONAL AERONAUTICS AND SPACE ADMINISTRATION • WASHINGTON, D. C. • JUNE 1967

NASA CR-649

FLIGHT TEST AERODYNAMIC HEATING DATA FOR THE AFTERBODY OF THE PROJECT MERCURY SPACECRAFT WITH COMPARISONS TO AVAILABLE PREDICTION METHODS

By J. D. Murphy

Prepared under Contract No. NAS 9-3531 by
LOCKHEED MISSILES AND SPACE COMPANY
Sunnyvale, Calif.

for Manned Spacecraft Center

NATIONAL AERONAUTICS AND SPACE ADMINISTRATION

For sale by the Clearinghouse for Federal Scientific and Technical Information
Springfield, Virginia 22151 – CFSTI price $3.00

ABSTRACT

Afterbody heating experienced by the Project Mercury Spacecraft during reentry is determined from skin temperature measurements obtained in four flights. Measured skin temperature histories and inferred heating rate histories are presented in tabular and graphical form. Dimensionless heat transfer parameters are computed and compared with the theoretical predictions of Denison, Baum, and King and of Chapman.

It is found that the laminar data can be correlated by an expression of the form

$$St \propto Re_x^{-3/4}$$

The flight test data is in good agreement with the above correlation for Reynolds numbers based on wetted length less than 2×10^4. For Reynolds numbers larger than 2×10^4 the experimental data gives strong indication of transitional flow.

FLIGHT TEST AERODYNAMIC HEATING DATA FOR THE AFTERBODY OF THE PROJECT MERCURY SPACECRAFT WITH COMPARISONS TO AVAILABLE PREDICTION METHODS

By J. D. Murphy

SUMMARY

Afterbody heating experienced by the Project Mercury Spacecraft during reentry has been inferred from temperature measurements obtained in four flights.

The afterbody heating rates and measured temperatures are tabulated as functions of time for the four flights considered. The data reduction procedure is described and the results obtained are compared with the theory of Chapman (ref. 1) and the theory of Denison, Baum, and King (refs. 2-4).

It is concluded that available theories for heating from a free shear layer are sufficiently accurate for order of magnitude estimates but that substantial improvements in prediction methods are required if optimum afterbody thermal protection systems are to be designed.

INTRODUCTION

With the completion of Project Mercury and the advent of the Gemini and Apollo programs the technology of man-rated systems must be extended to the far more severe environment associated with reentry at super-orbital velocities. As the environment becomes more severe new problems appear and the problems which, for orbital or ballistic entry, were amenable to approximate analysis, require more sophisticated techniques. Figuring prominently in this latter category is the problem of predicting aerodynamic heating in the base region of blunt reentry bodies. The present study is directed to the evaluation and presentation of afterbody heat transfer data obtained from four Project Mercury flights. It is believed that the information presented may prove useful in the evaluation of future afterbody thermal protection systems and in the verification of new theoretical procedures for the prediction of afterbody heating.

These data are believed to be the first flight test data for separated heat transfer in the reentry environment to receive broad dissemination. To aid the reader in interpretation of these results, the data are compared with applicable theories.

In order to give the information presented here the widest possible applicability the results are presented in three different forms: first the skin temperature histories are presented in tabular form, second the local heating rate histories are presented in tabular and graphical form, and finally the non-dimensional heating rates, St vs Re_x, are presented in graphical form. Sufficient information on the vehicle configuration and instrumentation system is presented in the text to permit interpretation of the results, and detailed discussions of the data reduction and prediction techniques are presented in the appendices.

SYMBOLS

A	area
a_i	coefficient in curve fit
B'	blowing parameter $\rho_w V_w / C_H$
C_f	local skin friction coefficient
C_H	local heat transfer coefficient
D	major body diameter
F_D	shear function evaluated on dividing streamline
F_{i-j}	radiation interchange factor
H	total enthalpy
h	static enthalpy
k	shock density ratio ρ_∞ / ρ_{ST} or thermal conductivity
ℓ	$\rho_D \mu_D / \rho_e \mu_e$
ℓ_2	distance aft of sphere-cone junction
M	Mach number
P	pressure
Pr	Prandtl number

q	local instantaneous heating rate
R_N	nose radius of curvature
r	radial coordinate
Re_x	Reynolds number based on boundary layer edge conditions and distance from stagnation point
S	distance from stagnation point
S_b	distance from stagnation point to separation point
St	Stanton number
T	temperature
u	streamwise velocity
v	normal velocity
Y	$\int \rho_e u_e \frac{\rho}{\rho_e} r \, dy$
y	distance from wall
β^*	angle between stagnation point and sonic point measured at the nose cap center of curvature
δ	increment of thickness
ϵ_i	emissivity of surface i
θ	time from launch
θ_o	base time chosen at a nominal vehicle altitude of 400,000 ft.
μ	viscosity
ρ	density
σ	Stefan-Boltzmann constant

Subscripts

b	base conditions
c	evaluated in recirculation region

D	evaluated on dividing streamline
e	evaluated at boundary layer edge
ST	evaluated at stagnation conditions
TR	evaluated at transition point
W	evaluated at wall conditions
∞	evaluated at free stream conditions

Superscripts

*	properties evaluated at reference enthalpy
-	evaluated just upstream of wall temperature discontinuity
+	evaluated just downstream of wall temperature discontinuity

VEHICLE CONFIGURATION, INSTRUMENTATION, AND TRAJECTORIES

Vehicle Configuration and Instrumentation

The general configuration of the Project Mercury Capsule is shown in figure 1. This vehicle can be described as a rearward facing 20° half angle cone terminated at the forward end by an 80 inch radius of curvature spherical segment and terminated at the aft end by a 32 inch cylindrical section 20 inches long. At the aft end of the cylindrical section the recovery cannister is attached. The recovery cannister is a 24 inch long truncated cone tapering from 24 inches at the base to 20 inches at the aftmost end.

The forward spherical segment is thermally protected by a phenolic-fiberglass ablating heat shield. The conical portion is covered with 0.016 inch Rene 41 shingles operating near radiation equilibrium, and the cylindrical surfaces are protected by a 0.22 inch thick beryllium heat sink. The afterbody skin is thermally isolated from the internal structure by thick blankets of fiberglass insulation and well designed supports and fasteners.

The afterbody instrumentation consisted of several chromel-alumel thermocouples affixed to the inner surface of the outer skin of the spacecraft. The number and locations of these thermocouples are shown for the several vehicles in figures 2a through 2d. The numbers shown adjacent to the thermocouple locations on these figures refer to the telemetry channels from which the appropriate temperature histories were obtained. Figure 3 shows a typical thermocouple installation on the inner surface of the 0.016 inch Rene 41 shingles. It should be noted that the thermocouple tiedown clamps were fabricated from 0.020" x 0.25" x 1.0" stainless steel strips.

The large thermal mass of these clamps together with that of the thermocouple leads causes a substantial perturbation in the temperature field. The effect of this distortion of the temperature field will be discussed in subsequent sections of this report.

Vehicle Trajectories

Mercury-Atlas No. 2 (MA-2) was launched from Cape Canaveral on February 21, 1962. The trajectory was chosen to produce maximum afterbody temperatures and near maximum loads. The trajectory of MA-2 was a ballistic trajectory with an apogee of about 100 nautical miles and a range of 1257 nautical miles. Figure 4a shows the velocity and altitude histories of vehicle MA-2 during the reentry portion of the trajectory. Time zero for this and subsequent figures has been arbitrarily chosen as the time the vehicle is at a nominal altitude of 400,000 feet.

The trajectories of MA-5 and MA-8 were virtually identical during the reentry phase. Mercury-Atlas No. 5 was launched from Cape Canaveral on November 29, 1961. The flight was for two orbits. Figure 4b shows the velocity and altitude histories during the reentry portion of the trajectory.

Mercury-Atlas No. 8 (MA-8) was launched on October 3, 1962. The flight was a manned 6 orbit mission. The velocity and altitude histories for this flight were virtually identical with those of MA-5 and are shown superimposed on the MA-5 histories in figure 4b.

Mercury-Atlas No. 7 (MA-7) was launched from Cape Canaveral on May 24, 1962. The flight was a manned 3 orbit mission. Altitude and velocity histories for this mission are presented in figure 4c.

Table 1 presents certain other parameters of interest in interpreting reentry heating data. Of particular interest is the large angle of attack, i.e., 12.5°, noted on MA-2.

Table 1.-Entry parameters

Vehicle ID	Velocity at 400 KFT ft/sec	Roll Rate* deg/sec	Angle of Attack at Max Dynamic Pressure deg
MA-2	17900	10	12.5
MA-5	24200	9.5	0
MA-7	24200	10	0
MA-8	24200	10	0

*Assumed at programmed rate unless otherwise noted in mission analysis reports.

DATA REDUCTION

Raw thermocouple data in the form of commutated temperature histories were employed as the primary data source. The temperature histories were smoothed by plotting the raw digitized data and hand-fairing a smooth curve through the mean of the data. The resulting curves were numerically differentiated and the derivative was smoothed. To insure the absence of significant error in this process a new temperature curve was constructed from the smoothed derivative and compared with the original data. In all cases this constructed temperature history gave results which were everywhere within a few degrees of the original smoothed curve. This constructed temperature history was taken as the surface boundary condition on the data reduction program. For a discussion of the analysis leading to this choice of data smoothing procedure the reader is referred to Appendix A.

The data reduction program developed for this study employs the assumption that the thin afterbody skin can be treated as a spacewise isothermal volume convectively heated at its outer surface and thermally irradiated by the internal vehicle structure. Under this assumption the smoothed temperature data is employed as the bulk temperature of the wall and the outer surface is permitted to radiate to free space. The inner surface of the skin is radiatively coupled to the internal insulation and the temperature distribution history of the insulation is solved for by a standard finite difference routine. Output from this program is in the form of surface convective heating rate and insulation temperature distribution as functions of time. For a justification of the above assumptions and a description of the data reduction program, the reader is referred to Appendix A. The material properties employed are shown in tables 2a through 2c.

RESULTS

As noted above the fundamental results of this study are the measured afterbody heating rates obtained from the four flights considered. These measured heating rates are presented in tabular form together with the smoothed experimental skin temperature in tables 3a through 3d and in graphical form in figures 5 through 8. These results are presented as data with little or no interpretation or comparison with theory. It should be noted however that the results of the suborbital flight, MA-2, shown in figure 5 are somewhat inconsistent with the balance of the data presented since this vehicle flew with a large trim angle, $\alpha = 12.5^{\circ}$, over the major portion of the reentry trajectory. The data for the remaining three flights MA-5, MA-7, and MA-8, indicate a high degree of consistency which is even more apparent when the data are compared on a dimensionless basis.

The following section presents a comparison of the above mentioned data in dimensionless form with the prediction methods discussed in Appendix B.

Comparisons of Theoretical and Measured Afterbody Heating

In comparing the measured heat transfer rates obtained from flight test data with the heat transfer rates predicted from the theory of Denison, Baum, and King, it is convenient to present the results in dimensionless form. Since the Reynolds analogy was invoked during the course of the analysis (see Appendix B) the dimensionless form chosen was Stanton number as a function of length Reynolds number. For the present study these parameters are defined

$$St = \frac{q_{measured}}{\rho_e u_e (H_{rec} - h_w)}$$

$$Re_x = \rho_e u_e x / \mu_e$$

where "x" is measured along the vehicle surface from the stagnation point and the boundary layer edge properties and heating rates are obtained using the procedures described in Appendix B.

In the following subsections data from each of the four vehicles considered are presented. The results obtained from MA-5 are treated as typical and are discussed in detail. Results for the remaining three flights, MA-2, MA-7, and MA-8, are presented but detailed discussion is limited to those results which differ significantly from those obtained on MA-5.

The flight test data presented in this section are compared with the theory of Denison, Baum, and King, and with the theory of Chapman. In comparing the two theoretical predictions it should be kept in mind that the Chapman theory yields a true similarity solution which is the limiting case of the Denison, Baum, and King theory for very long separated regions. As noted in Appendix B the Denison, Baum, and King theory does not yield a unique relation between Stanton number and Reynolds number. This is due to the effects of initial conditions on the shear layer profiles which effects are relatively strong for short separated regions but tend to wash out at large values of "S". As a result of this the lines representing the Denison, Baum, and King theory on the Stanton number plots should be considered limit lines for the Mercury Spacecraft afterbody and should not be applied to significantly different configurations without consideration of the relative lengths of separated and forebody attached flows. The procedure outlined in Appendix B however is applicable to any axisymmetric configuration.

<u>MA-5</u>.-Figure 9a presents a comparison of predicted and experimental afterbody heating rates at the forward end of the conical section of the spacecraft of MA-5. These data indicate that for pure laminar separation in the range $2 \times 10^2 \leq Re_x \leq 2 \times 10^4$ the experimental heat transfer is

bracketed by the theories of Chapman, and of Denison, Baum, and King. At $Re_x \simeq 2 \times 10^4$ the dimensionless heating undergoes a severe change of behavior indicating transition or reattachment or perhaps both. The behavior of the data subsequent to $Re_x \simeq 5 \times 10^4$ is appropriate in level to attached laminar boundary layer heating although slope of the few data points appears to be closer to $-1/5$. In reference 1, Chapman points out a strong Mach number influence on separated turbulent heating which makes it impossible to assess the character of the flow from heating level alone. The behavior of the data at low Reynolds number, $Re_x < 10^2$, is rather more difficult to explain. This same data are presented in heating rate history form in figure 6a where the low Reynolds number data of figure 9a corresponds to times, $\theta - \theta_o$, less than 220 seconds. It is apparent from both of these figures that a sharp change in the character of the heating occurs abruptly at this time. The only event noted in the post launch report occurring at this time was the initiation of the Automatic Stabilization and Control System (ASCS) Roll Programming. The roll rate induced however is small, 10 deg/sec, and data previous to this time indicate no serious asymmetries in circumferential heating distribution, so that it is difficult to see how an effect of this magnitude could be associated with this event. A possible explanation for this behavior may be associated with the unaccounted for radiation heat transfer to the afterbody. The only remaining possibilities which might explain this behavior are either a sudden change in the character of the flow field, as from attached to separated flow, or a sudden zero shift in all the data. Since MA-5, MA-7, and MA-8 all exhibit this behavior the latter possibility appears unlikely.

Figure 9b displays the dimensionless heating at the midcone point and indicates essentially the same behavior as that shown on 9a. The low Reynolds number, early-time data indicate the same relatively high values of Stanton number. For Reynolds numbers in the range $5 \times 10^2 \leq Re_x \leq 2 \times 10^4$ the experimental results are bracketed by the theories of Denison, Baum, and King, and Chapman, and for $Re_x \simeq 2 \times 10^2$, the flow undergoes the previously noted change.

Figures 9c and 9d show the dimensionless heating at the aft end of the conical section and on the cylinder. The aft cone data, figure 9c, are consistent with the previously presented data except for a somewhat smaller value of "transitional" Reynolds number, $Re_x \simeq 8 \times 10^3$, which may well result from the large unfavorable pressure gradient in this region, see figure 10. The cylinder heat transfer data, figure 9d, is again bracketed by the two theories in the range $5 \times 10^2 \leq Re_x \leq 2 \times 10^4$, with apparently both transition, and reattachment occurring between $Re_x \simeq 2 \times 10^4$ and 2×10^5. The initial overshoot of the data beyond the attached turbulent prediction and subsequent convergence from above is characteristic of turbulent boundary layers preceeded by long "laminar runs", e.g., reference 5. These figures give a very strong indication of transition for $300 \leq \theta - \theta_o \leq 400$. This interpretation is reinforced by figure 11 where the streamwise variation of experimental heating is compared with attached and separated laminar and attached turbulent predictions. The data show that for late time $\theta - \theta_o \geq 400$ the flow over the aft portion of the afterbody is essentially transitional. For $\theta - \theta_o = 425$ the heating rate at $S/R = 1.45$ is nearly that for a fully developed attached turbulent boundary layer.

Another point which is of some interest is the apparent lag of experimental heating with respect to predicted heating. For example in figure 6a the experimental heating rates are positive near the end of the heating pulse even though the predicted driving potential (H_{rec} - h_W) is negative. Initially this was assumed to be associated with the very large possible error at late times, see Appendix A, but as more of the data were reduced it was noted that this lag was consistently present. An explanation of this behavior may well be associated with the step change in wall temperature as the boundary layer passes from the hot ablator material of the forebody to the relatively cool metal afterbody. Although there are no theoretical analyses of the non-isothermal wall effect for separated layers it is felt that consideration of the theory of Rubesin, reference 6, for attached laminar boundary layers may be informative. According to this theory the heat transfer downstream of a step discontinuity in surface temperature is given by the expression

$$q(x) = h(x)\left[T_{rec} - T_W^- - f\right]$$

where for a single discontinuity

$$f = \left[1 - \left(\frac{L}{x}\right)^{3/4}\right]^{-1/3} (T_W^+ - T_W^-)$$

and

L is the distance from the leading edge to the discontinuity

x is the distance from the leading edge to the point in question

T_W^- is the wall temperature just upstream of the discontinuity

T_W^+ is the wall temperature just downstream of the discontinuity

It can be seen from this expression that

$$\left[1 - \left(\frac{L}{x}\right)^{3/4}\right]^{-1/3} = A > 1$$

In the present case, the temperature downstream of the discontinuity approaches the recovery temperature and

$$\lim_{T_{rec} \to T_W} q(x) = h(x)\left[(T_W^+ - T_W^-) - A(T_W^+ - T_W^-)\right] = h(x)\left[(1 - A)(T_W^+ - T_W^-)\right]$$

As a consequence, for $T_W^- > T_W^+$ we have finite heat transfer even though the normally employed driving potential is zero. Physically this procedure accounts for the fact that it takes a significant run length to establish new similarity profiles in the thermal boundary layer. When the upstream temperature is higher than the recovery temperature, energy is transferred from the wall to the boundary layer. If the recovery temperature downstream of the discontinuity does not reflect this increase in energy, an erroneous specification of the driving potential will result. Although this analysis applies strictly only to an attached laminar boundary layer it is physically plausible to expect analogous behavior in a free shear layer. As a result of the restriction to attached laminar boundary layers in the above model direct application to the present separated transitional shear layer is not possible, however substitution of values appropriate to the MA-5 flight yield lag-times of the correct order of magnitude.

MA-2.-Figures 12a through 12d present a comparison of the experimental and predicted afterbody heating on the spacecraft of MA-2. As noted in table I the entry trajectory of this vehicle was characterized by a relatively high angle of attack.

Examination of figure 12a leads to the conclusion that the vehicle entered the atmosphere in a pitched up condition and retained this orientation during the major portion of the trajectory. From entry until boundary layer transition ($Re_x \simeq 2 \times 10^5$) the bottom centerline heating rates, segment 40, are nearly uniformly a factor of two larger than those on the top centerline. An apparent anomaly is evidenced by the fact that the two thermocouples in the yaw plane indicate heating rates of roughly a factor of two below those on the top centerline. Similar results however have been noted on the forebodies of slender cones at yaw in reference 7, where this phenomenon is attributed to separation and the establishment of trailing vortices in the cross flow plane. Figure 10 of reference 8 shows the circumferential distribution of heat transfer at the midcylinder point on the Mercury Spacecraft. These data indicate about a 20 percent increase in heating at a 10° angle of attack, in going from 90° to 180° from the windward meridian. The data are qualitatively consistent with previously obtained results. It should be noted that no effort has been made to account for angle of attack effects in the predicted heating results since the other three vehicles considered in this study were at essentially zero incidence over their entire trajectories.

Figure 12b presents essentially the same information for the midcone position. No thermocouples were located in the yaw plane for this body station, however the bottom centerline thermocouples again indicate somewhat higher heating rates than those on the top centerline lending credence to the assumption of a pitched up orientation. Again boundary layer transition appears to occur at a length Reynolds number of about 2×10^5.

The data of figure 12c are badly scattered and generally inconsistent with the preceding results. The bottom centerline thermocouple still indicates the highest local heating rate however.

Figure 12d presents the data for the single functioning instrument location on the cylinder. These results are in essential agreement with the cylinder data obtained in the other flights at zero angle of attack. The low Reynolds number data, $Re_x \leq 2 \times 10^4$, indicate separated laminar flow with a Reynolds number dependence somewhat greater than -1/2 followed by the beginning of transition at $Re_x \simeq 2 \times 10^4$, with what appears to be fully-developed attached turbulent flow for $Re_x > 2 \times 10^6$.

In general the quality of the data obtained from MA-2 is not as good as that obtained from the other three flights considered. The quality of data together with the angle of attack effects noted earlier render the comparisons of predicted and experimental heating more difficult than those for the other flights considered. As a result conclusions and recommendations offered in the final section of this report are based, for the most part, on flights MA-5, MA-7, and MA-8.

MA-7.-Figure 13a presents the dimensionless heating data for the forward portion of the conical section of the spacecraft of MA-7. With the exception of the data of segment 7, these data are consistent with the results obtained on MA-5. This leads to the conclusion that the segment 7 data shown here are in error. Comparison of the raw temperature data of segments 7, 8, 9, 10 indicate that while segments 8, 9, and 10 show peak temperatures of the order of 850° the peak temperature of segment 7 is nearly 1200°F. The results shown for segment 7 are then due to measurement error or some localized phenomenon and should not be considered in the comparison of predicted and experimental heating rates. The balance of the data shown in figures 13b and 13c show essentially the same behavior noted for the MA-5 data, i.e., relatively high heating rates at Reynolds numbers less than 500 followed by a gradual decay from values of Stanton number appropriate to Chapman's theory down to values appropriate to the Denison, Baum, and King theory. Transition for these data occurs in the range $2 \times 10^4 \leq Re_x \leq 5 \times 10^4$.

MA-8.-Figures 14a through 14d present the dimensionless heating data for the spacecraft of MA-8. These data are both qualitatively and quantitatively consistent with the results discussed earlier.

DISCUSSION

Probably the most interesting result of the present study is shown in figure 15, where representative results of this effort are compared with results obtained in reference 9. Despite the difference in level which is attributable to differences in the data reduction programs, both sets of data are extremely well correlated by a line with a -3/4 dependence on length Reynolds number. This form of correlation also appears to be applicable to the data of reference 10, although in this case the data presentation in the form of a continuous line makes comparison difficult. References 11 and 12 however present results obtained in wind tunnels for similar configurations which indicate good agreement with Chapman's theory. No explanation is apparent for this lack of agreement between wind tunnel and flight test data.

In comparison with the Reynolds number, the other influencing parameters appear to exert relatively little effect on Stanton number. The theory of Denison and Baum indicates a dependence on the upstream mass injection parameter, B'. This dependence is not observed in the experimental results, probably because it is masked by other effects and by data inaccuracies. Wall cooling ratio, (h_W/H_{tot}), does not generally exhibit any influence. However, at late times when this ratio becomes close to unity, there is some evidence that the surface temperature discontinuity between the forebody and afterbody causes an increase in afterbody heating.

The heat transfer correlations provide important information on the occurrence of transition. The lower limit of free shear layer transition, inferred from heat transfer, on the conical portion of the body is $Re_x = 2 \times 10^4$, see figure 16. These results indicate that transition in the free shear layer will be initiated in the range $2 \times 10^4 \leq Re_x \leq 5 \times 10^4$ and fully developed turbulence will occur in the range $2 \times 10^5 \leq Re_x \leq 10^6$ for the Mercury configuration.

CONCLUSIONS AND RECOMMENDATIONS

One of the principal conclusions to be drawn from the present study is that there are no completely satisfactory analytic techniques for the prediction of afterbody heating to manned reentry vehicles. While the level of heating is generally bounded by the alternative theories, the observed dependence on flow conditions is not well correlated. This discrepancy is attributed primarily to the fact that the influence of the recirculation flow characteristics is not accounted for in any of the theories. A second contributing factor is that the heat transfer predictions are based on a somewhat uncertain description of the inviscid flow field.

In order to obtain improved correlations of heat transfer data and to permit the accurate prediction of afterbody heating to future generation vehicles it is necessary to explain theoretically the behavior of the flight test data obtained in this study and in references 9 and 10. It is believed that the explanation for the consistent trends observed in these analyses lies in the detail of the recirculation region. It is therefore recommended that some effort be expended in developing a theory for the inner flow. Such a study should present no insurmountable difficulties since existing analyses should be adequate to define the outer boundary conditions on the low speed recirculating flow, which would permit the use of an iteration scheme to match inner and outer flow parameters.

APPENDIX A

THE INFERENCE OF EXPERIMENTAL SURFACE HEATING RATES ON THE PROJECT MERCURY CAPSULE AFTERBODY

INTRODUCTION

The inference of surface heating rates from thermocouple data is accomplished by taking an energy balance on an element of surface volume and solving the resulting equations for the heating rate required to support the observed temperature rise. Sketch A-1 schematically depicts the various components of energy to be accounted for in the energy balance.

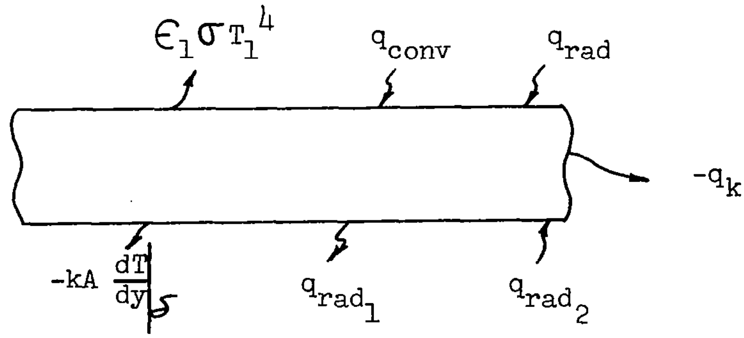

Sketch A-1.-Graphical presentation of energy flux.

In equation form the representation of figure A-1 can be written as:

$$q_{conv} = \epsilon_1 \sigma T_1^4 + q_{rad_1} + \rho c_p \frac{d}{d\theta} \int_0^{\delta} T dy - kA \left.\frac{dT}{dy}\right|_{\delta} - q_{rad} - q_{rad_2} - q_K$$

where

q_{conv}	is the convective heat flux to the outer surface
$\epsilon_1 \sigma T_1^4$	is the radiative loss from the outer surface

q_{rad_1} is the radiative loss from the inner surface

q_{rad} is the radiative heat flux to the outer surface resulting from earthshine, solar and/or shocklayer radiation

$\rho c_p \frac{d}{d\theta} \int_0^{\delta} T dy$ is the time rate of energy storage within the surface volume

$-k A \left. \frac{dT}{dy} \right|_{\delta}$ is the heat loss by conduction to the attached instrumentation and structure

q_k is the heat conducted away from the element due to temperature gradients along the skin

q_{rad_2} is the energy absorbed at the inner surface due to radiation from the internal structure

An exact accounting for all of the above mentioned terms is neither practical nor desirable since many of the parameters involved are highly uncertain and since many of the terms are small in comparison with others. A detailed accounting would result in an extremely cumbersome data reduction program with only small advantages in accuracy.

The sources of error to be considered can be grouped under two general categories; the first, truncation errors, evaluates the order of magnitude of the various components of energy flux to determine the error which would result from a failure to consider them, and the second, intrinsic errors, considers those sources of error which are associated with basic uncertainties in properties, configurations, and measurements.

TRUNCATION ERRORS

The truncation errors considered are those associated with failure to account for conduction losses to the instrumentation and vehicle internal structure, and those associated with failure to account for radiation losses to the internal structure and radiation received from external sources. In choosing an optimum data reduction program both the error magnitude associated with ignoring and the cost of including a specific term were considered.

Thermal Analyzer Study

In order to evaluate the effect of the thermocouple installation (see fig. 3) on the heat transfer inferred from measured skin temperature histories a Thermal Analyzer study was carried out. The Thermal Analyzer program is in effect simply a very general finite difference conduction program capable of treating virtually any geometrical configuration.

A nodal network of 143 nodes was constructed covering a surface area of 2.5 x 1.07 inches and assuming the temperature field to be symmetric about the thermocouple lead centerline. This assumed symmetry does not reflect the actual configuration; however, auxiliary hand calculations indicate the resulting error to be small. In addition, radiative coupling between the internal skin and insulation and the shielded thermocouple leads was not accounted for. The effective resistance to energy transfer from the insulation to the thermocouple wires was computed assuming the heat reflecting tape to have an emissivity of 0.1, the refrasil insulation on the thermocouple wire to be 0.075" thick, and the mean temperature to be 1000°F. Using these figures it was found that the effective resistance was of the same order of magnitude as the conduction resistance down the lead from the skin. At temperatures higher than 1000°R radiative transfer to the thermocouple leads will dominate the energy transfer and by increasing the internal temperature of the wire will further reduce conduction losses. Under these conditions the skin response will closely approach that of a thin skin with a heat capacity somewhat larger than that of the skin alone due to the presence of the retaining clip.

A representative convective heat rate history was imposed as a boundary condition in the Thermal Analyzer program, and the temperatures at different points on the plate determined. Figure 17 presents the temperature of the undisturbed wall and the temperature sensed by the thermocouple in close proximity to the retaining clip. The temperature of the thermocouple in the absence of the retaining clip is also presented for comparison. It is apparent from this figure that the presence of the retaining clip introduces a large perturbation on the temperature field. On the basis of this figure it is reasonable to assume that the presence of the clip will tend to make the wall behave more like a calorimeter than it would without the clip. Figure 18 compares the temperature sensed by the thermocouple with that of the clip close to the thermocouple. It is observed that the largest discrepancy between these temperatures is of the order of 15 degrees. It appears physically plausible then, that if the thermocouple temperature is employed together with a suitable average of the heat capacities of the skin and clip, and the skin and thermocouple, a reasonable approximation to the surface heating rate history could be obtained.

Figure 19 presents the results of this approximation. The solid line represents the convective heating rate originally imposed; the broken line represents the energy radiated away from the body by a surface at the thermocouple temperature, and the plotting symbols represent the convective heating to the body inferred from the thermocouple temperature under the assumption that the skin thickness, $\delta = 0.4(\delta_1 + \delta_2)$. The coefficient 0.4 was obtained by matching the heat rates at $\theta = 110$ seconds, and is physically reasonable since it results in nearly the arithmetic average of the thicknesses of the two nodes.

The relative error of this approximation is presented in figure 20 for thin skin data reduction both with and without internal radiation. An examination of these two figures together indicates that the initially large relative error, up to 15 percent, corresponds to an absolute error of less than 0.05 Btu/ft^2-sec, and the large oscillating error, of the order ±20 percent, late in the heating pulse corresponds to an absolute error of ±0.1 Btu/ft^2-sec. The heating rates over the balance of the heat pulse are determined by this procedure to within less than ±10 percent.

The relatively small error associated with the Thin Skin Data Reduction Program is even more attractive when the cost of obtaining the complete thermal analyzer solution is considered. The machine time required to compute the temperature histories from the specified heating rate was 34 minutes of IBM 7094 time.

The numerical errors associated with conduction losses through the structural elements and radiation losses to the metallic substructure have not been evaluated in detail. However, they are believed to be small since the location of the structural elements are thermally remote from the thermocouple junction, and the characteristic response time of the insulated joint is in excess of 700 times that of the skin. Insofar as radiation transfer to the structure is concerned the heat reflecting tape which covers all the exposed structural elements will tend to make the internal radiant transfer nearly one-dimensional. In brief, the design of the joints of skin to structure, see figure 21, is such as to provide good thermal isolation of the skin.

INTRINSIC ERRORS

The intrinsic errors noted must, for the most part, be treated in a more qualitative manner than the errors already considered. This is due to the fact that flight tests do not take place under controlled laboratory conditions and that dimensions and physical properties vary within certain limits due to manufacturing tolerances, included impurities, and environmental histories.

If it is assumed, for the moment, that temperatures can be measured with any desired accuracy the errors associated with the other parameters are limited to the following:

1. Density, thermal conductivity, and specific heat are sufficiently accurate to limit errors in inferred heating rates to a few percent. Due to preoxidation surface treatment the radiation properties would appear to be functions of temperature only so that the emissivity and absorptivity are probably accurate to within less than 5 percent unless the surface has been scratched or soiled in the immediate vicinity of the thermocouple.

2. Maximum error in surface heating rate due to uncertainties in skin thickness will be given by

$$\text{error} = \frac{0.016 \pm x}{0.016}$$

where x is the fabrication tolerance on the skin thickness. This tolerance is not called out on available drawings, however private communication with NASA/MSC indicates that the tolerance is of the order of $\pm$.003 in. resulting in a maximum error in measured heating rate of the order of 18 percent of the heat capacity-term. At high surface temperature the actual percent error in heating rate will be greatly reduced from this value since reradiation will dominate capacitive heat absorption.

The only remaining error source to be considered is that associated with the employment of thermocouple data as a boundary condition on the data reduction program.

DATA SMOOTHING

The principle difficulty in inferring heating rates from flight test data is that one must employ the inherently divergent process of differentiating experimental data. Figure 22 presents a plot of the "raw" thermocouple data obtained from segment 33 of flight MA-5. It should be pointed out that in terms of data scatter this represents the worst of the data obtained on flight MA-5. Since an upper bound of error is sought, it is judged that this data should be considered in the data smoothing and error analysis. An examination of this data indicates graphically the divergence noted above. At almost any value of the abscissa the consideration of two consecutive data points will lead to the evaluation of a derivative which is substantially different from that evidenced by the local bulk of the data. For this reason techniques must be employed which permit the averaging of the data points locally, together with the physical constraints that the temperature and its derivative be, at least piecewise, smooth and continuous.

Since the actual temperature history represented by the data of figure 22 is unknown it becomes necessary to define an error associated with a given data smoothing procedure somewhat arbitrarily. For the present application it was decided that a rational error could be defined in terms of the band of temperature derivative obtained using two or more data smoothing procedures. That is to say if several different techniques of data smoothing yield the same value of $dT/d\theta$, then the error is considered to be zero, whereas if they yield differing values the error is considered to be proportional to the difference.

Three different techniques for data smoothing were employed here. The first was a simple hand faired curve through the mean of the data, with hand smoothing of the subsequently computed derivatives, the second method employed is described in reference 13 and is similar to that mentioned above except that prior to hand fairing the temperature curves the data is averaged in scatter bands and the curve is hand faired through the resulting averaged points. The third method employed considered the data to be divided into five overlapping regions for $80 \leq \theta \leq 260$ sec., $200 \leq \theta \leq 380$ sec., $260 \leq \theta \leq 430$ sec., $360 \leq \theta \leq 470$ sec., and $430 \leq \theta \leq 580$ sec. The data was then fit in each of these regions with a least squares polynomial of the form

$$T = \sum_{i=0}^{n} a_i \theta^i$$

where n was varied from 2 to 5. The polynomial giving the best fit in each region was chosen and a composite temperature and temperature derivative was constructed by patching the polynomials together at points where they were in essential agreement in magnitude and slope.

Temperature derivatives were constructed using the results of all three data smoothing procedures. The envelope defined by the extreme values of the several methods is shown in figure 23. It can be seen that the temperature derivative is fairly well defined for the period from 140 to 420 seconds. From 420 to 460 seconds the derivative is seen to change very rapidly from large positive to large negative values and in this region the data is not sufficiently precise to permit specification of $dT/d\theta$ within a factor of two.

Figure 24 presents the error, or uncertainty, in observed heating rates obtained by employing the upper and lower bounds of $dT/d\theta$ obtained from figure 23. It can be seen that the absolute error is of the order of ± 0.05 Btu/ft^2 for $130 \leq \theta \leq 420$ seconds while subsequent to $\theta = 420$ seconds, the error is of the same order of magnitude as the heat rate.

The maximum error associated with errors in temperature level occurs near $\theta = 430$ where radiation transfer is the dominant mechanism. For this time the worst data gives $T_W = 930 \pm 25°F$ which would yield, at worst, errors in heating rate of the order of ± 10 percent.

SUMMARY OF ERROR ANALYSIS

The errors in inferred heating rates resulting from the various sources listed have been evaluated. While that list of possible sources is not exhaustive, it is believed to contain the primary sources. The results indicate that if all errors were to act in the same direction, the maximum error during the period of reliable data reduction (150 to 420 seconds for flight MA-5) would not exceed about 50 percent. The major contributors and the approximate magnitudes are:

Intrinsic Errors

Capacitive term		% Error (Maximum)
properties	<	3
thickness tolerance	<	18
temperature slope	<	15
Radiative term		
radiative properties	<	5
temperature level	<	15
Truncation Errors	<	10

The actual error resulting from the simultaneous action of all the error sources should be significantly less since some compensation should occur. Because the intrinsic errors are relatively large, appreciable truncation error may be accepted without undue increase in uncertainty of the results. For this reason, a relatively simple procedure has been adopted for computation of heat rates from the temperature data.

It should be noted that the foregoing analysis applies only to Rene 41 skin. The relatively thick (0.25") beryllium cylindrical section should not be effected to any great degree by the thermocouple installation. The primary error in this area will arise from temperature gradients through the skin. Even this error is small however, due to the high thermal conductivity of the beryllium.

DATA REDUCTION

It was determined above that the data reduction could be accomplished with an accuracy consistent with the accuracy of the measured temperatures by making an equivalent thickness assumption. As a consequence the data reduction procedure employs the thin skin assumption and solves an energy balance for the configuration shown in figure 25.

The equations employed in the data reduction program are:

for the thin skin

$$T_1 = T_1(\theta)$$

and

$$\rho_W \, c_{p_W} \, \delta_W \frac{dT_1}{d\theta} = q_{conv} - \epsilon_1 \sigma T_1^{\,4} - (q_{rad_1} - q_{rad_2})$$

where

$$q_{rad_1} - q_{rad_2} = \frac{1}{\frac{1}{\epsilon_1} + \frac{1}{\epsilon_2} - 1} \sigma (T_1^{\,4} - T_2^{\,4})$$

For the surface of the insulation

$$q_{rad_1} - q_{rad_2} = \rho_2 \, c_{p_2} \, \delta_2 \frac{dT_1}{d\theta} + K_2 \frac{T_2 - T_3}{x_3 - x_2}$$

For the interior of the insulation

$$\rho_i \, c_{p_i} \, \delta_i \frac{dT_i}{d\theta} = k_{i-1} \frac{T_{i-1} - T_i}{x_i - x_{i-1}} - k_i \frac{T_i - T_{i+1}}{x_{i+1} - x_i}$$

and for the inside surface of the insulation

$$k_n \frac{\partial T_n}{\partial x} = \rho_n \, c_{p_n} \, \delta_n \frac{T_n}{\theta}$$

where

$$c_{p_W} = c_{p_W}(T_W)$$

and

$$c_{p_{ins}} = c_{p_{ins}}(T)$$

$$k_{ins} = k_{ins}(T, \text{altitude})$$

These equations are solved by standard finite difference techniques yielding $q_{conv}(\theta)$, the surface convection heating rate, and the temperature distribution through the insulation.

HEATING RATE HISTORIES

The procedures described above have been used to convert the flight test temperature data, obtained from the spacecraft of Mercury Atlas Mission Nos. 2, 5, 7, and 8, to convection heating rates as functions of time.

The spacecraft carried several chromel-alumel thermocouples affixed to the inside surface of the afterbody. The locations of these instruments are shown in figures 2a - 2d. As can be noted from these figures, the majority of the thermocouples are located on the inner surface of the 0.016" Rene 41 shingles, the remaining thermocouples on the inner surface of the 0.22" beryllium shingles. The equivalent thickness assumption was not employed in the data reduction of this latter location. Instead, the net heat transfer (convection less reradiation) was simply equated to the rate of capacitive heat gain for the 0.22" beryllium slab.

Discussions of the results are presented in the main body of this report.

APPENDIX B

PREDICTION TECHNIQUES

This appendix describes the techniques employed in predicting the flow parameters, heat transfer, and heat shield response for both the forebody and afterbody of the Project Mercury Capsule. The forebody is considered in order to define initial conditions for the separated afterbody flow. Since the forebody analyses are of secondary importance, detailed results for heat transfer and shield response are presented only for one flight, the MA-5.

FLOW FIELDS

In consideration of the flow field, attention was directed to definition of the surface pressure distribution. Knowledge of this distribution enables computation of the desired convective heating parameters.

Forebody.-The configuration of the Project Mercury Capsule forebody can be described as a spherical segment having a 74.5 inch diameter and an 80 inch radius of curvature. The half angle subtended by the forebody at the center of curvature is 28°. Since, for this configuration, the body sonic point is located at the discontinuity in body curvature the subsonic portion of the flow field cannot be easily described by available analytic techniques.

Fortunately this and similar configurations have been the subject of extensive wind tunnel test programs so that the flow field can be described to a reasonable accuracy on the basis of empirical information. Figure 26 indicates that while the density, temperature, and velocity distributions may be strong functions of energy level the pressure distribution over blunt bodies exhibits the well known hypersonic freeze. The results for a hemispherical configuration in figure 26 compare the real gas numerical solutions of Lomax and Inouye, reference 14, with the modified Newtonian approximation. The shock density ratio varies over a more than two-fold range with only small effects on pressure distribution.

Figure 27 compares the modified Newtonian approximation with the measured pressure distribution of Boison and Curtiss, reference 15, over a 30° half-angle spherical segment. It can be seen that the surface pressure is closely represented by the Newtonian prediction to roughly half the distance from the stagnation point to the shoulder. At $S/R_N = 0.3$ the surface pressure begins to fall more rapidly than the Newtonian prediction reflecting the effect of the sonic corner at $S/R_N = 0.525$.

Figure 28 compares wind tunnel data compiled from references 16 through 20 with the modified Newtonian approximation. The broken line shown in this figure is the pressure distribution inferred from the data. This pressure distribution was employed in all subsequent calculations of forebody convective heating. The data accuracy is not sufficient to deduce stagnation point velocity gradient and other sources must be consulted.

Figure 29 shows a comparison of the stagnation point velocity gradient as inferred from the numerical results of Lomax and Inouye, and the theory of Li and Geiger, reference 21, with the measured stagnation point velocity gradients on spherical segments as obtained by Boison and Curtiss, reference 15. The broken line on this figure was constructed to pass through the $\beta^* = 28^o$ point and to retain the variation with shock density ratio shown by the Li and Geiger theory and the numerical results of Lomax and Inouye. This matching procedure yields, for the Mercury Capsule configuration

$$\frac{R_N}{u_\infty} \left. \frac{du}{ds} \right|_{ST} = 1.08\sqrt{k(2-k)}$$

where

$$k = \rho_\infty / \rho_{ST}$$

Afterbody.-Since no analytic solutions are available to obtain the detailed flow field over the Mercury spacecraft forebody it was not possible to employ analytic techniques in determining the afterbody flow field parameters. Again, a substantial body of wind tunnel data was fortunately available for empirical description of the afterbody pressure distribution. In reference 8, Weston and Swanson have collected and correlated the major portion of the available ground-test pressure data on the Mercury spacecraft afterbody. These correlations are presented in figure 10. The ordinate of this figure is the local pressure normalized with respect to the stagnation point pressure. The abscissa is the distance from the sphere cone junction normalized with respect to the maximum body diameter. It is interesting to note that while the pressure on the conical portion of the vehicle can be correlated by a single curve the pressure on the cylindrical portion of the vehicle shows a strong Reynolds number dependence. This increase in cylinder pressure with increasing free stream Reynolds number is consistent with a tendency of the boundary layer to reattach on the cylinder at high Reynolds number.

In brief the technique employed to determine the boundary layer edge properties was to evaluate the free stream Reynolds number variation with time for each of the four trajectories considered, and at each of the Reynolds numbers noted on figure 10, to assign the appropriate pressure distribution. These pressure distributions together with the assumption of an isentropic expansion from the stagnation point were employed to obtain the boundary layer conditions using real gas properties of air as presented in reference 22. Edge properties for each of the instrumented locations and each of the five Reynolds numbers were then cross plotted as functionsof time for each of the four trajectories. This procedure then yields the variation of boundary layer edge properties with time at each location of interest for each of the four trajectories. For times prior to those associated with $Re_{\infty_D} = 2 \times 10^5$ the pressure distribution for $Re_{\infty_D} = 2 \times 10^5$ was assumed to apply.

Heat Transfer and Shield Response

Forebody.-Stagnation point heat transfer to the Mercury spacecraft was predicted from the flow field parameters of the previous section using the theory of Fay and Riddell, reference 23, and the viscosity of Peng and Pindroh, reference 24. Figure 30 presents the cold wall, non-blowing stagnation point heat rate history computed for MA-5. Also shown in this figure is the net heat transfer to the wall accounting for the effects of the time dependent wall temperature and pyrolysis gas injection. These results, while not specifically applicable to the present study goals, are required to define the initial conditions on the afterbody boundary layer.

The distribution of laminar boundary layer heating, which is shown in figure 31, was predicted from the theory of Lees, reference 25. Forebody laminar boundary layer heating distributions were computed for two trajectory points. The first, for conditions near peak laminar boundary layer heating, and the second, for conditions near the end of the heating pulse. It can be seen from figure 31 that the distribution of laminar boundary layer heating is essentially independent of time and varies by only 15 percent over the entire front face of the vehicle.

The predicted convective heat transfer described above specified the boundary condition necessary for prediction of heat shield material response. In this latter prediction the LMSC computer program "Charring in Reinforced Plastics" (CHIRP III) was employed. The basic relations used in this program are described in reference 26. Figure 32 presents the surface temperature history and the temperature history at a nominal 1 inch depth for the forebody heat shield obtained from the prediction. The history of the blowing parameter, $B' = \rho_W v_W / C_H$ is presented in figure 33, for the stagnation point and a point on the periphery of the spherical segment. This parameter is of particular importance for the prediction of afterbody heating since, according to reference 2, for the range of B' over the forebody $0 \leq B' \leq 1.5$, a difference in afterbody heating level of more than 40 percent can result.

As an experimental verification of these results, figure 34 presents the predicted final density profile in the forebody heat shield. Visual observations of post flight core samples of the heat shield, as reported in Post Launch Reports, indicate a char thickness of 0.3 to 0.35 inches. The predicted curve of figure 34 indicates the material is essentially unchanged at depths greater than 0.39 inches and that the experimentally observed char depths correspond to a 10 to 30 percent degradation of the resin binder. The predicted mass loss for the forebody was 11.5 lbs. which compares favorably with the average of measured mass losses of 6.7 lbs. for mission MA-5 and 17.43 lbs. for mission MA-8. The large discrepancy between the two measured weights is attributable to different drying procedures employed on the two spacecraft after recovery from the ocean.

Afterbody.-Flow over the afterbody of the Mercury spacecraft will be separated for at least a portion of the entry trajectory. As a result the attached boundary layer theories discussed for the forebody must be supplemented. In reference 27, Chapman, et. al., have divided separated flows into three categories depending on the transition point location. The first category is pure laminar separation for which boundary layer transition occurs, if at all, downstream of the reattachment point, the second category is transitional separation for which transition occurs between the separation and reattachment points, and the third category is turbulent separation for which transition occurs at or upstream of the separation point. Of these three categories, only the first has received extensive analytic attention, e.g., reference 1 through 4 and 27 through 32. Although a large number of experimental studies on separation have been carried out for transitional and turbulent boundary layers, e.g., references 33 through 35, only Korst, et. al., reference 36, have had analytic success with turbulent separation and then only for fully developed mixing profiles. The Crocco-Lees theory, reference 37, while applicable to all of the above types of separation requires the empirical evaluation of certain governing parameters and is not readily applied in engineering calculations.

Consideration of the pressure distributions of figure 10 and the magnitude of the heating rates obtained from the data reduction program indicates that the separated flow over the afterbody of the Mercury spacecraft can be considered to be of the pure laminar type over a major portion of the trajectory. Consequently attention has been restricted to the laminar shear flow problem.

In choosing among the several theoretical treatments available for the prediction of heating to the Mercury spacecraft afterbody the following criteria were employed:

1. The method used should require a minimum of empirical information in predicting base heating.

2. It should be sufficiently general to apply to configurations ranging from that of Project Mercury to that of Project Apollo and to apply to the entire trajectories.

3. It should be applicable to engineering calculations without resorting to a large computer effort.

For pure laminar separation Chapman's model, references 1, 27, and 29, has had extensive empirical verification. The principle limitation of Chapman's theory based on this model is the failure to account for the effects of initial boundary layer thickness. Due to this fact he was able to obtain similarity solutions which are strictly applicable only for leading edge separation, where the initial boundary layer thickness is small, or to the free shear layer far downstream of the separation point, where the effects of initial conditions have washed out.

More recently Denison, Baum, and King, references 2, 3, and 4, have extended Chapman's model to the case of finite boundary layer thickness at the separation point, assuming an initial Blasius velocity profile, and have accounted for the effects of upstream transpiration assuming the initial velocity profiles of Emmons and Leigh, reference 38. Since the theory of Denison, Baum, and King comes closest to fitting the previously established criteria this method was chosen for comparison with flight test data.

Figure 35 presents a comparison of the several heating theories which are potentially applicable to the Mercury spacecraft afterbody. The predicted distributions of heat transfer shown on this figure are; the attached turbulent boundary layer heating prediction of Bromberg, Fox, and Ackermann, reference 39, the attached laminar boundary layer theory of Lees, reference 25, and the separated laminar shear layer theories of Chapman and of Denison, Baum, and King. It should be noted that the predicted heating rates are for a specific vehicle and trajectory time and are normalized with respect to the predicted stagnation point heat transfer. The low prediction of the Denison, Baum, and King theory relative to the Chapman theory is indicative of the relatively short length of the Mercury afterbody compared with the distance required to approach similarity profiles in the free shear.

It should be noted that none of the available theories for separated flow which comply with the aforementioned criteria consider the recirculation region in detail. Since this is the case certain additional assumptions and relations must be established in order to extend the theory to the prediction of base heating. These assumptions and the development of the necessary relations are now presented.

The theory of Denison, Baum, and King presents an extension of Chapman's free shear layer analysis to the case of finite boundary layer thickness at separation and includes the effect of transpiration upstream of separation. As with Chapman's analysis the details of the recirculation region are ignored. As a result of this lack of consideration of the recirculation region the flow parameters in the vicinity of the wall are not obtained and, in fact, only the transformed momentum equation is solved. Despite these severe limitations, this theory presents the most complete and rigorous results which can be generalized and employed in engineering calculations.

In applying this analysis to the Mercury spacecraft, three assumptions in addition to those employed in the basic analysis are required. These assumptions are:

1. Reynolds analogy applies on the dividing streamline.

2. The recirculation region is thin and isoenergetic, i.e., it neither contributes to, nor retards heat transfer from the free shear layer to the wall.

3. The enthalpy on the dividing streamline is linearly related to the velocity.

The first of these assumptions is supported analytically by Chapman, reference 1, where he shows that although there is no reason to assume the validity of Reynolds analogy for this case the heat transfer and shear parameters are numerically equal for $Pr = 1$ and $(dP/dx) = 0$. The latter two assumptions are less easily justified. Schlieren and oil flow studies of reference 19 indicate that the recirculation region is in fact thin but no conclusions can be drawn with regard to the variation of energy content. The final assumption, that the enthalpy on the dividing streamline is given by the Crocco integral is valid in the limit as Chapman's distribution is approached but is applied here over the entire separated region.

In reference 2, Baum presents the generalized shear and velocity on the dividing streamline as a function of distance downstream of separation with forebody blowing rate as parameter. These results are reproduced here as figures 36 and 37. Employing assumptions 1 and 2 above, we have

$$St_W = St_D = \frac{1}{Pr^{2/3}} \left. \frac{C_f}{2} \right|_D \tag{B-1}$$

where the subscript W indicates wall conditions and subscript D indicates dividing streamline conditions and

$$\left. \frac{C_f}{2} \right|_D = \frac{\mu_D \left. \frac{\partial u}{\partial y} \right|_D}{\rho_e u_e (u_e - u_D)} = \frac{\mu_D \left. \frac{\partial u}{\partial y} \right|_D}{\rho_e u_e^2 \left(1 - \frac{u_D}{u_e}\right)} \tag{B-2}$$

From the definitions of references 2, 3, and 4

$$F_D \sqrt{2\ S_b} = \left. \frac{\partial u/u_e}{\partial Y} \right|_D \sqrt{2\ S_b}$$

where

$$Y = \int \rho_e u_e\, r \frac{\rho}{\rho_e}\, dy$$

then

$$\mu_D \frac{\partial u}{\partial y}\bigg|_D = \frac{\mu_D u_e}{\sqrt{2 S_b}} F_D \sqrt{2 S_b} \frac{\partial \chi}{\partial y}$$

or

$$\mu_D \frac{\partial u}{\partial y}\bigg|_D = \frac{\rho_e u_e^2 r}{\sqrt{2 S_b}} \frac{\rho_D \mu_D}{\rho_e \mu_e} \mu_e F_D \sqrt{2 S_b} \qquad \text{(B-3)}$$

Combining equations (B-1), (B-2), and (B-3) we obtain

$$St_D = \frac{r}{Pr^{2/3}} \left(\frac{\rho_D \mu_D}{\rho_e \mu_e}\right) \frac{\mu_e F_D \sqrt{2 S_b}}{\sqrt{2 S_b}\left(1 - \frac{u_D}{u_e}\right)}$$

or finally letting

$$\frac{\rho_D \mu_D}{\rho_e \mu_e} = \ell$$

$$\frac{St}{\ell} = \frac{r}{Pr^{2/3}} \frac{\mu_e F_D \sqrt{2 S_b}}{\sqrt{2 S_b}\left(1 - \frac{u_D}{u_e}\right)}$$

Since this expression does not yield an explicit relation for Stanton number as a function of Reynolds number both of these parameters were evaluated for the foremost and aftermost thermocouple stations of the MA-5 trajectory. These parameters were evaluated from figures 36 and 37 using the boundary layer edge conditions previously described and assuming

$$1 - \frac{h_D}{H_{ST}} = 1 - \frac{u_D}{u_e}$$

This latter assumption is not critical since it is used only in evaluation of the ratio $(\rho_D \mu_D)/(\rho_e \mu_e)$ which parameter is a weak function of enthalpy ratio.

The results of these numerical computations are presented in figure 38. The lines on this figure represent the variation of upper and lower bound, with Reynolds number for $0 \leq B' \leq 1.5$. It can be seen from this figure that even for constant B' the computations do not collapse onto a single line. That is to say there is a weak dependence on S^* in addition to that accounted for by Re_x. This dependence, however, has not been considered in the data correlation. The variation of S^* with S/R for the Mercury configuration with $\theta - \theta_o$ as parameter is shown in figure 39.

REFERENCES

1. Chapman, D. R.: A Theoretical Analysis of Heat Transfer in Regions of Separated Flow. NACA TN 3792, 1956.

2. Baum, E.: Effect of Boundary Layer Blowing on the Laminar Separated Shear Layer. Electro Optical Systems, Res. Note RN 9, Apr. 1963.

3. Denison, M. R.; and Baum, E.: Compressible Free Shear Layer with Finite Initial Thickness. AIAA Journ., Feb. 1963.

4. Baum, E.; King, H. H.; and Denison, M. R.: Recent Studies of the Laminar Base Flow Region. AIAA Preprint 64-5.

5. Reynolds, W. C.; Kays, W. M.; and Kline, S. J.: Heat Transfer in the Turbulent Incompressible Boundary Layer - Part IV, Effect of Location of Transition and Prediction of Heat Transfer in a Known Transition Region. NASA MEMO 12-4-58W, Dec. 1958.

6. Rubesin, M. W.: An Analytic Investigation of the Heat Transfer Between a Fluid and a Flat Plate Parallel to the Direction of Flow Having a Stepwise Discontinuous Surface Temperature. M.S. Thesis, Univ. of California, Berkeley, 1945.

7. Wittliff, C. E.; and Wilson, M. R.: Heat Transfer to Slender Cones in Hypersonic Air Flow Including the Effects of Yaw and Nose Bluntness. Journ. Aero/Space Sci., Jul. 1962.

8. Weston, K. C.; and Swanson, J. E.: A Compilation of Wind Tunnel Heat Transfer Measurements on the Afterbody of the Project Mercury Capsule Reentry Configuration. (U). NASA TMX-495, Aug. 1961 (REPORT CONFIDENTIAL)

9. Weston, K. C.; and Fitzkee, A. L.: Afterbody Heat Transfer Measurements Obtained During Reentry of the Spacecraft of the Mercury-Atlas 5 Mission. (U). NASA TMX 564, Dec. 1963 (REPORT CONFIDENTIAL).

10. Stephens, Emily W.: Afterbody Heating Data Obtained from an Atlas Boosted Mercury Configuration in a Free Body Reentry. NASA TMX 493, Aug. 1961.

11. Lee, George: Correlation of Heat Transfer Data for the Apollo Afterbody at Mach Numbers 8 to 20. NASA TMX 855, Feb. 1964.

12. Reller, J. O., Jr.; and Seegmiller, H. L.: Pressure and Heat Transfer Measurements on a Mercury Capsule Model. NASA TMX 647, May 1962.

13. Murphy, J. D.; and Rubesin, M. W.: An Evaluation of Free Flight Test Data for Aerodynamic Heating from Laminar, Turbulent, and Transitional Boundary Layers. Part I The Air Force Mark 2 Reentry Body. (U). Vidya Rpt. 135, Sep. 1964 (REPORT CONFIDENTIAL).

14. Lomax, M.; and Inouye, M.: Numerical Analysis of Flow Properties About Blunt Bodies Moving at Supersonic Speeds in an Equilibrium Gas. NASA TR R-204, July 1964.

15. Boison, J. C.; and Curtiss, H. A.: An Experimental Investigation of Blunt Body Stagnation Point Velocity Gradient. ARS Journ., Feb. 1959.

16. Newlander, R. A.; Taylor, N. L.; and Pritchard, E. B.: Pressure Distribution on Two Models of a Project Mercury Capsule for a Mach Number Range of 1.60 to 6.01 and Angle of Attack 0° to 180°. NASA TMX-336, Nov. 1960.

17. Wallace, A. R.; and Swain, W. N.: Static Stability, Heat Transfer, and Pressure Distribution Tests of NASA-McDonnel Mercury Models at Mach Numbers 17 to 21. (U). AEDC TN 59-157, Jan. 1960 (REPORT CONFIDENTIAL).

18. Pritts, O. R.; and Mallard, S. R.: Pressure and Heat Transfer Distribution on a One Tenth Scale Mercury Capsule at Mach Number 8. (U). AEDC TN 59-164, Jan. 1960 (REPORT CONFIDENTIAL).

19. Everhart, P. E.; and Bernot, P. T.: Measurements of the Surface Flows, Heat Transfer, Pressure Distribution, and Longitudinal Stability of a Mercury Capsule Model at Mach Numbers 6.9 and 9.6. (U). NASA TMX-458, Apr. 1961 (REPORT CONFIDENTIAL).

20. Taylor, N. L.; Hodge, W. F.; and Burbank, P. B.: Heat Transfer and Pressure Measurements of a 1/7 Scale Model of a Mercury Capsule at Angles of Attack from 0° to $\pm 20^{\circ}$ at Mach Numbers of 3.50 and 4.44. (U). NASA TMX-522, June 1961 (REPORT CONFIDENTIAL).

21. Li, T. Y.; and Geiger, R. E.: Stagnation Point of a Blunt Body in Hypersonic Flow. Journ. of Aero. Sci., Jan. 1957.

22. Moeckel, W. E.; and Weston, K. C.: Composition and Thermodynamic Properties of Air in Chemical Equilibrium. NACA TN 4265, Apr. 1958.

23. Fay, J. A.; and Riddell, F. R.: Theory of Stagnation Point Heat Transfer in Dissociated Air. Journ. of Aero. Sci., Feb. 1958.

24. Peng, T. C.; and Pindroh, A. L.: An Improved Calculation of Gas Properties at High Temperature Air. Boeing Doc. no. D-2-11722, Feb. 1962.

25. Lees, L.: Laminar Heat Transfer Over Blunt Nosed Bodies at Hypersonic Flight Speeds. Jet Propulsion, Apr. 1956.

26. Kratsch, K. M.; Hearne, L. F.; and McChesney, H. R.: Theory for the Thermophysical Performance of Charring Organic Heat Shield Composites. Lockheed Missiles & Space Co., LMSC/803099 2-60-63-7, Oct. 1963.

27. Chapman, D. R.; Kuehn, D. M.; and Larson, H. K.: Investigation of Separated Flows in Supersonic and Subsonic Streams with Emphasis on the Effect of Transition. NACA TR 1356, 1958.

28. Pallone, A.; Erdos, J.; and Eckerman, J.: Hypersonic Laminar Wakes and Transition Studies. AIAA Journ., May 1964.

29. Chapman, D. R.: An Analysis of Base Pressure at Supersonic Velocities and Comparison with Experiment. NACA Rpt. 1051, 1951.

30. Kubota, T.; and Dewey, C. F.: Momentum Integral Methods for the Laminar Free Shear Layer. AIAA Journ., vol. 2, no. 4, Apr. 1964.

31. Nielsen, J. N.; Lynes, L. L.; Goodwin, F. K.; and Holt, M: Calculation of Laminar Separation with Free Interaction by the Method of Integral Relations. AIAA 2nd Aero. Sci. Meeting, Jan. 25-27, 1964.

32. Lees, L.; and Reeves, B. L.: Supersonic Separated and Reattaching Laminar Flows: I. General Theory and Application to Adiabatic Boundary Layer Shock Wave Interaction. AIAA Journ., vol. II, no. ii, Nov. 1964.

33. McCarthy, J. F.; and Kubota, T.: A Study of Wakes Behind a Circular Cylinder at M = 5.7. AIAA Journ. vol. 2, no. 4, Apr. 1964.

34. Bogdonoff, S. M.; and Kepler, C. E.: Separation of a Supersonic Turbulent Boundary Layer. Princeton Univ., Dept. of Aero. Eng., Rpt. 249, Jan. 1954.

35. Tomke, G. J.: Separation and Reattachment of Supersonic Turbulent Boundary Layers Behind Downstream Facing Steps and Over Cavities. Douglas Rpt. SM-43062, Mar. 1964.

36. Korst, H.; Page, R.; and Childs, M: A Theory for Base Pressue in Transonic and Supersonic Flow. Univ. of Illinois, Eng. Exp. Sta., Eng. Tech. Note 392-2, Mar. 1955, or AFOSR TN-55-89.

37. Crocco, L.; and Lees, L.: A Mixing Theory for the Interaction Between Dissipative Flows and Nearly Isentropic Streams. J. Aeron. Sci., vol. 19, no. 10, Oct. 1952.

38. Emmons, E. W.; and Leigh, D.: Tabulation of the Blasius Function with Blowing and Suction. Harvard Univ., Div. of Appl. Sci., Combustion Aero Lab., Interim Rpt. no. 9, Nov. 1953.

39. Bromberg, R.; Fox, J. L.; and Ackermann, W. O.: A Method of Predicting Convective Heat Input to the Entry Body of Ballistic Missile. (U). Transactions of 1st Tech. Symposium on Ballistic Missiles, WDC, ARDC, and R-W Corp., June 1956 (REPORT CONFIDENTIAL).

TABLE IIa

THERMOPHYSICAL PROPERTIES OF RENE 41

$T \sim {}^{o}R$	$C_p \sim \frac{Btu}{lb^{o}R}$	$k \frac{Btu}{ft^2 sec {}^{o}R/ft}$	$\rho \sim \frac{lb}{ft^2}$	ϵ
400	0.1	0.00110	514.8	0.9
500	0.1	0.00124		
600	0.1067	0.00136		
700	0.1122	0.00149		
800	0.1164	0.00162		
1000	0.1236	0.00186		
1300	0.1315	0.00225		
1600	0.1359	0.00264		
1660	0.1366	0.00269		
2000	0.1406	0.00315		
2400	0.1481	0.00366	514.9	0.9

TABLE IIb

THERMOPHYSICAL PROPERTIES OF THERMOFLEX RF 300

$T \sim {}^{o}R$	$c_p \sim \frac{Btu}{lb^{o}R}$	$k \frac{Btu}{ft^2 sec^{o}R/ft}$			
		200 K-ft	150 K-ft	100 K-ft	Sealevel
400	0.2135	0.1×10^{-5}	0.13×10^{-5}	0.17×10^{-5}	0.2×10^{-5}
500	0.217	0.10	0.15	0.21	0.25
600	0.22	0.10	0.17	0.26	0.3
700	0.22	0.20	0.24	0.35	0.4
800	0.22	0.25	0.40	0.51	0.63
1000	0.2241	0.91	0.97	1.2	1.36
1300	0.2461	1.53	1.76	1.96	2.18
1600	0.258	2.18	2.43	2.76	3.05
1660	0.26	2.30	2.56	2.91	3.23
2000	0.268	2.98	3.30	3.70	4.20
2400	0.275	3.7	4.07	4.54	5.24

$\rho = 3 \ lb/ft^3$
$\epsilon = 0.9$

TABLE IIc

THERMOPHYSICAL PROPERTIES OF BERYLLIUM

$T \sim {}^{o}R$	$c_p \sim \frac{Btu}{lb^{o}R}$	$k \frac{Btu}{ft^2 sec^{o}R/ft}$	$\rho \cdot \frac{lb}{ft^3}$	ϵ
560	0.463	0.0236	115.5	0.9
960	0.590	0.0206	↕	↕
1460	0.680	0.0169	↕	↕
2460	0.750	0.0156	115.5	0.9

TABLE IIIa

EXPERIMENTAL TEMPERATURE AND CONVECTIVE HEATING RATE HISTORIES, MA-2

Segment 28-29[(a)]

$\theta-\theta_o$, sec	T_w, °F (b)	q, $\frac{Btu}{ft^2\text{-}sec}$
0	80	0.413
10	84	0.227
20	86	0.416
30	90	0.464
40	94	0.395
44	96	2.162
48	105	7.110
52	135	12.19
60	238	16.62
66	343	12.03
70	393	3.846
74	408	2.200
78	416	1.377
82	420	0.261
90	420	0.079
100	417	-0.165
110	412	-0.365
120	405	-0.332
130	399	-0.626
140	390	-1.160
150	374	-2.402
160	369	-0.764
170	359	-1.101
180	346	-0.841
190	335	-1.230

Segment 32

$\theta-\theta_o$, sec	T_w, °F (b)	q, $\frac{Btu}{ft^2\text{-}sec}$
0	101	0.127
10	110	0.188
20	125	0.289
30	150	0.443
40	190	1.264
50	315	3.258
60	640	4.717
66	885	2.706
70	917	0.783
80	785	-0.384
90	625	-0.435
100	513	-0.499
110	420	-0.634
120	328	-0.700
130	240	-0.692
140	160	-0.572
150	97	-0.394
160	55	-0.260
170	28	-0.196
180	8	-0.140
190	-6	-0.037

Segment 33

$\theta-\theta_o$, sec	T_w, °F (b)	q, $\frac{Btu}{ft^2\text{-}sec}$
0	74	0.155
10	87	0.271
20	112	0.402
30	150	0.717
40	220	2.239
50	450	3.881
52	525	1.742
54	550	2.920
56	600	2.780
58	644	5.767
60	750	14.01
62	1025	6.706
64	1100	4.566
66	1135	5.054
68	1153	0.889
70	1130	2.124
80	850	-0.055
90	695	-0.495
100	560	-0.677
110	440	-0.648
120	345	-0.586
130	268	-0.559
140	200	-0.475
150	145	-0.384
160	102	-0.311
170	68	-0.207
180	46	-0.153
190	30	-0.117

Segment 34

$\theta-\theta_o$, sec	T_w, °F (b)	q, $\frac{Btu}{ft^2\text{-}sec}$
0	95	0.200
10	112	0.217
20	130	0.357
30	162	0.711
40	230	1.404
50	367	3.853
60	750	5.396
64	925	3.702
68	990	2.017
72	970	1.668
80	914	1.063
90	805	-0.429
98	690	-0.131
102	655	0.654
106	630	-0.111
110	599	-0.233
120	516	-0.574
130	415	-0.635
140	325	-0.497
150	260	-0.456
160	204	-0.373
170	160	-0.352
180	120	-0.289
190	88	-0.165

[a]Where two segment numbers are shown, instrument readings have been averaged.

[b]Smoothed experimental temperatures are presented in these tables.

TABLE IIIa.-Continued

EXPERIMENTAL TEMPERATURE AND CONVECTIVE HEATING RATE HISTORIES, MA-2

Segment 35-36[a]			Segment 37-38[a]			Segment 39			Segment 40		
$\theta-\theta_o$, sec	T_w, °F (b)	q, $\frac{Btu}{ft^2\text{-}sec}$	$\theta-\theta_o$, sec	T_w, °F (b)	q, $\frac{Btu}{ft^2\text{-}sec}$	$\theta-\theta_o$, sec	T_w, °F (b)	q, $\frac{Btu}{ft^2\text{-}sec}$	$\theta-\theta_o$, sec	T_w, °F (b)	q, $\frac{Btu}{ft^2\text{-}sec}$
0	163	0.201	0	130	0.233	0	70	0.172	0	98	0.425
10	177	0.239	10	149	0.264	10	85	0.270	10	139	0.541
20	194	0.396	20	170	0.600	20	110	0.410	20	190	0.767
30	226	0.536	30	225	0.755	30	149	0.633	30	265	1.417
40	270	0.825	40	292	1.108	40	210	1.030	40	400	0.668
50	340	1.462	50	390	2.056	50	310	1.180	44	415	0.788
60	468	1.964	60	575	3.971	58	395	0.857	48	435	1.980
62	500	0.849	70	887	1.818	64	431	-0.055	50	470	2.288
66	515	0.508	80	756	-0.336	70	405	-0.333	60	670	3.750
68	516	0.428	90	610	-0.422	76	365	0.495	62	730	2.770
70	515	0.227	100	505	-0.450	84	389	0.098	64	764	1.549
74	505	0.115	110	420	-0.494	90	378	-0.012	66	770	0.426
80	485	-0.095	120	344	-0.466	100	350	-0.188	70	735	-0.168
90	435	0.686	130	280	-0.490	110	307	-0.366	80	605	-0.122
100	475	-1.222	140	219	-0.376	120	250	-0.447	90	528	-0.084
110	310	-0.386	150	174	-0.338	130	190	-0.396	100	473	-0.395
120	258	-0.424	160	135	-0.256	140	140	-0.374	110	395	-0.441
130	205	-0.379	170	106	-0.187	150	95	-0.271	120	325	-0.470
140	160	-0.312	180	85	-0.143	160	63	-0.224	130	260	-0.439
150	124	-0.252	190	69	-0.097	170	37	-0.142	140	204	-0.378
160	95	-0.182				180	20.5	-0.144	150	158	-0.332
170	75	-0.133				190	4	-0.059	160	119	-0.242
180	60	-0.076							170	91	-0.258
190	51	-0.038							180	62	-0.143
									190	46	-0.117

[a] Where two segment numbers are shown, instrument readings have been averaged.

[b] Smoothed experimental temperatures are presented in these tables.

TABLE IIIa.-Concluded

EXPERIMENTAL TEMPERATURE AND CONVECTIVE HEATING RATE HISTORIES, MA-2

Segment 41			Segment 42		
$\theta-\theta_o$, sec	T_w, °F (b)	q, $\frac{Btu}{ft^2\text{-sec}}$	$\theta-\theta_o$, sec	T_w, °F (b)	q, $\frac{Btu}{ft^2\text{-sec}}$
0	100	0.089	0	151	0.089
10	105	0.138	10	154	0.120
20	115	0.162	20	160	0.162
30	127	0.271	30	170	0.313
40	150	0.451	40	195	0.426
50	191	0.824	50	230	0.886
60	269	0.943	60	310	1.059
70	353	0.534	70	400	0.645
80	384	0.456	80	436	0.579
88	400	0.287	84	446	0.327
92	400	0.119	88	445	0.272
100	386	0.098	92	442	0.251
110	369	0.016	100	435	0.165
120	346	-0.034	110	419	0.058
130	321	-0.072	120	395	-0.087
140	295	-0.136	130	360	-0.136
150	265	-0.154	140	325	-0.098
160	236	-0.148	150	298	-0.094
170	210	-0.118	160	274	-0.085
180	189	-0.101	170	253	-0.090
190	171	-0.044	180	233	-0.084
			190	215	-0.095

[b]Smoothed experimental temperatures are presented in these tables.

TABLE IIIb

EXPERIMENTAL TEMPERATURE AND CONVECTIVE HEATING RATE HISTORIES, MA-5

$\theta-\theta_o$	Segment 28		Segments 32-33[a]		Segment 34		Segment 35	
sec	T_w °F (b)	q $\frac{Btu}{ft^2\text{-sec}}$	T_w °F (b)	q $\frac{Btu}{ft^2\text{-sec}}$	T_w °F (b)	q $\frac{Btu}{ft^2\text{-sec}}$	T_w °F (b)	q $\frac{Btu}{ft^2\text{-sec}}$
0	44	0.115	100	0.042	235	0.100	110	0.452
10	45	0.202	100	0.042	235	0.100	110	0.452
20	47	0.203	100	0.042	235	0.100	110	0.452
30	49	0.204	100	0.042	235	0.100	110	0.452
40	51	0.204	100	0.042	235	0.100	110	0.452
50	53	0.205	100	0.042	235	0.100	110	0.452
60	55	0.118	100	0.052	235	0.100	110	0.452
70	56	0.118	101	0.052	235	0.110	110	0.641
80	57	0.206	102	0.062	236	0.111	112	0.746
90	59	0.207	104	0.053	237	0.112	115	1.137
100	61	0.207	105	0.063	238	0.112	122	1.266
110	63	0.208	107	0.073	239	0.113	130	1.397
120	65	0.208	110	0.074	240	0.124	139	1.439
130	67	0.209	113	0.085	242	0.135	148	1.574
140	69	0.122	117	0.115	245	0.158	158	1.717
150	70	0.297	124	0.156	250	0.273	169	2.244
160	73	0.385	135	0.236	266	0.328	185	2.998
170	77	0.212	154	0.265	286	0.355	208	3.337
180	79	0.387	175	0.333	307	0.394	233	5.679
190	83	0.301	202	0.424	330	0.446	281	6.194
200	86	0.302	237	0.487	356	0.474	330	7.518
210	89	0.390	276	0.565	382	0.523	388	8.006
220	93	0.392	320	0.607	410	0.570	444	7.557
230	97	0.481	364	0.634	439	0.652	487	7.325
240	102	0.570	406	0.665	472	0.644	520	7.416
250	108	0.659	446	0.677	499	0.627	548	7.625
260	115	0.662	481	0.659	520	0.592	573	8.107
270	122	0.665	508	0.675	534	0.523	598	8.651
280	129	0.755	532	0.640	539	0.516	623	9.223
290	137	0.846	548	0.609	543	0.540	648	9.541

[a]Where two segment numbers are shown, instrument readings have been averaged.

[b]Smoothed experimental temperatures are presented in these tables.

TABLE IIIb.-Continued

EXPERIMENTAL TEMPERATURE AND CONVECTIVE HEATING RATE HISTORIES, MA-5

$\theta-\theta_o$, sec	Segment 38 T_w, °F (b)	Segment 38 q, $\frac{Btu}{ft^2\text{-sec}}$	Segment 39 T_w, °F (b)	Segment 39 q, $\frac{Btu}{ft^2\text{-sec}}$	Segment 40 T_w, °F (b)	Segment 40 q, $\frac{Btu}{ft^2\text{-sec}}$	Segment 41 T_w, °F (b)	Segment 41 q, $\frac{Btu}{ft^2\text{-sec}}$
0	105	0.044	145	0.057	105	0.044	225	0.094
10	105	0.044	145	0.057	105	0.044	225	0.094
20	105	0.044	145	0.057	105	0.044	225	0.094
30	105	0.044	145	0.057	105	0.044	225	0.094
40	105	0.044	145	0.057	105	0.044	225	0.094
50	105	0.044	145	0.057	105	0.044	225	0.094
60	105	0.044	145	0.086	105	0.044	225	0.104
70	105	0.044	148	0.088	105	0.044	226	0.105
80	105	0.044	151	0.099	105	0.044	227	0.106
90	105	0.044	155	0.101	105	0.072	228	0.107
100	105	0.044	159	0.113	108	0.064	229	0.107
110	105	0.072	164	0.125	110	0.065	230	0.108
120	108	0.073	170	0.148	112	0.075	232	0.129
130	111	0.103	178	0.162	115	0.095	235	0.202
140	117	0.114	187	0.215	120	0.154	245	0.220
150	126	0.185	201	0.282	131	0.235	256	0.329
160	140	0.258	221	0.334	150	0.301	277	0.358
170	161	0.307	245	0.419	175	0.456	299	0.387
180	186	0.397	276	0.513	215	0.567	322	0.499
190	219	0.503	314	0.616	265	0.701	354	0.674
200	261	0.658	359	0.808	324	0.899	400	0.822
210	316	0.767	419	1.032	398	0.998	455	0.937
220	377	0.760	494	0.970	473	0.878	513	0.771
230	430	0.695	549	0.912	523	0.770	544	0.742
240	469	0.728	587	0.869	552	0.884	567	0.763
250	505	0.742	613	0.816	588	0.902	588	0.825
260	536	0.797	628	0.793	618	0.969	611	0.875
270	567	0.801	638	0.886	648	1.032	634	0.909
280	592	0.872	656	0.998	677	1.097	655	1.040
290	619	0.906	681	1.078	705	1.174	684	1.142

[b]Smoothed experimental temperatures are presented in these tables.

TABLE IIIb.-Continued

EXPERIMENTAL TEMPERATURE AND CONVECTIVE HEATING RATE HISTORIES, MA-5

$\theta-\theta_o$, sec	Segment 28 T_w, °F (b)	Segment 28 q, Btu/ft²-sec	Segments 32-33[a] T_w, °F (b)	Segments 32-33[a] q, Btu/ft²-sec	Segment 34 T_w, °F (b)	Segment 34 q, Btu/ft²-sec	Segment 35 T_w, °F (b)	Segment 35 q, Btu/ft²-sec
300	146	0.850	558	0.586	549	0.550	670	1.018
310	155	0.941	564	0.547	555	0.570	693	1.062
320	165	0.859	565	0.552	562	0.613	714	1.093
330	174	0.950	567	0.561	572	0.684	734	1.173
340	184	0.956	570	0.640	587	0.809	753	1.108
350	194	1.136	581	0.759	611	0.927	760	1.024
360	206	1.056	602	0.867	641	1.057	757	0.890
370	217	1.412	629	1.030	676	1.166	742	0.751
380	232	2.295	666	1.209	712	1.295	719	0.601
390	257	2.577	711	1.396	750	1.441	689	0.521
400	285	3.037	761	1.614	790	1.625	661	0.582
410	318	4.116	816	1.837	834	1.973	648	0.657
420	363	7.920	872	2.107	895	2.794	646	0.716
430	451	6.750	931	1.842	1009	2.273	650	0.563
440	524	4.183	931	1.010	1004	0.839	636	0.360
450	566	2.520	852	0.611	921	1.438	605	0.153
460	588	1.248	765	0.136	822	-0.368	561	0.085
470	595	0.640	683	0.028	723	0.172	521	0.035
480	595	0.453	607	-0.135	640	-0.319	484	-0.009
490	593	-8.630	537	-0.343	556	-0.336	449	-0.174

[a]Where two segment numbers are shown, instrument readings have been averaged.

[b]Smoothed experimental temperatures are presented in these tables.

TABLE IIIb.-Concluded

EXPERIMENTAL TEMPERATURE AND CONVECTIVE HEATING RATE HISTORIES, MA-5

$\theta-\theta_o$, sec	Segment 38		Segment 39		Segment 40		Segment 41	
	T_w, °F (b)	q, $\frac{Btu}{ft^2\text{-}sec}$	T_w, °F (b)	q, $\frac{Btu}{ft^2\text{-}sec}$	T_w, °F (b)	q, $\frac{Btu}{ft^2\text{-}sec}$	T_w, °F (b)	q, $\frac{Btu}{ft^2\text{-}sec}$
300	643	0.961	707	1.163	733	1.269	715	1.214
310	667	1.022	734	1.265	762	1.325	744	1.265
320	691	1.058	763	1.264	787	1.426	769	1.294
330	712	1.108	782	1.294	814	1.497	789	1.359
340	732	1.053	798	1.336	838	1.549	809	1.419
350	740	0.870	813	1.378	858	1.597	828	1.459
360	727	0.687	827	1.419	875	1.608	844	1.428
370	701	0.574	840	1.391	886	1.582	851	1.347
380	673	0.552	845	1.306	890	1.441	848	1.162
390	652	0.570	840	0.571	878	1.084	829	0.665
400	639	0.585	762	0.374	836	0.463	770	0.621
410	631	0.662	700	0.679	750	0.616	732	0.681
420	633	0.674	690	0.887	718	0.906	712	0.768
430	635	0.465	702	0.584	725	0.765	706	0.509
440	614	0.253	677	0.353	712	0.401	675	0.369
450	577	0.150	637	0.199	665	0.210	640	0.252
460	539	0.162	593	0.148	614	0.142	603	0.181
470	511	0.113	555	0.031	570	0.055	568	0.056
480	483	-0.019	513	-0.059	527	0.402	528	0.027
490	446	-0.144	470	-0.045			493	-0.082

[b] Smoothed experimental temperatures are presented in these tables.

TABLE IIIc

EXPERIMENTAL TEMPERATURE AND CONVECTIVE HEATING RATE HISTORIES, MA-7

$\theta-\theta_o$, sec	Segment 7 T_w, °F (b)	Segment 7 q, $\frac{Btu}{ft^2-sec}$	Segment 8 T_w, °F (b)	Segment 8 q, $\frac{Btu}{ft^2-sec}$	Segment 9 T_w, °F (b)	Segment 9 q, $\frac{Btu}{ft^2-sec}$	Segment 10 T_w, °F (b)	Segment 10 q, $\frac{Btu}{ft^2-sec}$
0	45	0.028	78	0.036	62	0.032	129	-0.092
10	45	0.028	78	0.036	62	0.032	114	-0.081
20	45	0.028	78	0.036	62	0.032	101	-0.053
30	45	0.028	78	0.036	62	0.041	91.5	-0.022
40	45	0.028	78	0.036	63	0.041	85.5	0.029
50	45	0.028	78	0.036	64	0.042	85	0.035
60	45	0.028	78	0.036	65	0.051	85	0.102
70	45	0.037	78	0.036	67	0.052	92	0.115
80	46	0.037	78	0.036	69	0.043	100	0.224
90	47	0.038	78	0.036	70	0.053	119	0.099
100	48	0.038	78	0.036	72	0.063	117	0.034
110	49	0.038	78	0.036	75	0.073	115	0.047
120	50	0.057	78	0.045	79	0.083	115	0.071
130	53	0.058	79	0.055	84	0.085	118	0.125
140	56	0.068	81	0.083	89	0.096	126	0.196
150	60	0.132	86	0.150	95	0.108	141	0.289
160	71	0.326	98	0.165	102	0.138	165	0.398
170	103	0.503	111	0.207	112	0.160	199	0.391
180	153	0.584	128	0.270	124	0.184	230	0.387
190	209	0.646	151	0.300	138	0.209	258	0.364
200	268	0.636	176	0.471	154	0.225	282	0.440
210	321	0.684	218	0.508	171	0.280	312	0.496
220	374	0.733	261	0.578	193	0.302	345	0.567
230	426	0.798	308	0.694	216	0.344	382	0.700
240	478	0.821	363	0.763	242	0.463	429	0.798
250	523	0.886	419	0.879	279	0.558	479	0.939
260	566	0.964	480	0.888	323	0.656	535	0.876
270	608	1.002	531	0.772	373	0.794	573	0.805
280	644	1.070	559	0.735	432	0.535	596	0.752
290	678	1.123	578	0.682	454	0.498	609	0.474

[b]Smoothed experimental temperatures are presented in these tables.

TABLE IIIc.-Continued

EXPERIMENTAL TEMPERATURE AND CONVECTIVE HEATING RATE HISTORIES, MA-7

$\theta-\theta_o$, sec	Segments 11-1[a] T_w, °F [b]	Segments 11-1[a] q, Btu/ft²-sec	Segments 11-2[a] T_w, °F [b]	Segments 11-2[a] q, Btu/ft²-sec	Segment 12 T_w, °F [b]	Segment 12 q, Btu/ft²-sec	Segment 13 T_w, °F [b]	Segment 13 q, Btu/ft²-sec
0	95	0.039	100	0.042	80	0.019	75	0.035
10	95	0.039	100	0.042	80	0.047	75	0.035
20	95	0.039	100	0.042	80	0.044	75	0.035
30	95	0.039	100	0.042	80	0.042	75	0.035
40	95	0.039	100	0.042	80	0.041	75	0.035
50	95	0.039	100	0.061	80	0.041	75	0.035
60	95	0.043	102	0.071	80	0.041	75	0.035
70	95	0.044	105	0.063	80	0.040	75	0.035
80	95	0.044	107	0.073	80	0.040	75	0.040
90	95	0.050	110	0.084	80	0.040	75	0.040
100	96	0.074	114	0.067	80	0.040	76	0.054
110	100	0.080	116	0.086	80	0.040	78	0.055
120	103	0.077	120	0.097	80	0.039	80	0.069
130	107	0.116	125	0.100	80	0.039	83	0.071
140	114	0.119	130	0.111	80	0.057	87	0.072
150	122	0.155	136	0.132	82	0.067	90	0.119
160	133	0.188	144	0.127	85	0.122	99	0.118
170	147	0.223	151	0.163	94	0.117	107	0.158
180	164	0.241	161	0.196	102	0.156	119	0.178
190	182	0.293	175	0.227	114	0.171	132	0.253
200	204	0.298	191	0.288	127	0.221	153	0.268
210	226	0.382	212	0.312	145	0.248	175	0.335
220	255	0.404	235	0.426	165	0.286	202	0.356
230	284	0.456	268	0.490	188	0.330	230	0.435
240	316	0.522	305	0.505	214	0.347	265	0.513
250	352	0.597	340	0.538	241	0.424	305	0.595
260	392	0.625	375	0.614	274	0.469	350	0.513
270	430	0.649	414	0.635	309	0.528	381	0.479
280	465	0.704	450	0.633	347	0.495	405	0.421
290	500	0.718	480	0.672	371	0.392	420	0.394

[a]Where two segment numbers are shown, instrument readings have been averaged.

[b]Smoothed experimental temperatures are presented in these tables.

TABLE III c.-Continued

EXPERIMENTAL TEMPERATURE AND CONVECTIVE HEATING RATE HISTORIES, MA-7

$\theta-\theta_o$, sec	Segment 14		Segment 20		Segment 21		Segment 22		Segment 23	
	T_w, °F (b)	q, $\frac{Btu}{ft^2\text{-sec}}$	T_w, °F (b)	q, $\frac{Btu}{ft^2\text{-sec}}$	T_w, °F (b)	q, $\frac{Btu}{ft^2\text{-sec}}$	T_w, °F (b)	q, $\frac{Btu}{ft^2\text{-sec}}$	T_w, °F (b)	q, $\frac{Btu}{ft^2\text{-sec}}$
0	90	0.047	50	0.029	92	0.044	75	0.058	70	0.034
10	90	0.047	50	0.029	92	0.044	75	0.059	70	0.034
20	90	0.048	50	0.029	92	0.044	75	0.059	70	0.034
30	90	0.048	50	0.029	92	0.044	75	0.059	70	0.034
40	90	0.048	50	0.029	92	0.044	75	0.059	70	0.034
50	90	0.049	50	0.029	92	0.044	75	0.059	70	0.034
60	95	0.057	50	0.029	92	0.044	75	0.059	70	0.034
70	96	0.057	50	0.029	92	0.044	75	0.059	70	0.034
80	98	0.058	50	0.117	92	0.044	77	0.315	70	0.034
90	100	0.066	50	0.118	92	0.044	80	0.223	70	0.218
100	102.5	0.067	52	0.096	92	0.044	82	0.317	72	0.127
110	105	0.101	52	0.096	92	0.044	85	0.412	73	0.219
120	111	0.104	52	0.096	92	0.056	89	0.367	75	0.220
130	117	0.125	52	0.097	92	0.056	92	0.321	77	0.313
140	125	0.138	55	0.119	92	0.056	95	0.322	80	0.222
150	134	0.179	56	0.208	92	0.056	98	0.183	82	0.315
160	147	0.223	58	0.164	92	0.056	100	0.277	85	0.224
170	164	0.232	60	0.165	92	0.056	102	0.231	87	0.270
180	181	0.189	61	0.298	93	0.137	104	0.139	90	0.225
190	192	0.158	64	0.166	93	0.137	105	0.232	92	0.272
200	200	0.166	66	0.343	95	0.234	108	0.279	94	0.227
210	208	0.244	69	0.300	97	0.331	110	0.094	96	0.412
220	224	0.349	72	0.301	100	0.284	110	0.280	100	0.183
230	250	0.537	75	0.479	102	0.333	113	0.235	102	0.367
240	294	0.512	80	0.525	105	0.383	115	0.515	105	0.277
250	331	0.528	86	0.615	109	0.577	120	0.611	108	0.277
260	366	0.527	92	0.750	114	0.531	126	1.079	110	0.463
270	397	0.506	100	0.753	119	0.581	137	0.805	114	0.326
280	422	0.548	108	0.668	125	0.632	145	0.529	117	0.558
290	448	0.559	115	0.671	131	0.827	150	0.531	123	0.699

[b] Smoothed experimental temperatures are presented in these tables.

TABLE IIIc.-Continued

EXPERIMENTAL TEMPERATURE AND CONVECTIVE HEATING RATE HISTORIES, MA-7

$\theta-\theta_o$, sec	Segment 7 T_w, °F (b)	Segment 7 q, $\frac{Btu}{ft^2\text{-sec}}$	Segment 8 T_w, °F (b)	Segment 8 q, $\frac{Btu}{ft^2\text{-sec}}$	Segment 9 T_w, °F (b)	Segment 9 q, $\frac{Btu}{ft^2\text{-sec}}$	Segment 10 T_w, °F (b)	Segment 10 q, $\frac{Btu}{ft^2\text{-sec}}$
300	708	1.042	588	0.714	469	-0.039	600	0.852
310	720	1.189	600	0.793		0.468	625	0.965
320	746	1.419	618	0.935	517	0.905	655	1.035
330	788	1.628	647	1.075	552	0.921	684	1.115
340	836	1.910	683	1.168	592	1.057	713	1.181
350	894	2.035	718	1.190	638	1.032	740	1.245
360	937	2.055	744	1.138	669	0.850	765	0.995
370	961	2.103	756	1.063	672	0.846	756	1.019
380	978	2.185	757	1.089	676	0.920	756	1.139
390	998	2.487	762	1.166	688	1.026	768	1.283
400	1029	2.125	774	1.282	708	1.242	790	1.321
410	1067	4.461	794	1.468	745	1.450	808	1.377
420	1115	1.876	826	1.571	791	1.280	824	1.422
430	1170	5.484	855	1.338	800	1.161	839	1.424
440	1185	5.539	846	1.093	795	1.090	842	1.313
450	1184	5.372	818	0.454	786	1.010	815	0.613
460	1166	5.007	735	0.215	773	0.909	754	1.520
470	1134	4.394	663	0.353	755	0.793	691	0.516
480	1079	4.051	629	0.781	732	0.674	666	0.539
490	1057	4.076	649	0.872	705	0.539	680	1.240
500	1064	3.327	670	0.312	632	0.414	665	0.319
510	980	2.154	623	0.069	638	0.318	625	0.115
520	858	1.273	566	-0.032	603	0.215	575	-0.006
530	746	0.761	513	-0.098	566	0.114	525	-0.153
540	653	0.465	464	-0.120	527	0.037	470	-0.378
550	576	0.446	421	-0.132	488	-0.40	410	-0.278
560	529	0.289	383	-0.202	448	-0.129	399	-0.283
570	482	0.080	342	-0.484	405	-0.177	349	-0.455
580	425	-0.124	275	-0.537	363	-0.225	287	-0.657
590	360	-0.346	209	-0.495	321	-0.346	210	-0.880

[b]Smoothed experimental temperatures are presented in these tables.

TABLE IIIc.-Continued

EXPERIMENTAL TEMPERATURE AND CONVECTIVE HEATING RATE HISTORIES, MA-7

$\theta-\theta_o$, sec	Segments 11-1[a]		Segments 11-2[a]		Segment 12		Segment 13	
	T_w, °F (b)	q, $\frac{\text{Btu}}{\text{ft}^2\text{-sec}}$	T_w, °F (b)	q, $\frac{\text{Btu}}{\text{ft}^2\text{-sec}}$	T_w, °F (b)	q, $\frac{\text{Btu}}{\text{ft}^2\text{-sec}}$	T_w, °F (b)	q, $\frac{\text{Btu}}{\text{ft}^2\text{-sec}}$
300	530	0.747	509	0.646	391	0.455	430	0.562
310	557.5	0.752	530	0.717	412	0.587	457	0.594
320	580	0.735	555	0.696	445	0.683	438	0.484
330	592.5	0.670	572.5	0.682	470	0.468	485	0.392
340	589	0.782	585	0.671	479	0.397	483	0.303
350	610	0.827	594	0.625	480	0.359	475	0.320
360	630	0.875	596.5	0.614	477	0.311	470	0.344
370	650	0.878	598	0.495	470	0.317	470	0.380
380	665	0.881	587	0.320	466	0.344	473	0.376
390	676.5	0.859	561	0.247	465	0.383	475	0.424
400	673.5	0.613	551	0.610	469	0.453	482	0.436
410	653	0.439	564.5	0.431	480	0.536	489	0.475
420	624	0.314	561	0.616	498	0.516	499	0.498
430	599	0.497	573	0.730	510	0.586	509	0.554
440	595	0.573	594	0.969	527	0.531	524	0.596
450	596	0.606	635	1.108	535	0.564	540	0.665
460	600	0.665	679	1.160	545	0.602	560	0.736
470	609	0.708	715	1.182	557	0.726	583	0.848
480	620	0.822	742	1.200	580	0.935	612	1.111
490	640	0.879	743	0.614	670	1.573	669	1.372
500	639	0.350	705	0.426	735	0.982	711	1.092
510	604	0.203	660	0.256	704	0.312	686	0.324
520	564	0.070	612	0.090	640	-0.001	632	0.075
530	520	-0.049	560	-0.058	572	0.145	570	-0.176
540	473	-0.151	505	-0.189	531	0.008	497	-0.371
550	424	-0.261	447.5	-0.328	485	-0.158	420	-0.423
560	371	-0.354	385	-0.415	430	-0.380	350	-0.484
570	315	-0.400	322	-0.469	360	-0.425	282	-0.487
580	260	-0.462	260	-0.489	295	-0.643	220	-0.527
590	203	-0.505	201	-0.409	212	-0.747	158	-0.449

[a]Where two segment numbers are shown, instrument readings have been averaged.

[b]Smoothed experimental temperatures are presented in these tables.

TABLE IIIc.-Concluded

EXPERIMENTAL TEMPERATURE AND CONVECTIVE HEATING RATE HISTORIES, MA-7

$\theta-\theta_o$, sec	Segment 14		Segment 20		Segment 21		Segment 22		Segment 23	
	T_w, °F (b)	q, $\frac{Btu}{ft^2-sec}$	T_w, °F (b)	q, $\frac{Btu}{ft^2-sec}$	T_w, °F (b)	q, $\frac{Btu}{ft^2-sec}$	T_w, °F (b)	q, $\frac{Btu}{ft^2-sec}$	T_w, °F (b)	q, $\frac{Btu}{ft^2-sec}$
300	471	0.557	122	0.850	139	0.734	155	0.533	130	1.117
310	490	0.641	131	0.810	146	0.834	160	0.535	141	0.385
320	515	0.601	139	0.902	154	0.789	165	0.537	145	0.985
330	531	0.618	149	0.773	161.5	0.889	170	0.539	155	1.082
340	546	0.580	157	0.777	170	0.893	175	0.542	166	1.180
350	550	0.412	165	1.090	178.5	0.850	180	0.638	178	1.187
360	540	0.383	176	1.008	186.5	0.902	186	0.734	190	1.170
370	530	0.405	187	1.102	195	1.003	193	0.738	205	1.479
380	525	0.412	198	1.108	204.5	0.623	200	0.742	220	1.489
390	522	0.415	210	1.336	210	1.493	207	0.839	235	1.499
400	520	0.428	224	1.522	224.5	1.166	215	1.031	250	1.786
410	520	0.438	240	1.445	235.5	1.318	225	1.270	268	1.616
420	521	0.462	255	1.898	248	1.278	237	1.419	284	1.720
430	524	0.511	274	2.003	260	1.673	251	1.849	301	1.919
440	532	0.571	296	2.684	276	1.976	270	1.864	320	2.399
450	545	0.705	324	3.155	295	2.378	288	2.160	344	2.978
460	569	0.825	358	3.944	318	3.075	310	2.413	374	3.568
470	600	1.031	400	4.706	348	4.073	334	2.438	410	4.447
480	645	1.261	450	6.374	388	5.522	358	3.024	455	5.672
490	701	1.169	518	7.742	442	7.822	410	6.597	512	6.242
500	705	0.324	600	5.108	520	5.321	477	4.786	575	5.318
510	666	0.366	640	2.985	556	2.170	520	2.820	626	1.737
520	625	0.163	650	0.781	570	1.064	536	0.978	633	1.022
530	575	0.038	650	0.766	575	0.582	540	0.509	635	0.771
540	525	-0.160	650	0.359	575	0.140	539	0.314	636	0.717
550	465	-0.314	645	0.249	570	0.073	537	-0.162	636	0.710
560	400	-0.406	640	-0.170	565	-0.473	530	-0.229	635	0.613
570	335	-0.430	630	-0.425	555	-0.454	523	-0.481	635	0.697
580	275	-0.591	617	-0.680	545	-0.861	513	-0.548	628	-1.263
590	203	-0.553	602	-0.722	531	-0.990	502	-0.757	607	-1.878

[b] Smoothed experimental temperatures are presented in these tables.

TABLE IIId

EXPERIMENTAL TEMPERATURE AND CONVECTIVE HEATING RATE HISTORIES, MA-8

$\theta-\theta_o$, sec	Segment 3 T_w, °F (b)	Segment 3 q, $\frac{Btu}{ft^2-sec}$	Segment 7 T_w, °F (b)	Segment 7 q, $\frac{Btu}{ft^2-sec}$	Segment 8 T_w, °F (b)	Segment 8 q, $\frac{Btu}{ft^2-sec}$	Segment 10 T_w, °F (b)	Segment 10 q, $\frac{Btu}{ft^2-sec}$
0	50	0.029	25	0.024	-40	0.013	35	0.026
10	50	0.029	25	0.024	-40	0.013	35	0.026
20	50	0.029	25	0.024	-40	0.013	35	0.026
30	50	0.038	25	0.024	-40	0.013	35	0.026
40	51	0.038	25	0.033	-40	0.013	35	0.026
50	52	0.039	26	0.033	-40	0.013	35	0.026
60	53	0.039	27	0.033	-40	0.022	35	0.026
70	54	0.039	28	0.034	-39	0.023	35	0.026
80	55	0.040	29	0.034	-38	0.032	35	0.035
90	56	0.058	30	0.034	-36	0.050	36	0.044
100	59	0.059	31	0.043	-32	0.060	38	0.036
110	62	0.060	33	0.053	-27	0.088	39	0.045
120	65	0.070	36	0.072	-19	0.099	41	0.055
130	69	0.081	41	0.119	-10	0.164	44	0.074
140	74	0.091	51	0.185	6	0.195	49	0.084
150	80	0.103	68	0.236	25	0.237	55	0.113
160	87	0.141	90	0.326	48	0.307	64	0.152
170	98	0.164	121	0.421	78	0.426	77	0.211
180	111	0.197	161	0.532	120	0.508	96	0.291
190	127	0.240	211	0.654	169	0.660	123	0.303
200	147	0.286	271	0.719	232	0.956	150	0.325
210	171	0.353	333	0.761	323	0.898	178	0.340
220	201	0.408	393	0.795	398	0.806	206	0.365
230	235	0.476	449	0.835	453	0.777	235	0.411
240	274	0.535	501	0.848	497	0.774	267	0.436
250	316	0.574	544	0.912	532	0.837	299	0.455
260	358	0.663	585	0.924	567	0.879	330	0.484
270	405	0.738	618	0.941	599	0.944	361	0.417
280	454	0.812	645	1.022	631	0.984	381	0.389
290	503	0.882	674	1.070	659	1.062	396	0.368

[b] Smoothed experimental temperatures are presented in these tables.

TABLE IIId.-Continued

EXPERIMENTAL TEMPERATURE AND CONVECTIVE HEATING RATE HISTORIES, MA-8

$\theta-\theta_o$, sec	Segment 11		Segment 12		Segment 13		Segment 14		Segment 15	
	T_w, °F (b)	q, $\frac{Btu}{ft^2\text{-}sec}$	T_w, °F (b)	q, $\frac{Btu}{ft^2\text{-}sec}$	T_w, °F (b)	q, $\frac{Btu}{ft^2\text{-}sec}$	T_w, °F (b)	q, $\frac{Btu}{ft^2\text{-}sec}$	T_w, °F (b)	q, $\frac{Btu}{ft^2\text{-}sec}$
0	-28	0.034	-25	0.015	43	0.027	50	0.029	35	0.026
10	-26	0.034	-25	0.015	43	0.027	50	0.029	35	0.026
20	-25	0.034	-25	0.015	43	0.027	50	0.029	35	0.026
30	-23	0.034	-25	0.015	43	0.027	50	0.029	35	0.026
40	-21	0.043	-25	0.015	43	0.027	50	0.029	35	0.026
50	-18	0.044	-25	0.015	43	0.027	50	0.029	35	0.044
60	-15	0.045	-25	0.015	43	0.027	50	0.029	37	0.044
70	-12	0.045	-25	0.015	43	0.027	50	0.029	39	0.054
80	-9	0.064	-25	0.015	43	0.027	50	0.038	42	0.055
90	-4	0.056	-25	0.015	43	0.027	51	0.038	45	0.065
100	0	0.066	-25	0.015	43	0.027	52	0.057	49	0.075
110	5	0.094	-25	0.015	43	0.027	55	0.058	54	0.086
120	13	0.078	-25	0.102	43	0.027	58	0.068	60	0.097
130	19	0.107	-24	0.188	43	0.027	62	0.106	67	0.126
140	28	0.136	-22	0.189	43	0.201	70	0.136	77	0.148
150	40	0.158	-20	0.189	45	0.202	81	0.176	85	0.206
160	54	0.207	-18	0.190	47	0.203	96	0.264	107	0.259
170	73	0.241	-16	0.190	49	0.290	120	0.293	130	0.297
180	95	0.313	-14	0.450	52	0.291	146	0.378	156	0.328
190	124	0.353	9	0.278	55	0.379	180	0.442	184	0.370
200	156	0.396	6	0.192	59	0.381	219	0.495	215	0.416
210	191	0.452	4	0.625	63	0.295	261	0.535	249	0.458
220	230	0.504	3	0.454	66	0.383	304	0.591	285	0.497
230	272	0.528	8	0.541	70	0.384	349	0.628	322	0.550
240	313	0.593	14	0.716	74	0.472	393	0.687	361	0.609
250	357	0.685	22	0.545	79	0.648	438	0.767	402	0.667
260	406	0.708	28	0.719	86	0.651	485	0.785	444	0.755
270	451	0.638	36	0.808	93	0.653	525	0.822	489	0.788
280	481	0.622	45	0.897	100	0.656	561	0.864	529	0.809
290	504	0.587	55	0.727	107	0.745	594	0.833	563	0.801

[b]Smoothed experimental temperatures are presented in these tables.

TABLE IIId.-Continued

EXPERIMENTAL TEMPERATURE AND CONVECTIVE HEATING RATE HISTORIES, MA-8

$\theta-\theta_o$, sec	Segment 20		Segment 22		Segment 24		Segment 25		Segment 26	
	T_w, °F (b)	q, $\frac{Btu}{ft^2\text{-sec}}$	T_w, °F (b)	q, $\frac{Btu}{ft^2\text{-sec}}$	T_w, °F (b)	q, $\frac{Btu}{ft^2\text{-sec}}$	T_w, °F (b)	q, $\frac{Btu}{ft^2\text{-sec}}$	T_w, °F (b)	q, $\frac{Btu}{ft^2\text{-sec}}$
0	-25	0.015	17	0.022	190	0.076	45	0.028	38	0.026
10	-25	0.015	17	0.022	190	0.076	45	0.028	38	0.026
20	-25	0.015	17	0.022	190	0.076	45	0.028	38	0.026
30	-25	0.015	17	0.022	190	0.086	45	0.028	38	0.026
40	-25	0.015	17	0.022	191	0.097	45	0.028	38	0.026
50	-25	0.015	17	0.031	193	0.098	45	0.028	38	0.113
60	-25	0.024	18	0.041	195	0.099	45	0.028	39	0.027
70	-24	0.034	20	0.032	197	0.110	45	0.028	40	0.113
80	-22	0.034	21	0.032	200	0.132	45	0.028	40	0.113
90	-20	0.035	22	0.033	205	0.135	45	0.028	41	0.114
100	-18	0.044	23	0.051	210	0.148	45	0.028	42	0.114
110	-15	0.045	26	0.061	216	0.182	45	0.028	43	0.114
120	-12	0.054	30	0.080	225	0.208	45	0.208	44	0.115
130	-8	0.073	36	0.100	236	0.245	45	0.115	45	0.115
140	-2	0.093	44	0.174	250	0.295	46	0.116	46	0.115
150	6	0.122	60	0.198	268	0.320	47	0.116	47	0.115
160	17	0.161	78	0.268	287	0.385	48	0.204	48	0.202
170	32	0.210	103	0.305	311	0.407	50	0.204	50	0.203
180	52	0.271	131	0.363	335	0.469	52	0.205	52	0.290
190	78	0.307	164	0.416	363	0.529	54	0.206	55	0.291
200	107	0.364	201	0.465	394	0.619	56	0.294	58	0.292
210	141	0.389	241	0.510	430	0.697	59	0.295	61	0.379
220	176	0.453	283	0.580	469	0.651	62	0.470	65	0.467
230	216	0.468	329	0.644	497	0.665	67	0.559	70	0.641
240	255	0.487	377	0.706	522	0.668	73	0.562	77	0.730
250	293	0.474	426	0.786	543	0.775	79	0.651	85	0.820
260	326	0.505	477	0.809	571	0.825	86	0.828	94	0.909
270	359	0.484	521	0.845	598	0.874	95	0.744	104	1.000
280	386	0.449	560	0.876	624	0.944	103	0.922	115	1.004
290	406	0.415	594	0.882	651	1.011	113	0.839	126	1.095

[b] Smoothed experimental temperatures are presented in these tables.

TABLE IIId.-Continued

EXPERIMENTAL TEMPERATURE AND CONVECTIVE HEATING RATE HISTORIES, MA-8

$\theta-\theta_o$, sec	Segment 3		Segment 7		Segment 8		Segment 10	
	T_w, °F (b)	q, $\frac{Btu}{ft^2-sec}$	T_w, °F (b)	q, $\frac{Btu}{ft^2-sec}$	T_w, °F (b)	q, $\frac{Btu}{ft^2-sec}$	T_w, °F (b)	q, $\frac{Btu}{ft^2-sec}$
300	550	0.975	700	1.148	688	1.104	407	0.363
310	597	1.123	727	1.200	713	1.172	416	0.328
320	649	1.211	751	1.255	738	1.219	420	0.349
330	696	1.314	773	1.317	760	1.251	426	0.338
340	740	1.448	794	1.360	778	1.280	430	0.386
350	784	1.571	812	1.421	793	1.372	439	0.399
360	825	1.678	830	1.479	813	1.456	448	0.475
370	861	1.813	847	1.501	834	1.457	464	0.510
380	896	1.912	859	1.518	846	1.344	481	0.584
390	925	2.005	868	1.218	841	1.099	503	0.661
400	950	2.066	840	0.548	813	0.630	529	0.784
410	968	2.007	755	0.394	748	0.598	563	0.851
420	973	2.050	693	0.392	709	0.599	596	0.991
430	967	1.040	652	0.522	683	0.610	636	1.402
440	948	2.286	637	0.455	666	0.524	710	1.404
450	921	3.328	617	0.318	644	0.349	758	0.917
460	890	1.934	587	0.139	609	0.175	735	0.517
470	853	3.006	545	-0.025	565	0.188	682	0.239
480	813	1.192	495	-0.057	515	-0.081	620	-0.089
490	768	2.501	452	-0.103	465	-0.236	542	-0.329
500	720	1.141	411	0.370	407	0.360	458	0.441

[b]Smoothed experimental temperatures are presented in these tables

TABLE IIId.-Continued

EXPERIMENTAL TEMPERATURE AND CONVECTIVE HEATING RATE HISTORIES, MA-8

$\theta-\theta_o$	Segment 11		Segment 12		Segment 13		Segment 14		Segment 15	
sec	T_w °F (b)	q $\frac{Btu}{ft^2\text{-sec}}$	T_w °F (b)	q $\frac{Btu}{ft^2\text{-sec}}$	T_w °F (b)	q $\frac{Btu}{ft^2\text{-sec}}$	T_w °F (b)	q $\frac{Btu}{ft^2\text{-sec}}$	T_w °F (b)	q $\frac{Btu}{ft^2\text{-sec}}$
300	519	0.535	63	0.643	115	0.748	616	0.842	589	0.780
310	526	0.458	70	0.732	123	0.752	634	0.971	607	0.798
320	524	0.373	78	0.907	131	0.929	662	0.945	623	0.894
330	514	0.373	88	0.738	141	1.020	679	0.883	646	0.717
340	507	0.420	96	0.827	152	1.026	685	0.807	643	0.565
350	507	0.483	105	0.916	163	1.031	682	0.670	626	0.453
360	514	0.525	115	1.007	174	1.036	666	0.558	603	0.470
370	524	0.626	126	1.184	185	1.042	644	0.553	589	0.464
380	543	0.766	139	1.536	196	1.397	629	0.523	578	0.511
390	573	0.822	156	1.805	211	1.581	615	0.396	575	0.633
400	617	1.335	176	2.508	228	1.767	591	0.425	586	0.700
410	690	1.321	204	3.563	247	2.217	577	0.451	601	0.702
420	737	1.402	244	4.372	271	2.585	569	0.474	612	0.486
430	777	1.665	293	5.196	299	4.787	565	0.451	596	0.734
440	831	1.363	351	5.347	352	5.719	559	0.385	613	0.715
450	827	0.593	410	3.611	415	3.892	547	0.177	622	0.376
460	745	0.203	448	2.020	456	1.949	515	0.171	591	0.274
470	660	0.044	467	1.006	474	0.927	490	0.082	559	0.152
480	588	-0.010	474	0.318	480	-0.029	460	-0.059	522	0.038
490	530	0.019	473	0.308	475	-0.221	420	-0.165	481	-0.100
500	488	0.501	472	1.998	468	1.985	375	0.337	433	0.417

[b]Smoothed experimental temperatures are presented in these tables

TABLE IIId.-Continued

EXPERIMENTAL TEMPERATURE AND CONVECTIVE HEATING RATE HISTORIES, MA-8

	Segment 20		Segment 22		Segment 24		Segment 25		Segment 26	
$\theta-\theta_o$ sec	T_w °F (b)	q $\frac{Btu}{ft^2\text{-sec}}$	T_w °F (b)	q $\frac{Btu}{ft^2\text{-sec}}$	T_w °F (b)	q $\frac{Btu}{ft^2\text{-sec}}$	T_w °F (b)	q $\frac{Btu}{ft^2\text{-sec}}$	T_w °F (b)	q $\frac{Btu}{ft^2\text{-sec}}$
300	420	0.432	621	0.942	678	1.064	122	1.104	138	1.100
310	434	0.424	648	1.016	703	1.133	134	1.022	150	1.106
320	445	0.438	676	1.107	728	1.188	145	1.202	162	1.198
330	456	0.444	706	1.146	751	1.249	158	1.121	175	1.204
340	466	0.512	731	1.183	773	1.301	170	1.214	188	1.298
350	482	0.574	752	1.210	793	1.349	183	1.395	202	1.306
360	502	0.645	769	1.108	811	1.413	198	1.929	216	1.487
370	526	0.691	769	0.903	829	1.472	213	1.768	232	1.585
380	550	0.767	748	0.657	846	1.538	238	2.219	249	1.857
390	577	0.872	710	0.725	863	1.194	262	2.588	269	2.133
400	609	0.941	695	0.632	838	0.802	290	3.224	292	2.326
410	640	0.957	674	0.630	788	0.678	325	4.571	317	2.869
420	664	1.002	660	0.604	747	0.590	375	6.032	348	3.509
430	686	1.351	647	0.570	712	0.617	441	7.966	386	6.151
440	740	1.316	634	0.474	691	0.750	528	4.466	454	5.395
450	767	0.955	614	0.350	689	0.363	573	2.630	512	2.996
460	748	0.545	586	0.218	647	0.259	596	1.533	541	1.747
470	694	0.250	551	0.103	608	0.172	606	1.019	555	0.987
480	605	-0.195	512	-0.019	570	0.118	610	0.405	560	0.382
490	521	-0.179	468	-0.167	535	0.089	607	-0.225	558	0.109
500	459	0.447	416	0.382	504	0.533	597	2.462	553	2.275

[b] Smoothed experimental temperatures are presented in these tables

TABLE IIId.-Concluded

EXPERIMENTAL TEMPERATURE AND CONVECTIVE HEATING RATE HISTORIES, MA-8

	Segment 27		Segment 28			Segment 27		Segment 28	
$\theta-\theta_o$, sec	T_w, °F (b)	q, $\frac{Btu}{ft^2-sec}$	T_w, °F (b)	q, $\frac{Btu}{ft^2-sec}$	$\theta-\theta_o$, sec	T_w, °F (b)	q, $\frac{Btu}{ft^2-sec}$	T_w, °F (b)	q, $\frac{Btu}{ft^2-sec}$
0	-30	0.015	-34	0.014	300	548	0.653	665	1.053
10	-30	0.015	-34	0.014	310	560	0.583	690	1.052
20	-30	0.024	-34	0.014	320	563	0.613	708	1.022
30	-29	0.024	-34	0.014	330	570	0.607	718	0.967
40	-28	0.024	-34	0.014	340	575	0.613	720	0.944
50	-27	0.033	-34	0.014	350	580	0.638	720	0.935
60	-25	0.025	-34	0.014	360	587	0.669	720	0.929
70	-24	0.025	-34	0.014	370	596	0.733	720	0.916
80	-23	0.043	-34	0.014	380	610	0.758	719	0.908
90	-20	0.044	-34	0.023	390	623	0.824	718	0.893
100	-17	0.035	-33	0.023	400	640	0.905	716	0.884
110	-15	0.054	-32	0.024	410	661	0.901	714	0.867
120	-11	0.055	-31	0.042	420	675	0.686	711	0.812
130	-7	0.083	-28	0.097	430	661	0.712	703	0.703
140	0	0.093	-19	0.162	440	656	0.590	686	0.520
150	8	0.122	-3	0.211	450	639	0.302	655	0.334
160	19	0.179	18	0.216	460	596	0.117	614	0.159
170	36	0.230	39	0.286	470	546	-0.026	566	0.036
180	58	0.264	67	0.394	480	493	-0.201	517	-0.026
190	83	0.363	106	0.465	490	432	-0.308	472	-0.047
200	118	0.442	151	0.559	500	370	0.322	433	0.411
210	160	0.490	204	0.646					
220	205	0.436	263	0.681					
230	241	0.486	321	0.743					
240	280	0.553	380	0.820					
250	323	0.649	440	0.827					
260	372	0.749	492	0.926					
270	426	0.765	545	0.960					
280	474	0.788	590	1.001					
290	516	0.755	629	1.061					

[b]Smoothed experimental temperatures are presented in these tables

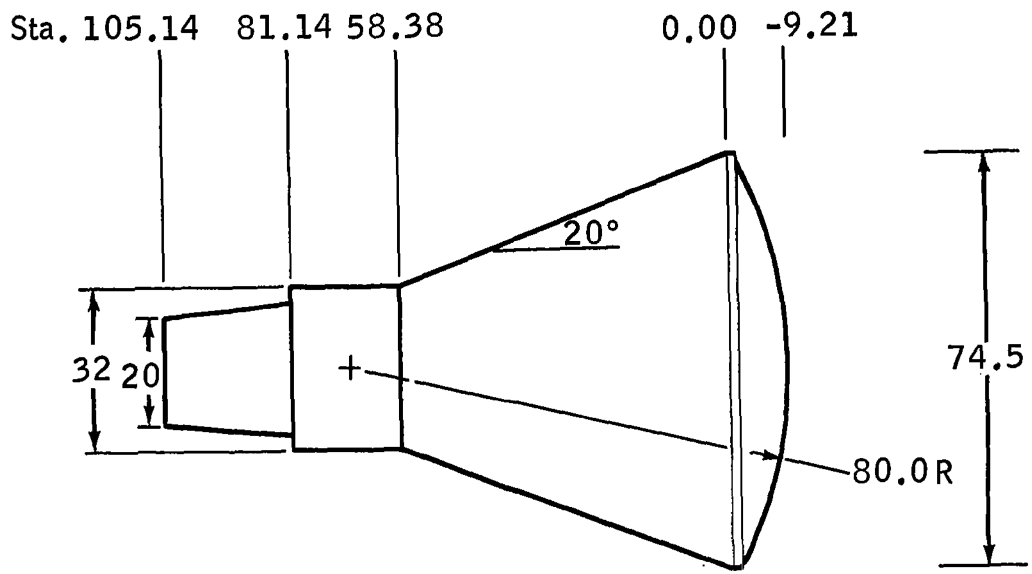

Figure 1. - Mercury spacecraft reentry configuration.

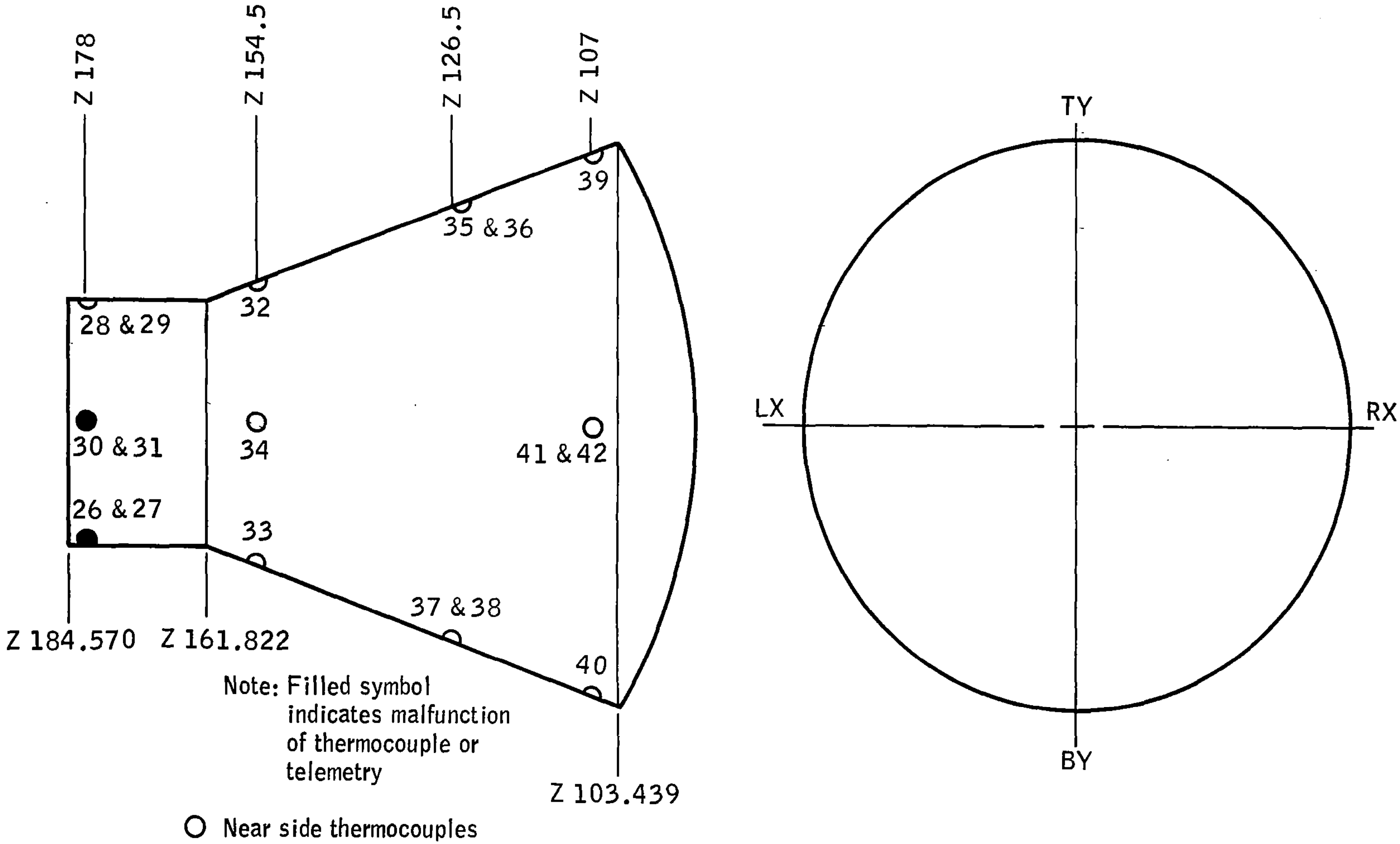

Figure 2a. - Instrumentation locations on afterbody of MA-2.

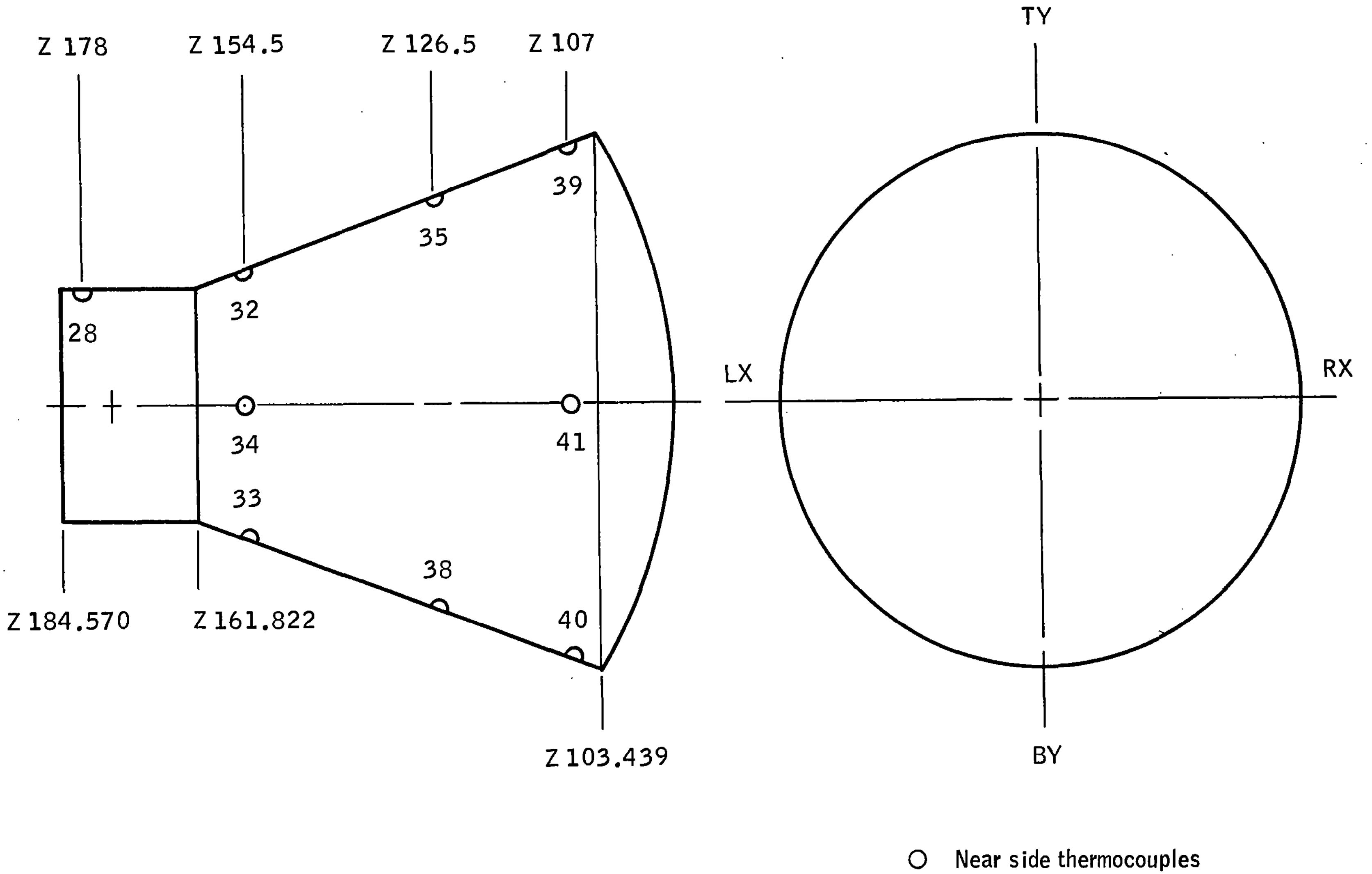

Figure 2b. - Instrumentation locations on afterbody of MA-5.

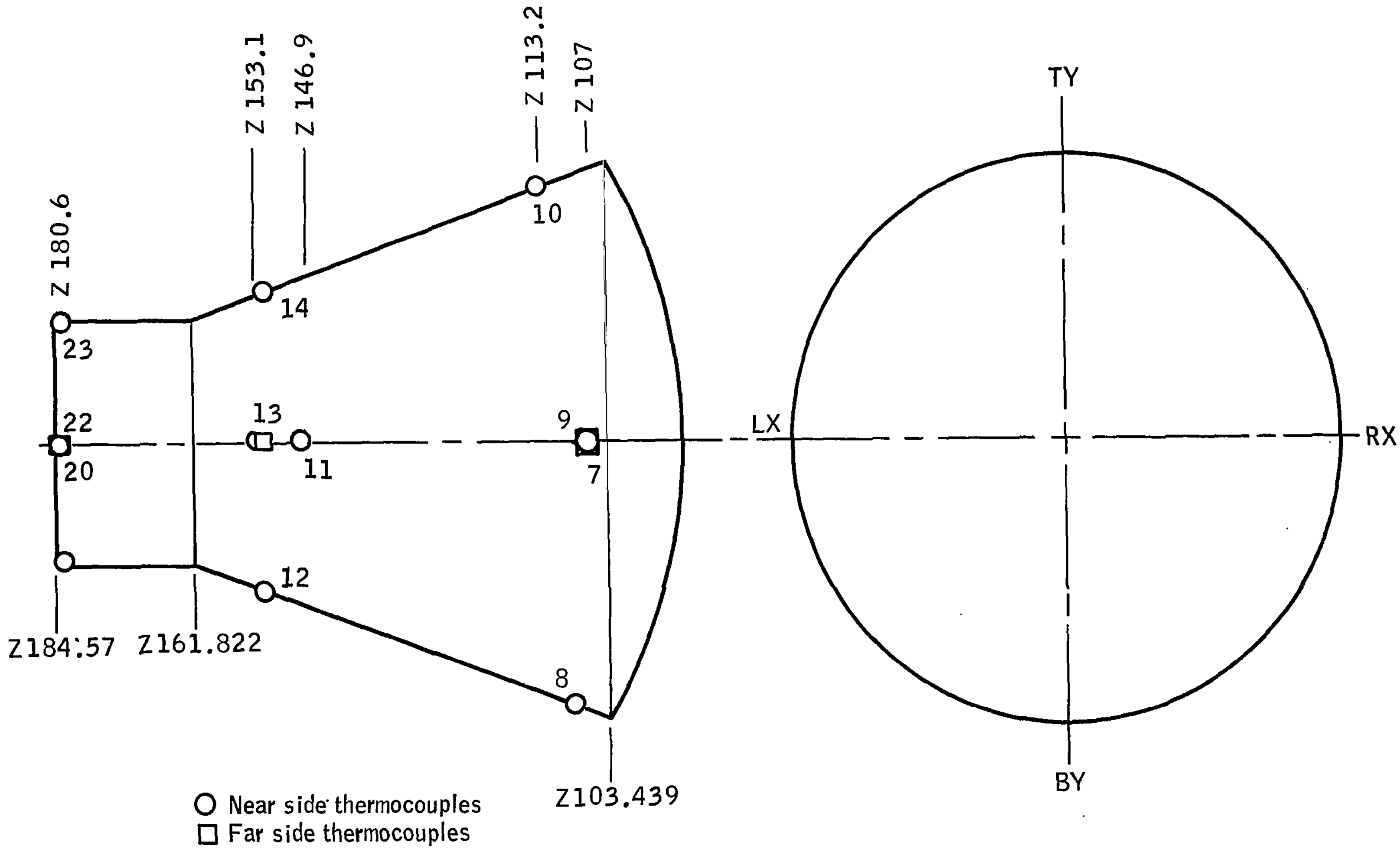

Figure 2c. - Instrumentation locations on afterbody of MA-7.

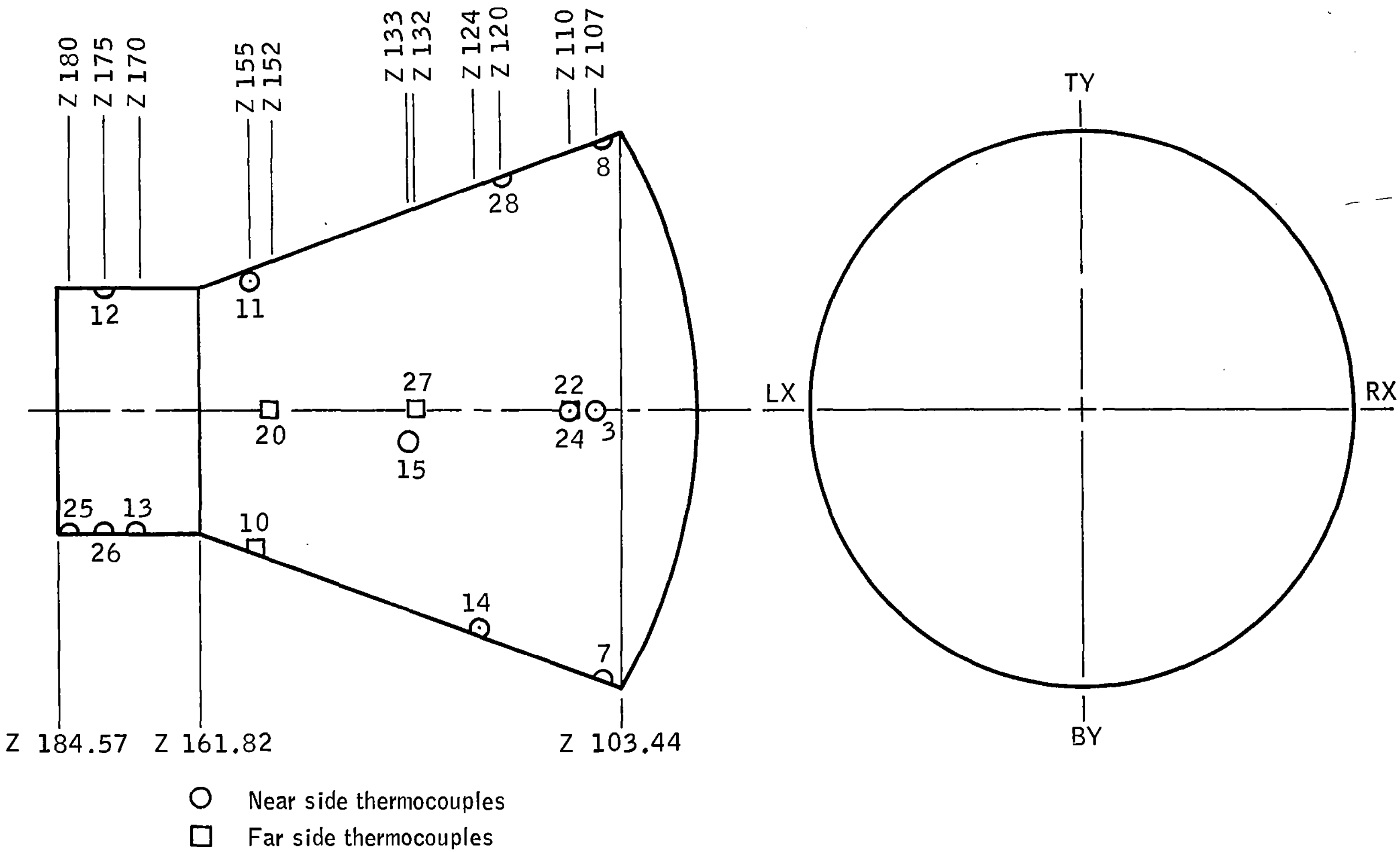

Figure 2d. - Instrumentation locations on afterbody of MA-8.

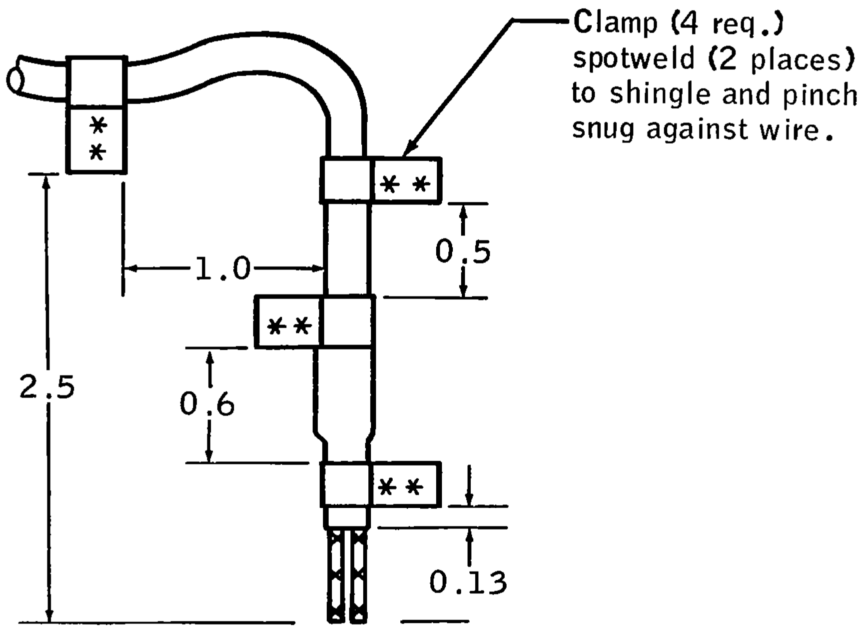

Figure 3. - Thermocouple installation - tiedown, typical.

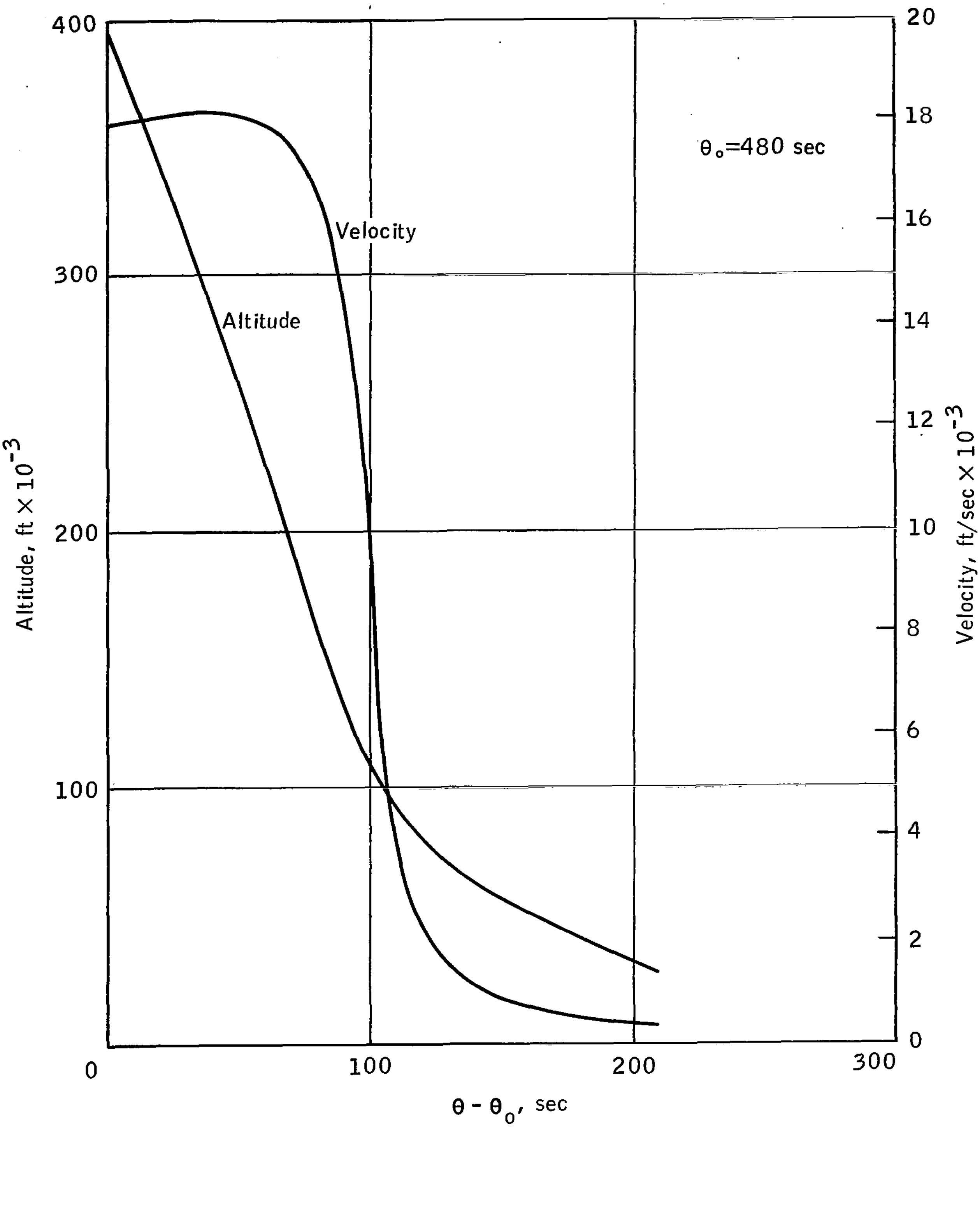

Figure 4a. - Trajectory parameters abort trajectory flight MA-2.

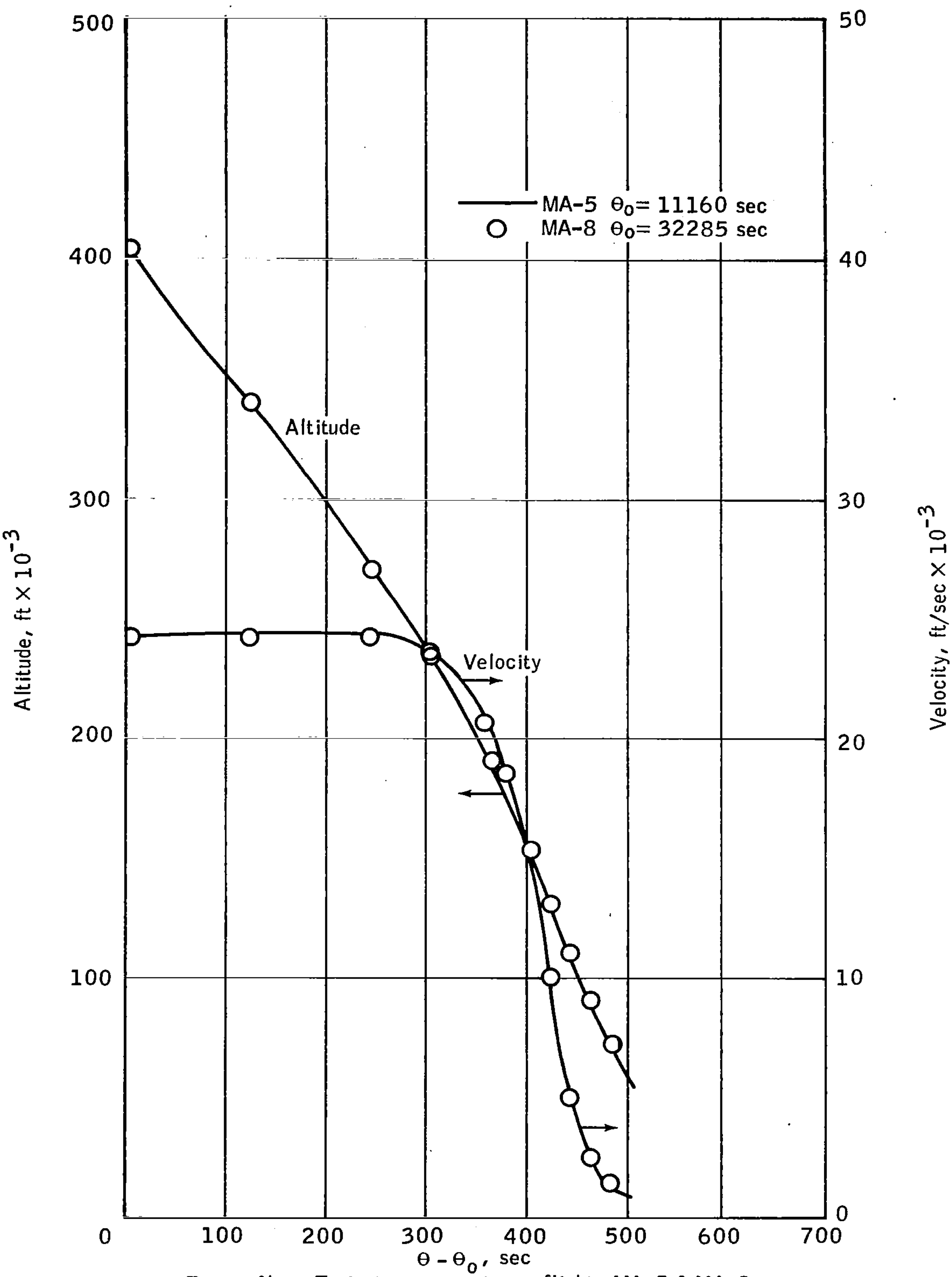

Figure 4b. - Trajectory parameters - flights MA-5 & MA-8.

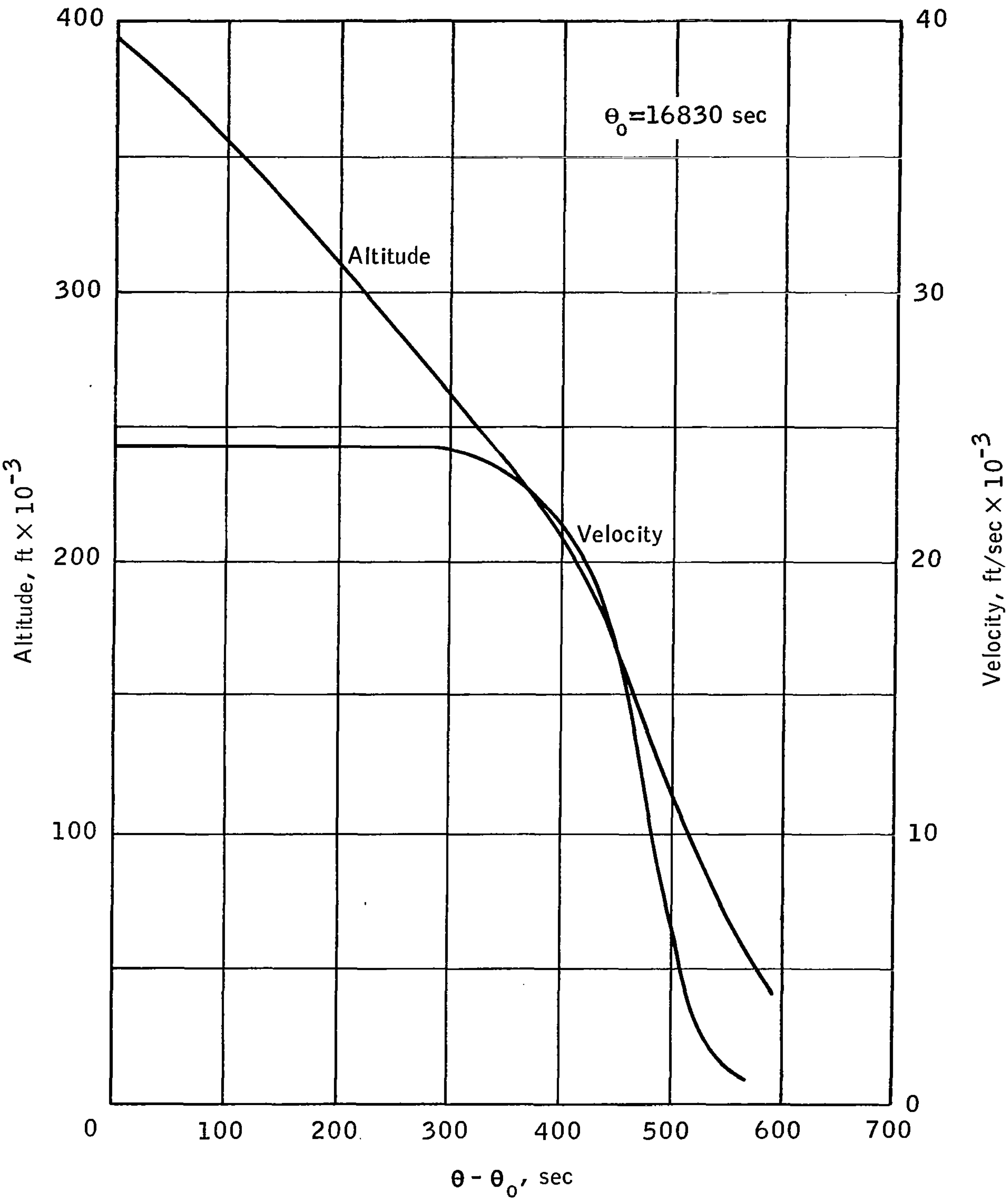

Figure 4c. - Trajectory parameters flight MA-7.

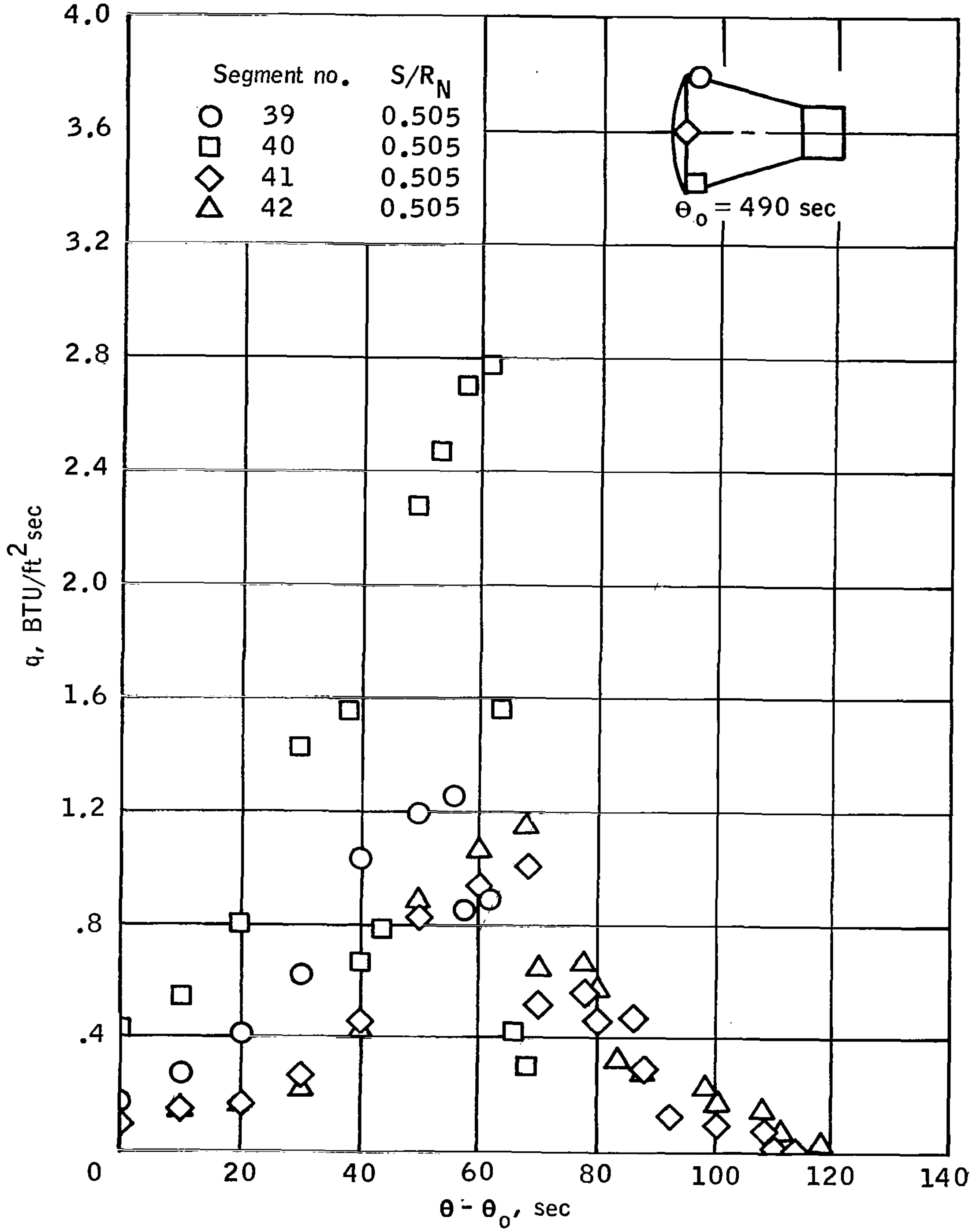

Figure 5a. - Experimental convective heating rate-mission MA-2.

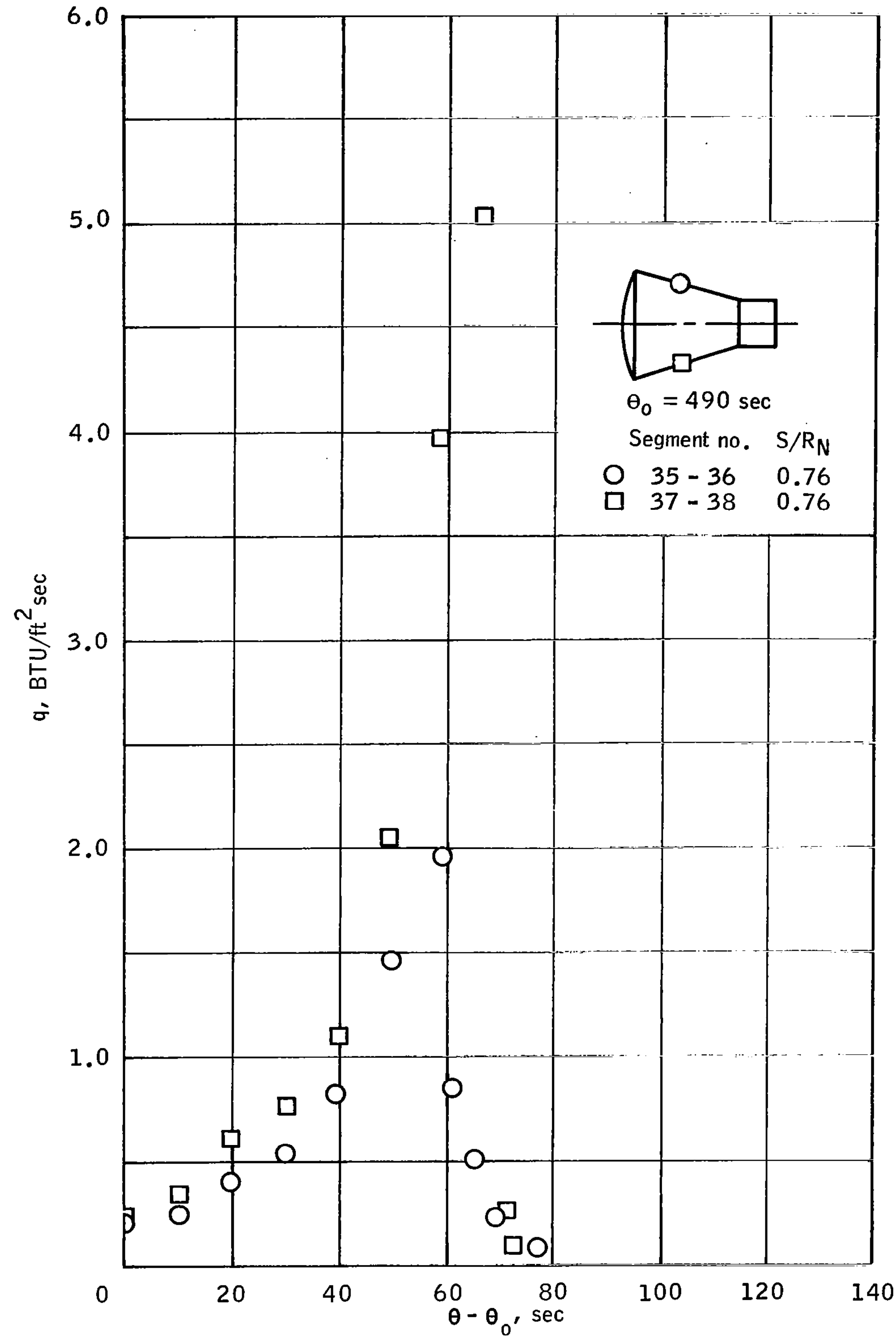

Figure 5b. - Experimental convective heating rate - mission MA-2.

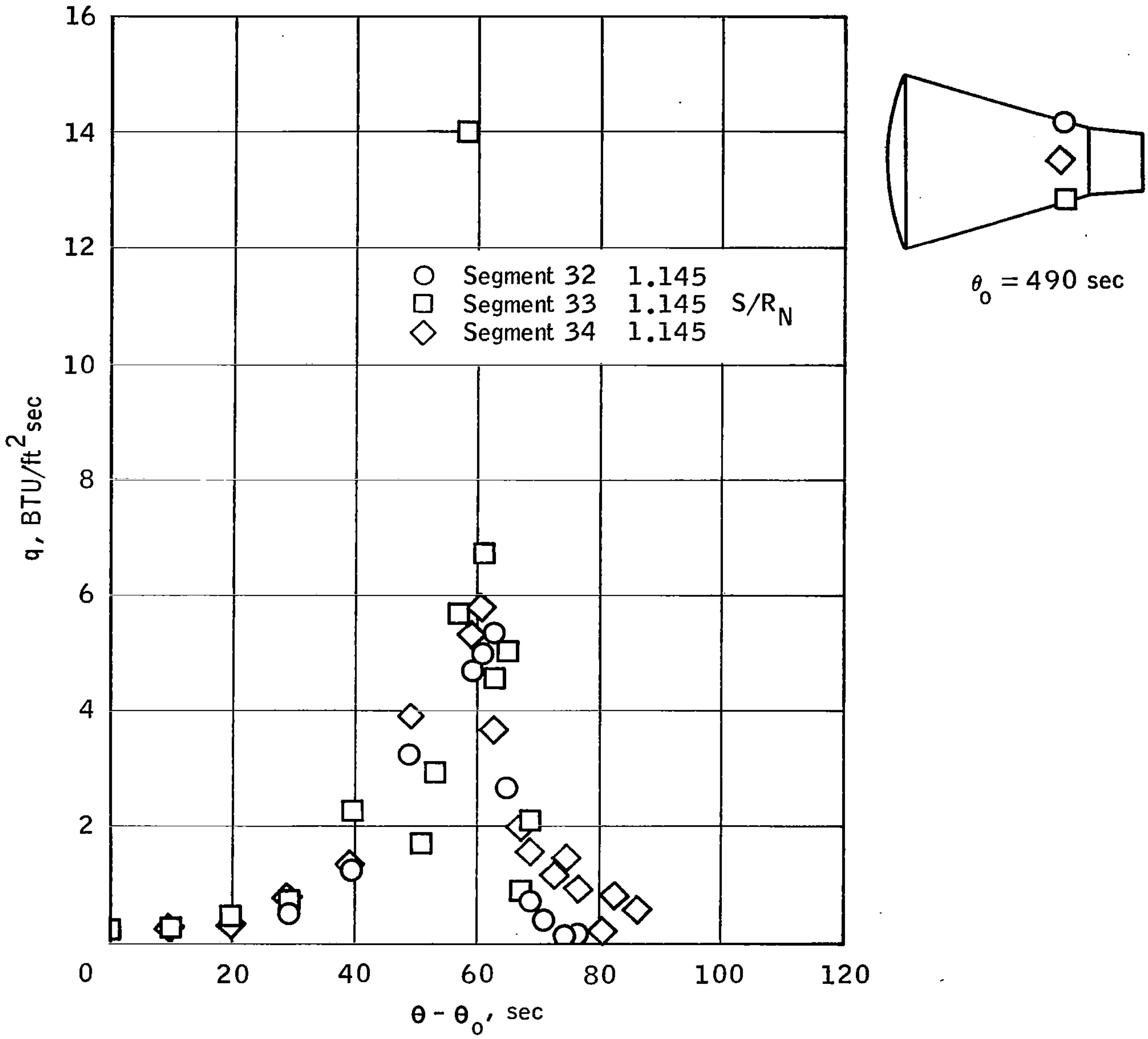

Figure 5c. - Experimental convective heating rate - mission MA-2.

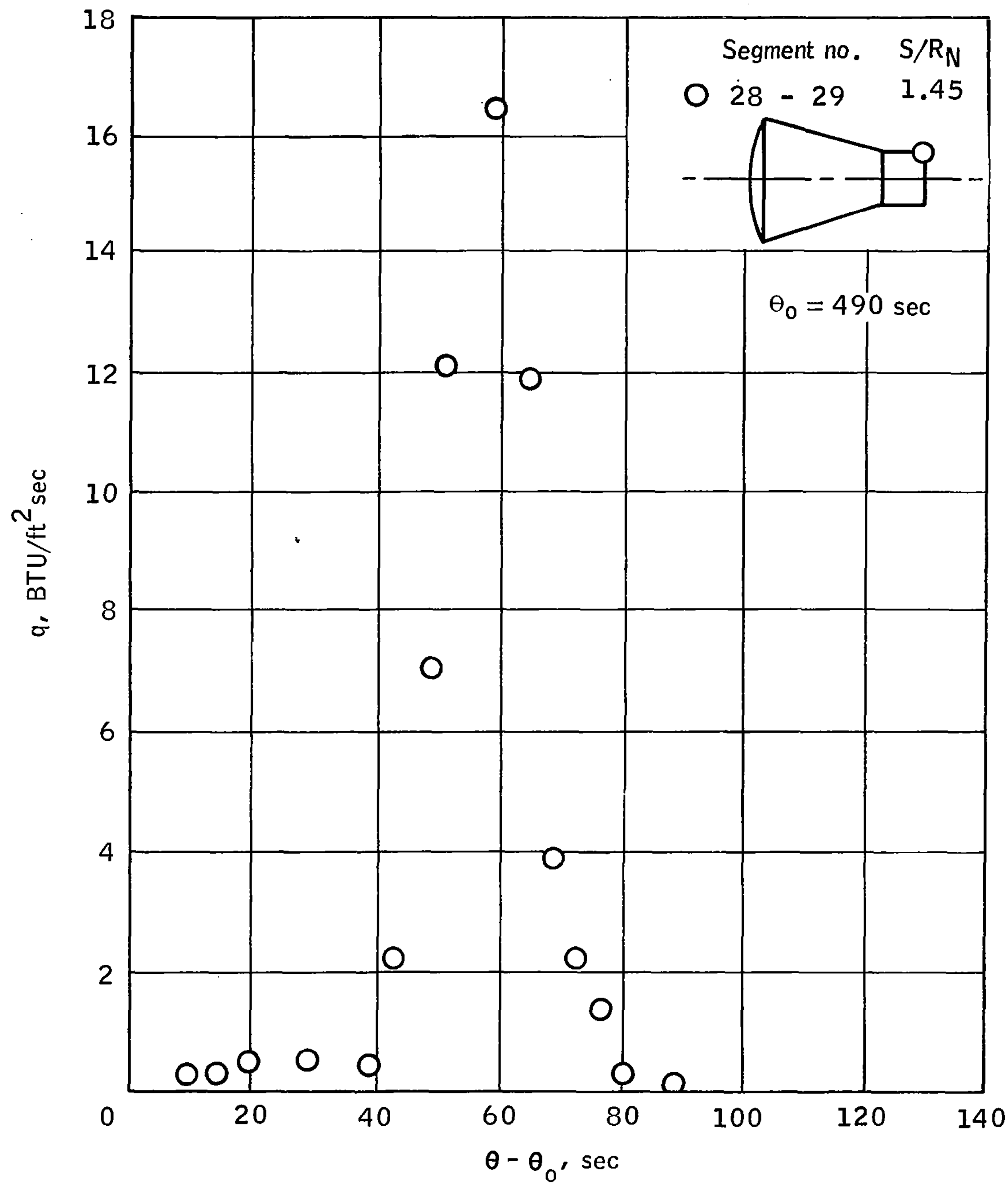

Figure 5d. - Experimental convective heating rate-mission MA-2.

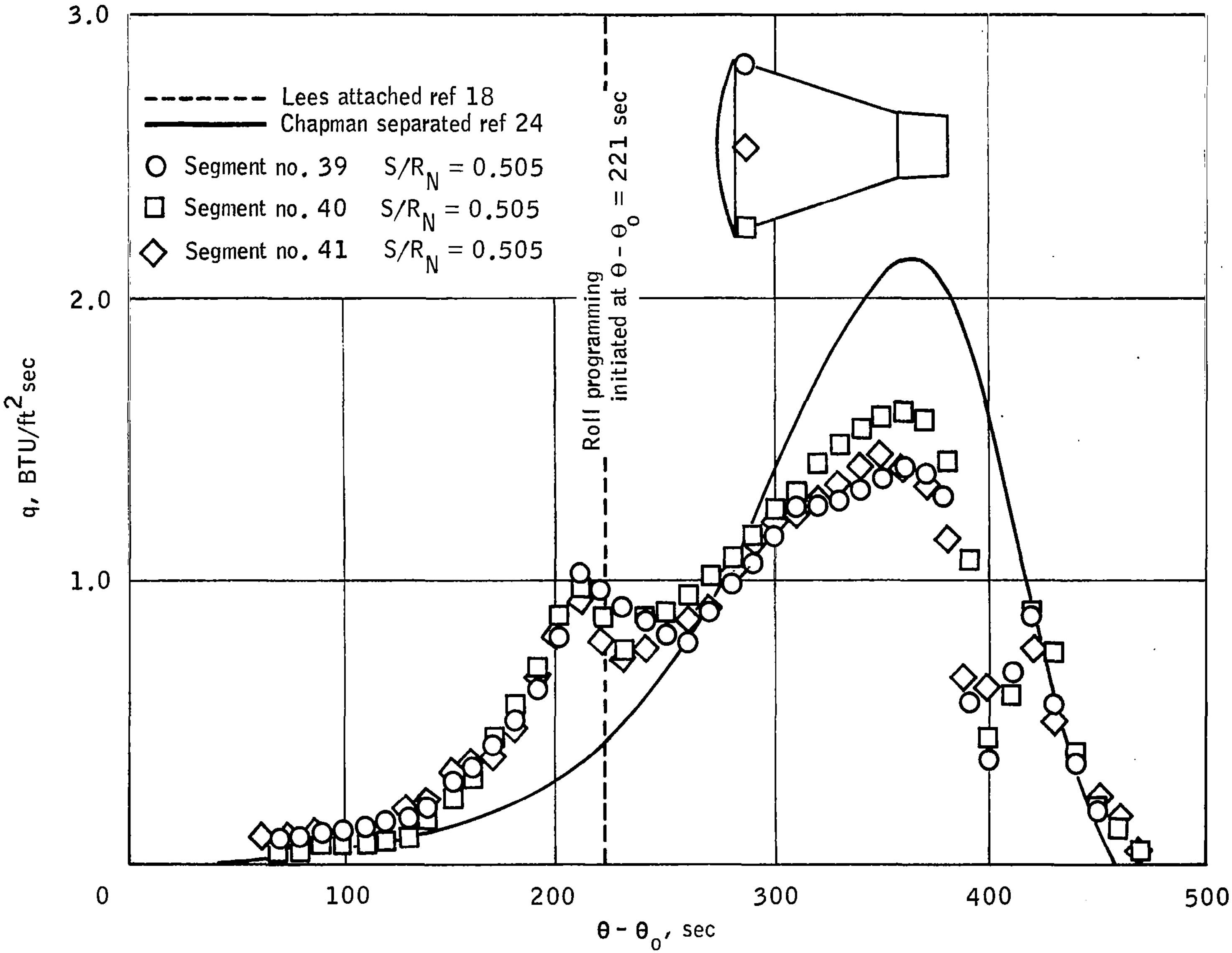

Figure 6a. - Experimental convective heating rate - mission MA-5.

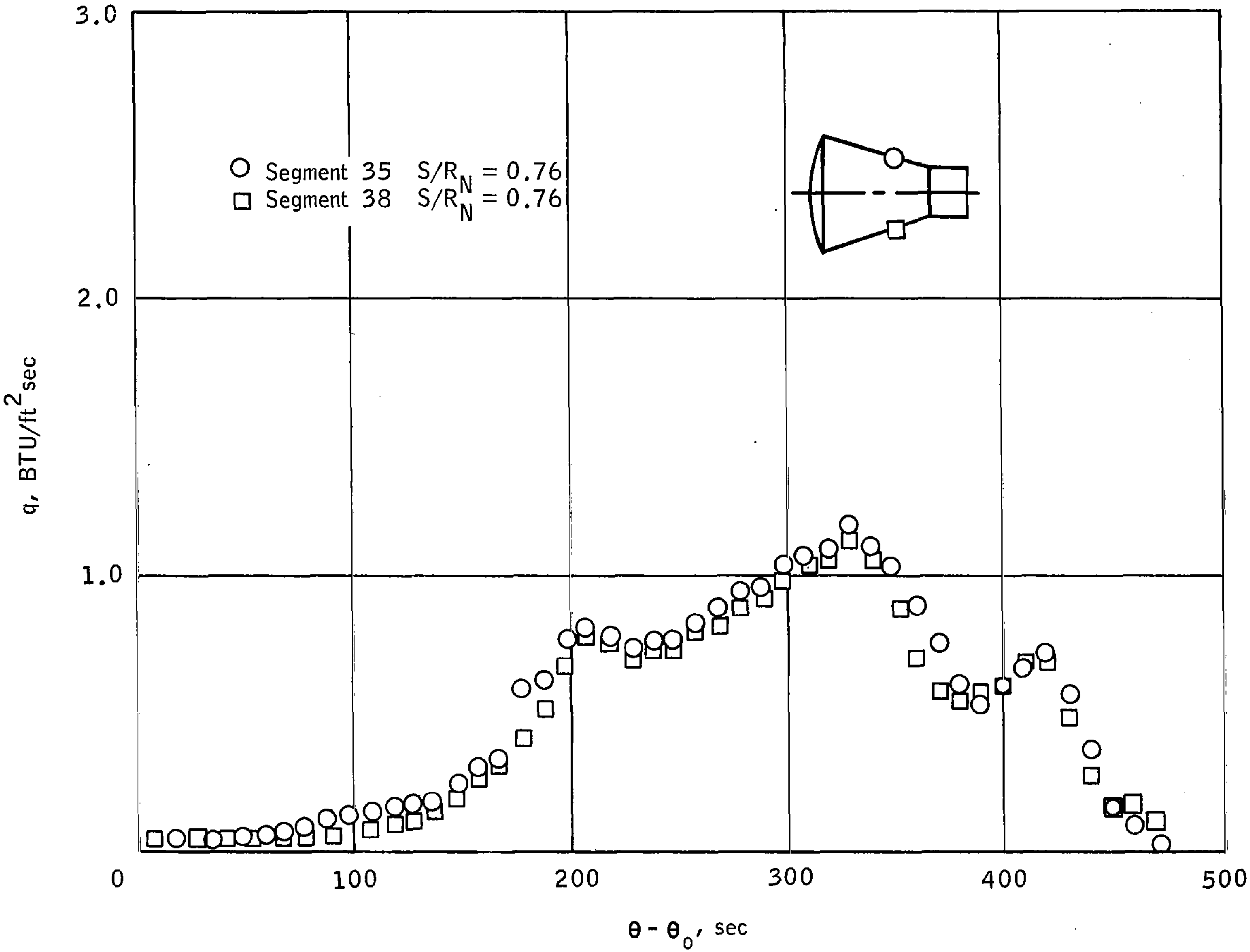

Figure 6b. - Experimental convective heating rate - mission MA-5.

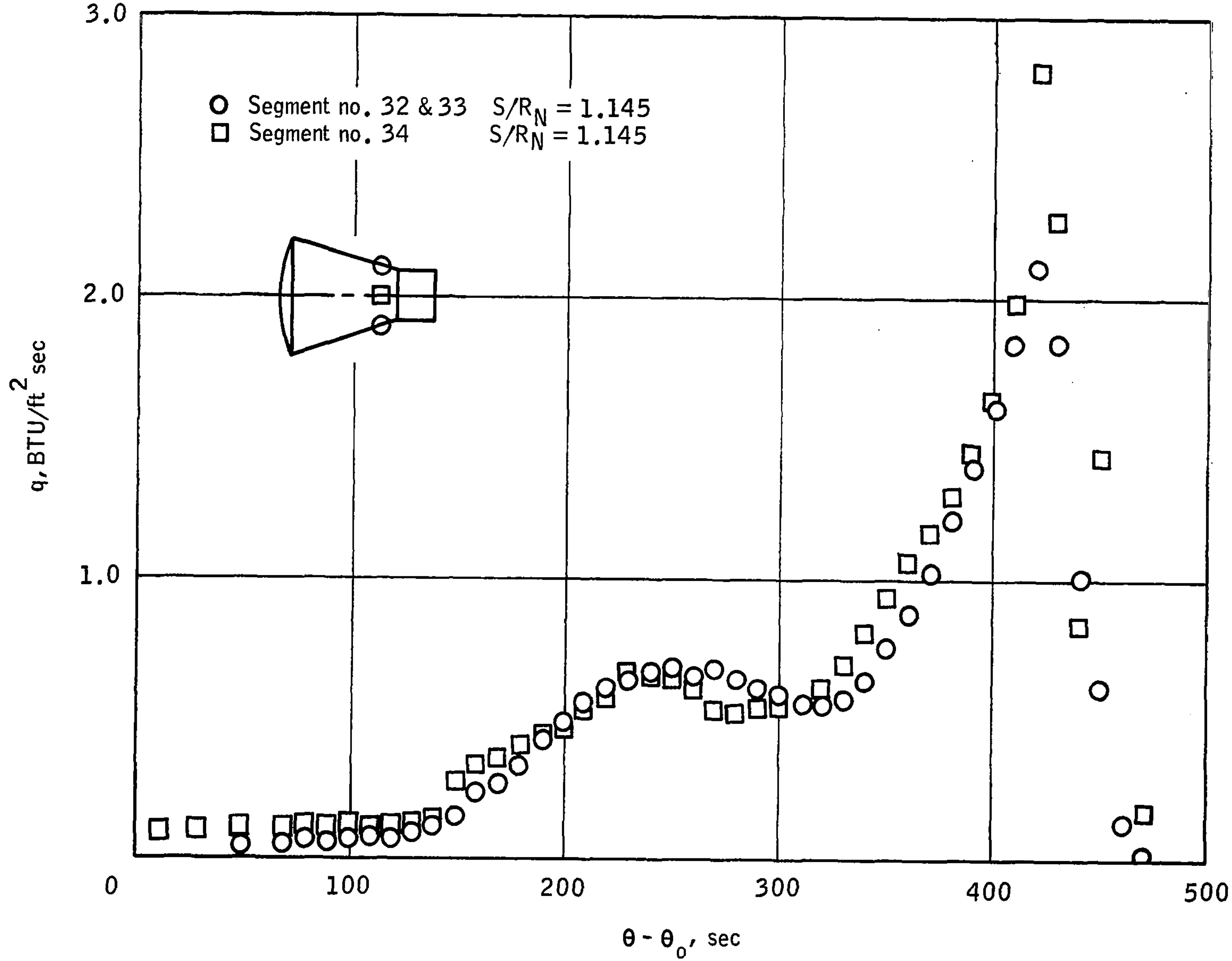

Figure 6c.- Experimental convective heating rate - mission MA-5.

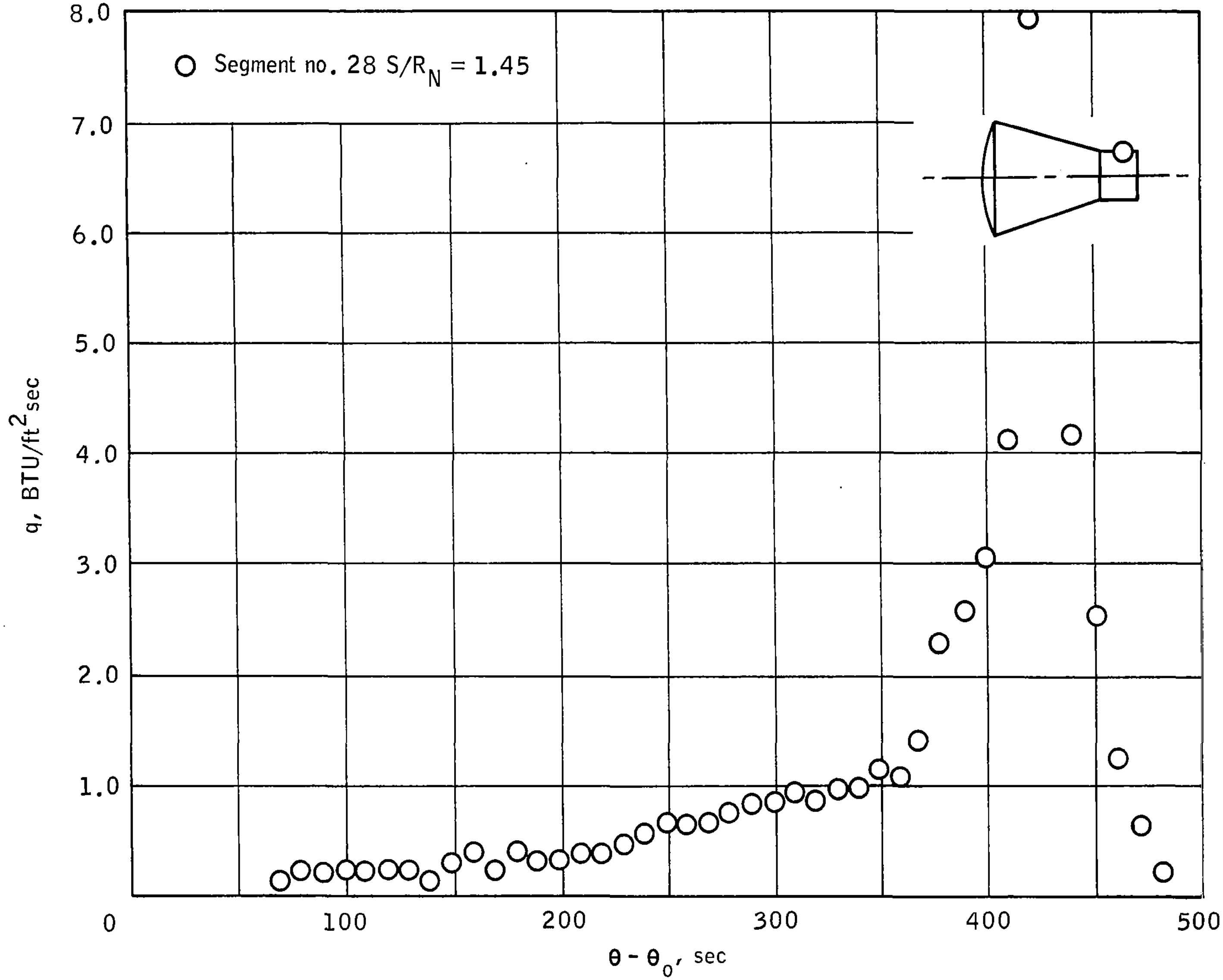

Figure 6d. - Experimental convective heating rate - mission MA-5.

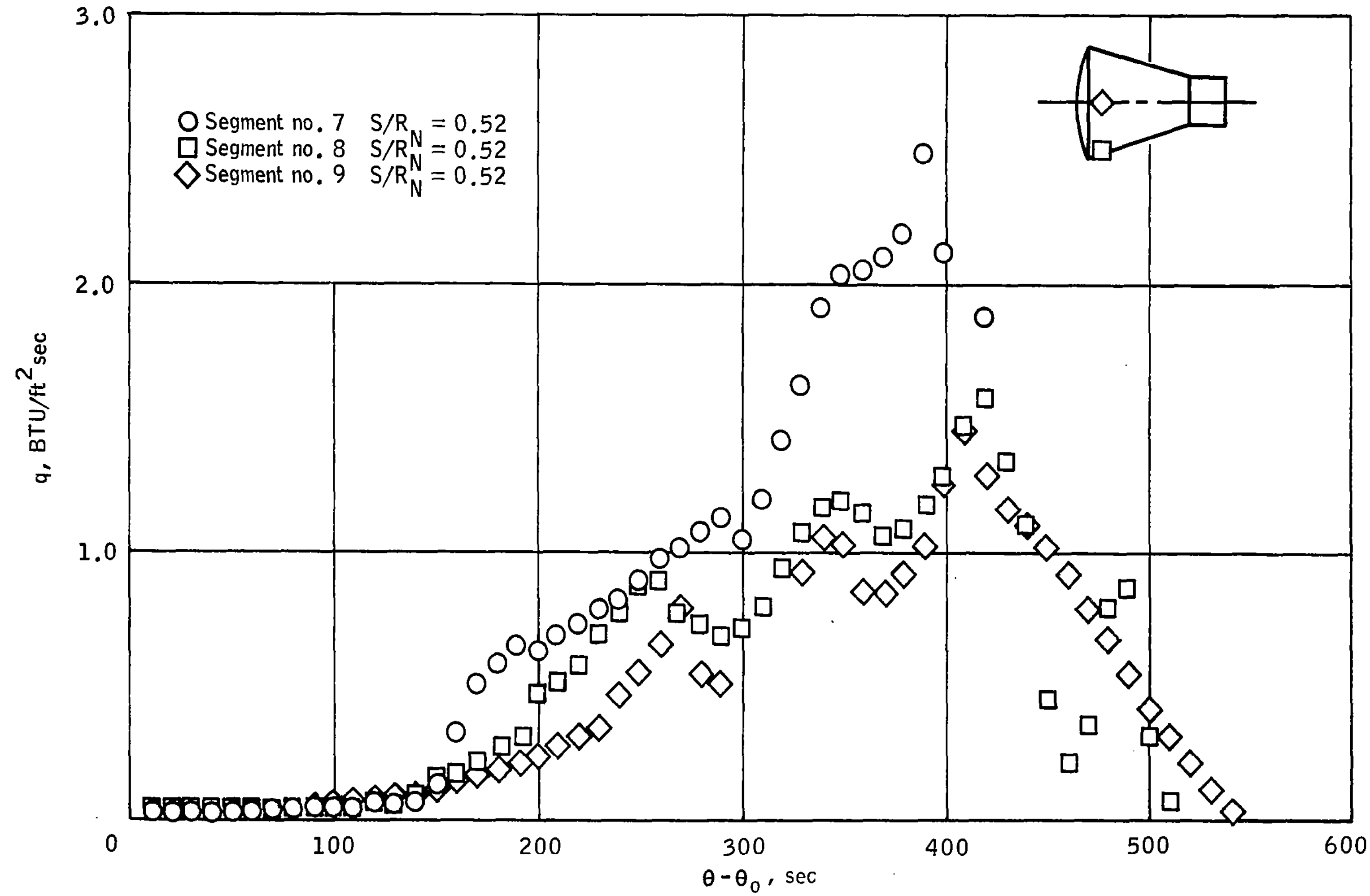

Figure 7a. - Experimental convective heating rate - mission MA-7.

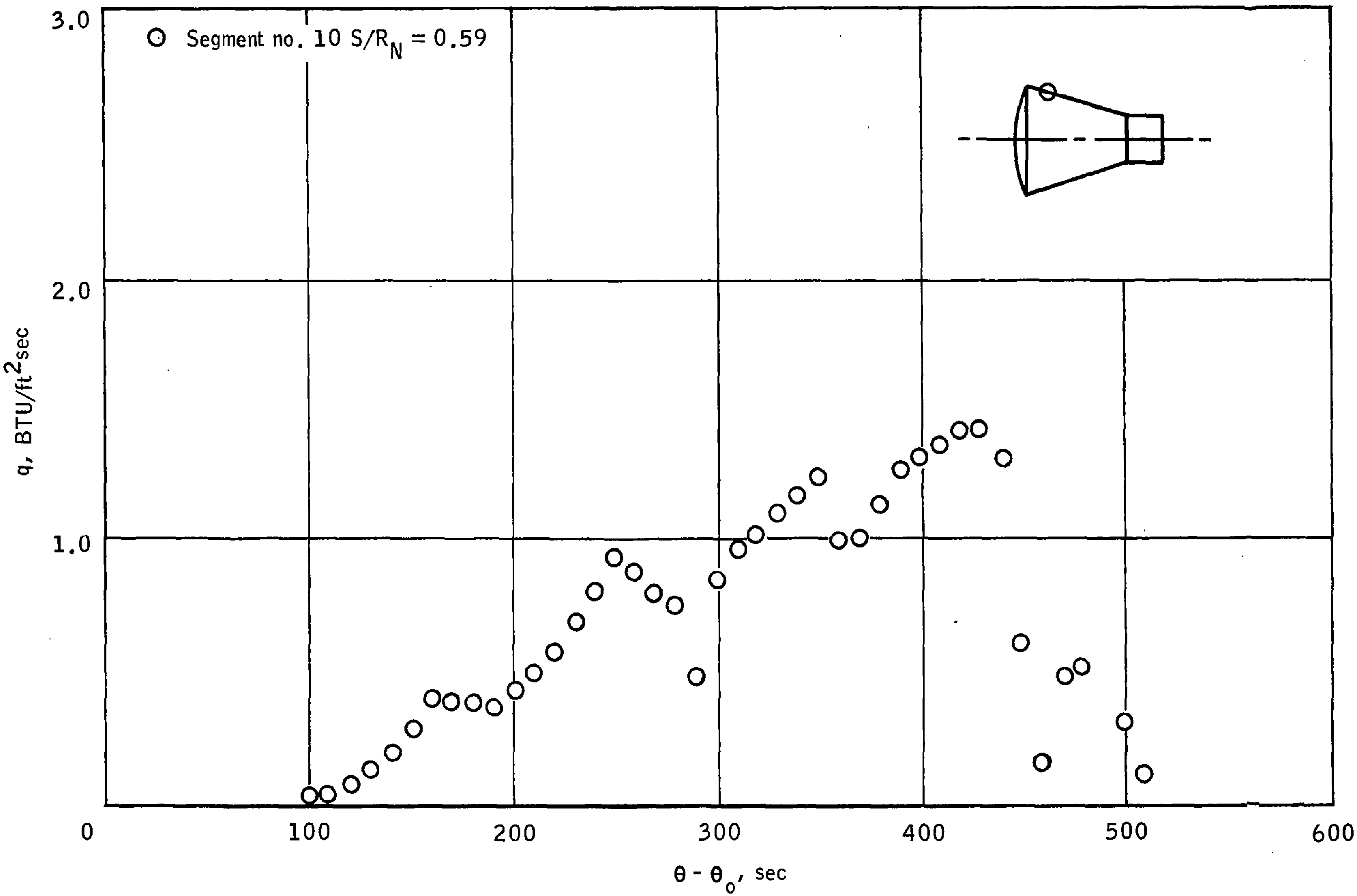

Figure 7b. - Experimental convective heating rate - mission MA-7.

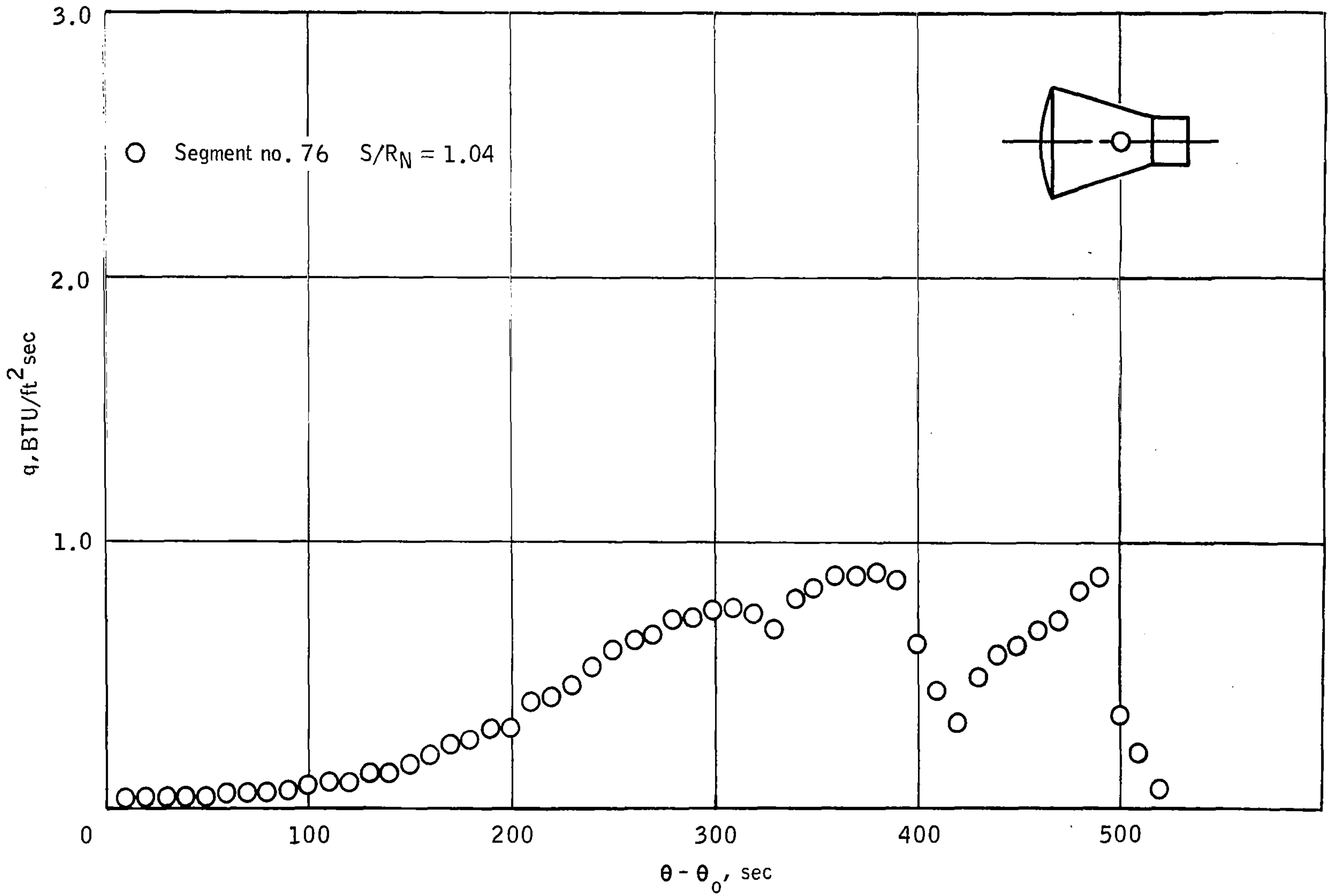

Figure 7c. - Experimental convective heating rate-mission MA-7.

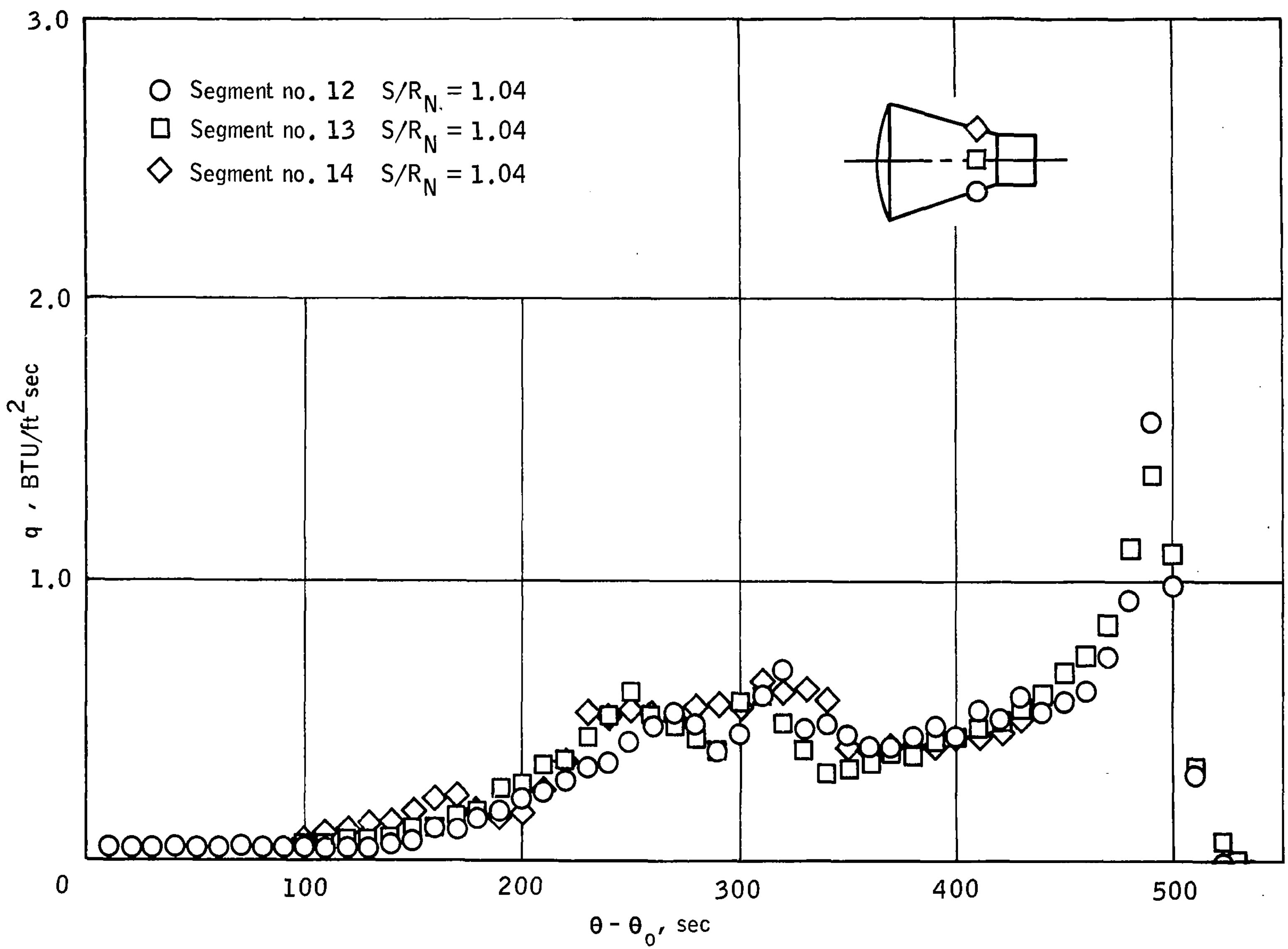

Figure 7d. - Experimental convective heating rate - mission MA-7.

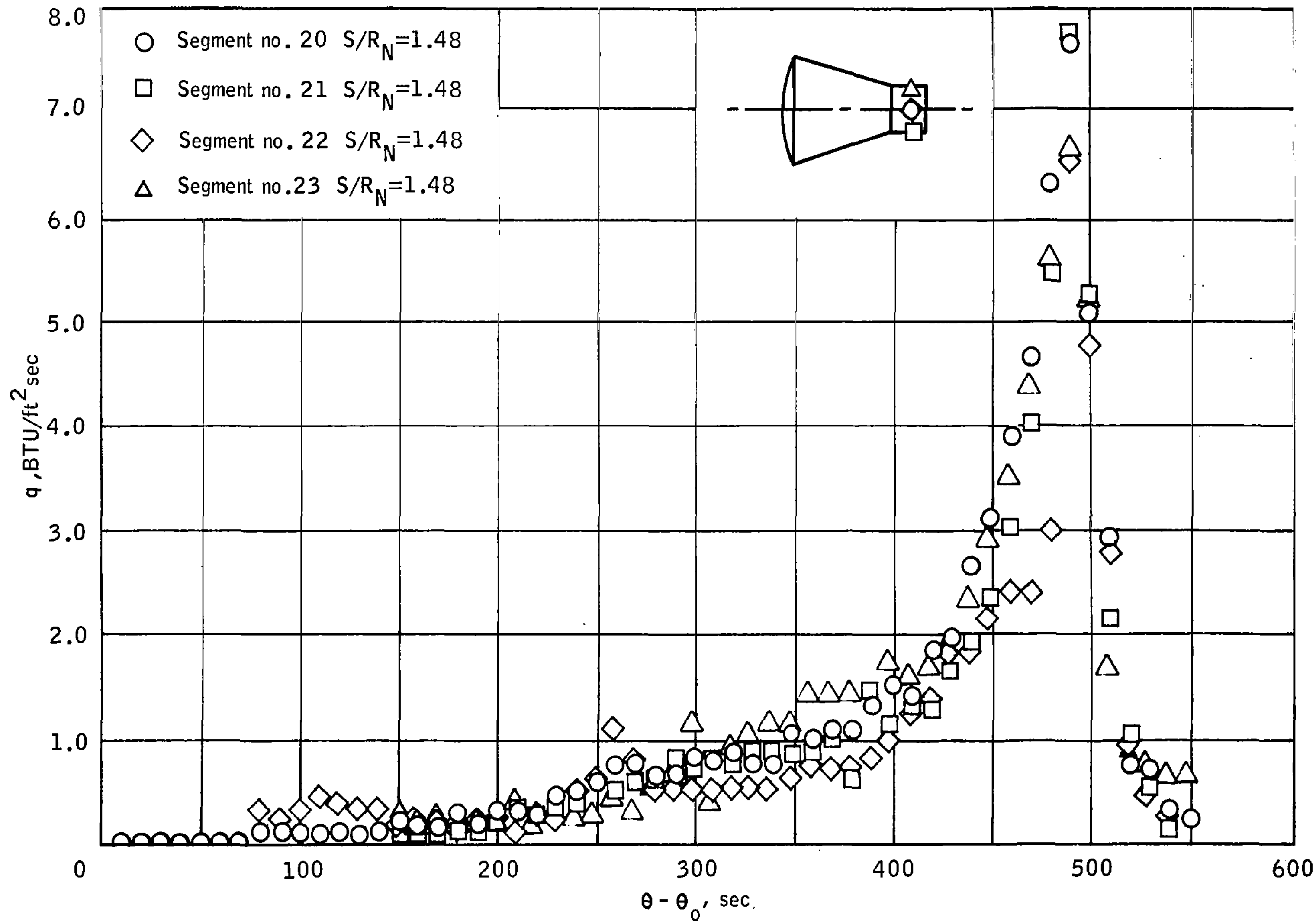

Figure 7e.- Experimental convective heating rate- mission MA-7

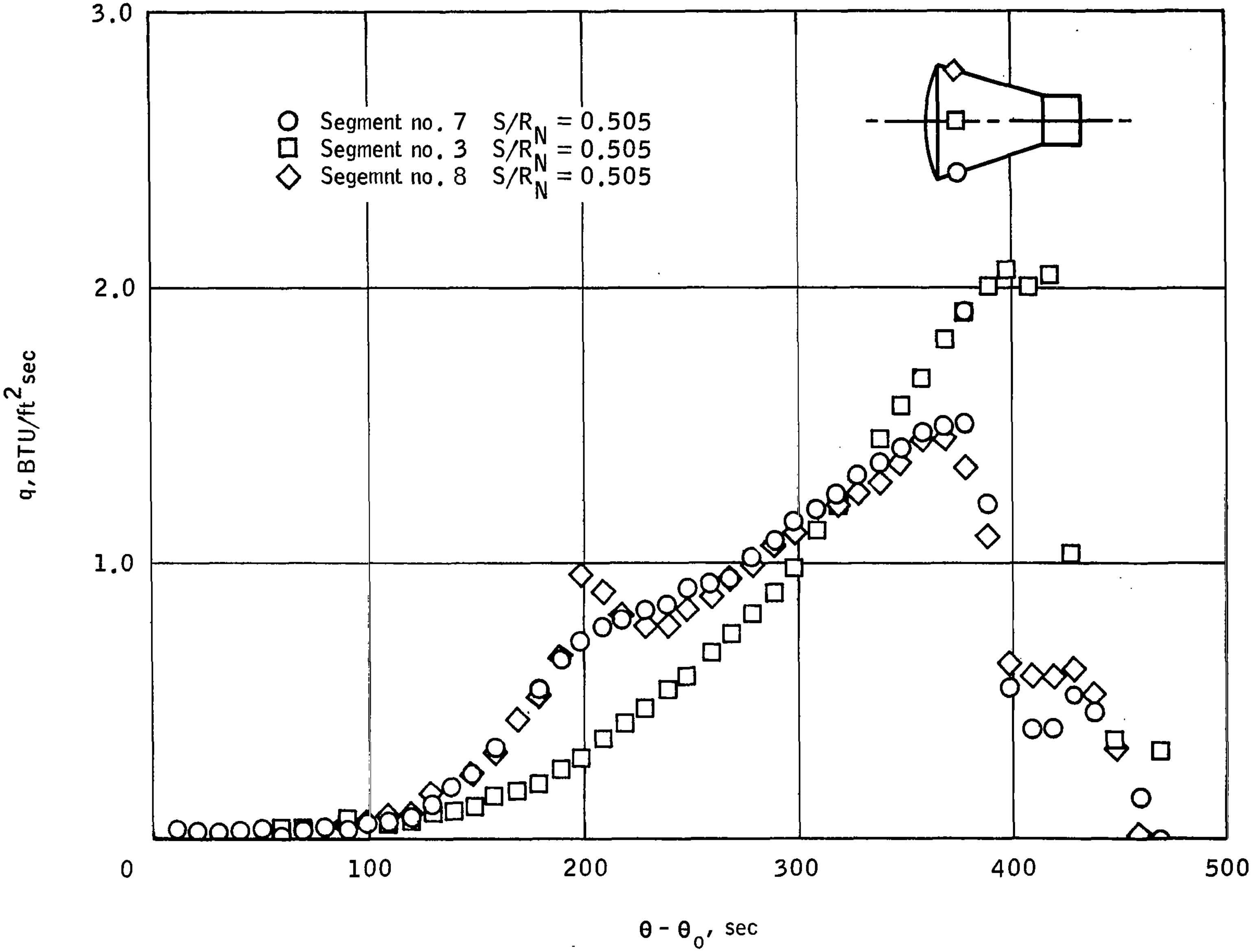

Figure 8a. - Experimental convective heating rate - mission MA-8.

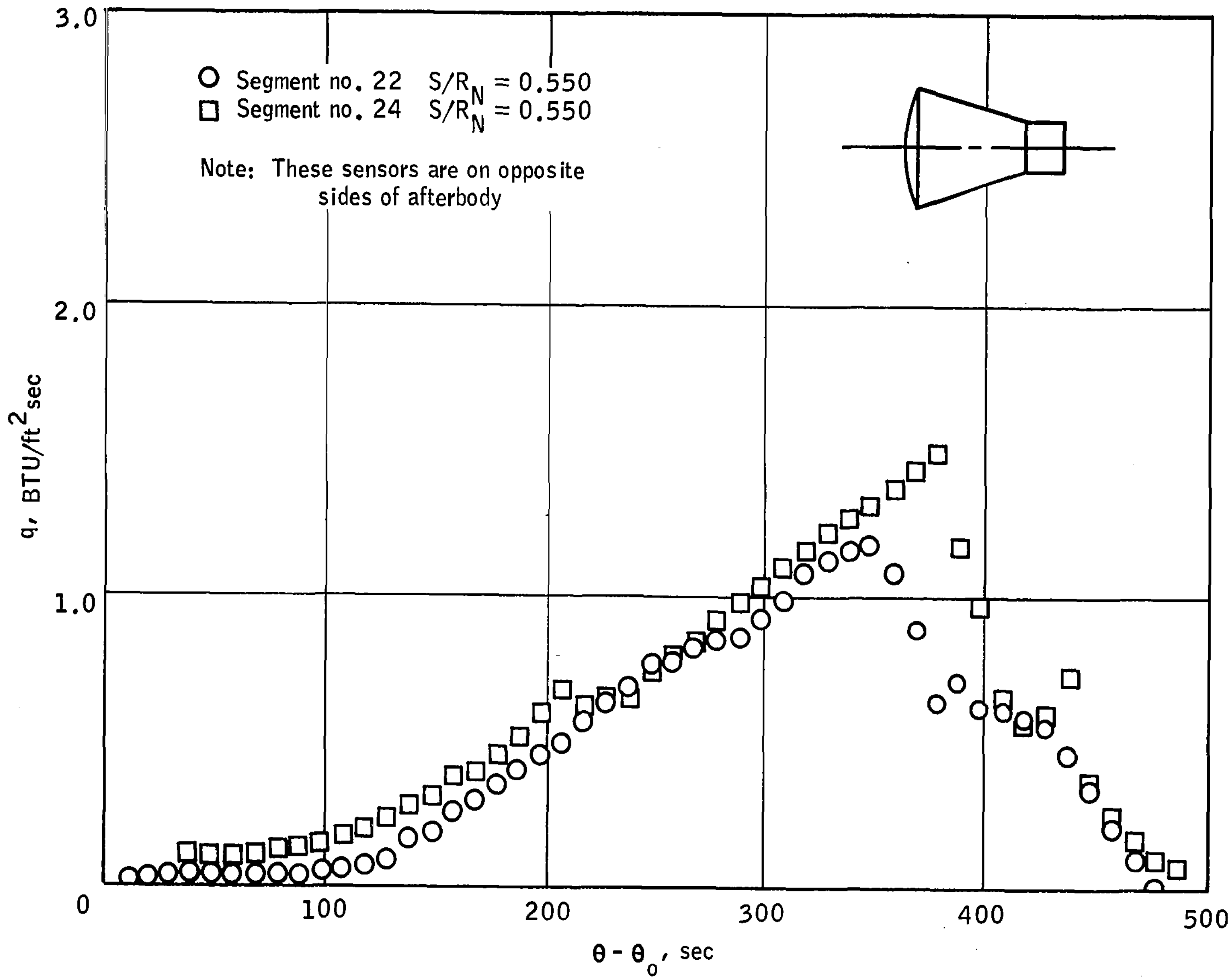

Figure 8b. - Experimental convective heating rate - mission MA-8

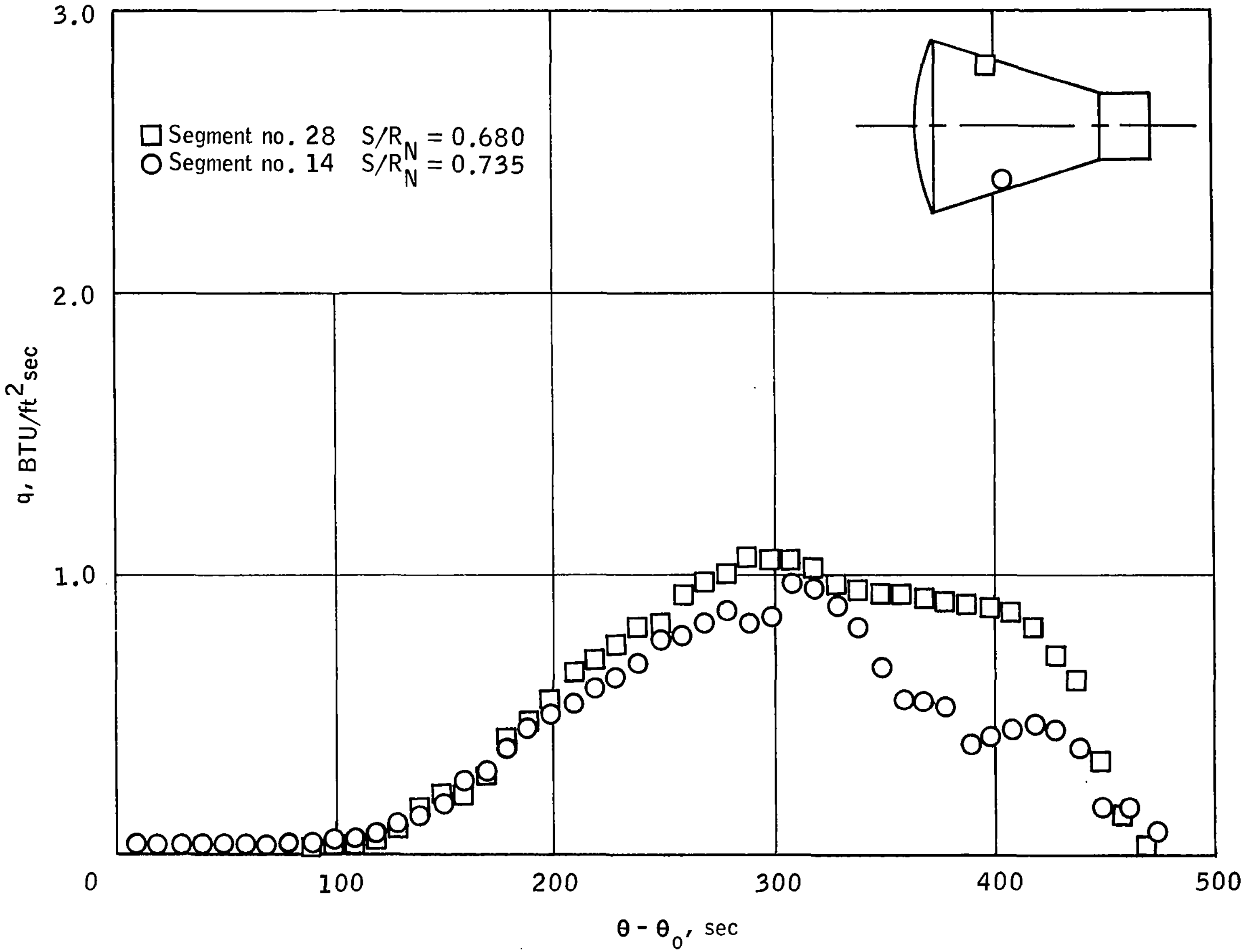

Figure 8c. - Experimental convective heating rate - mission MA-8.

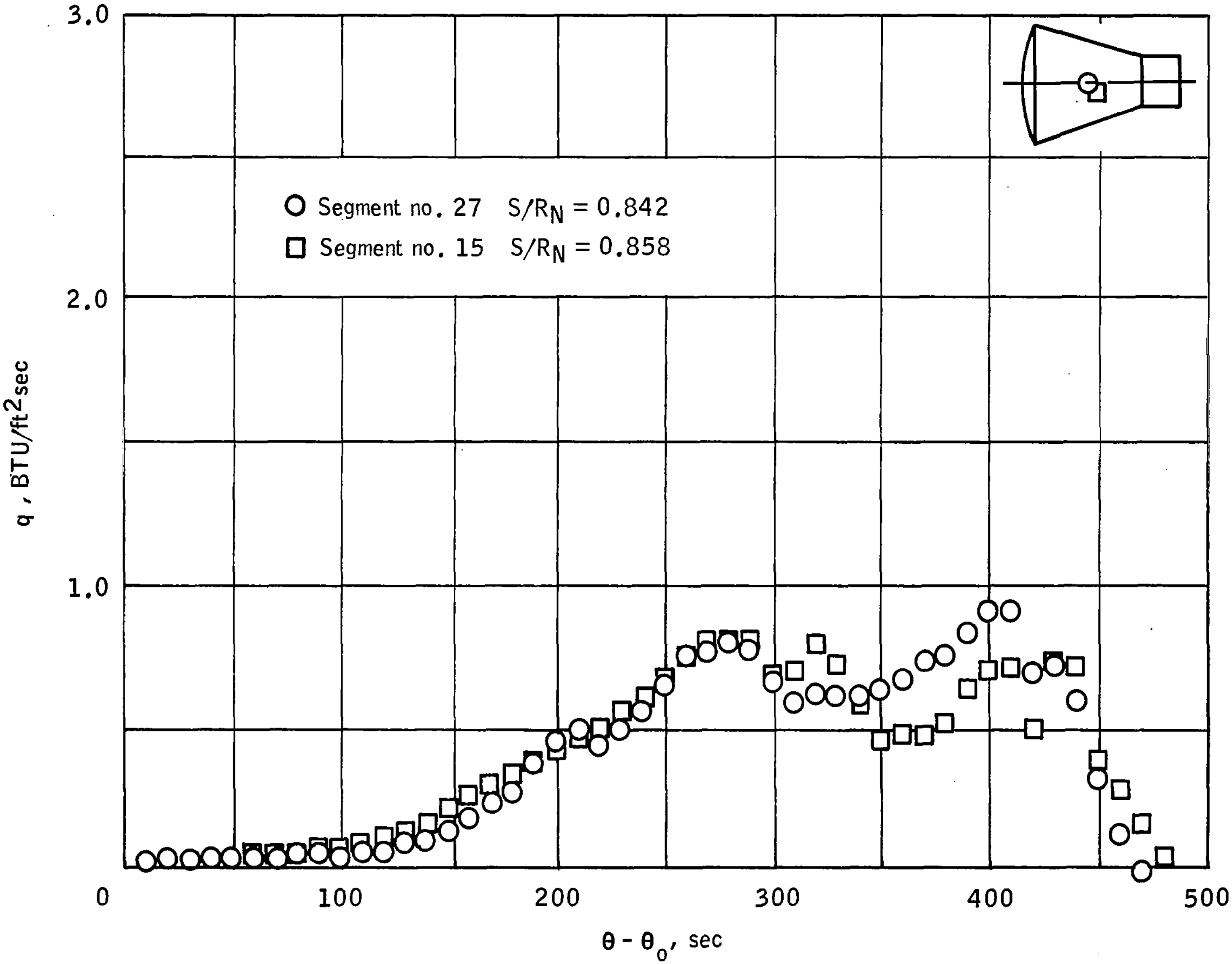

Figure 8d. - Experimental convective heating rate - mission MA-8.

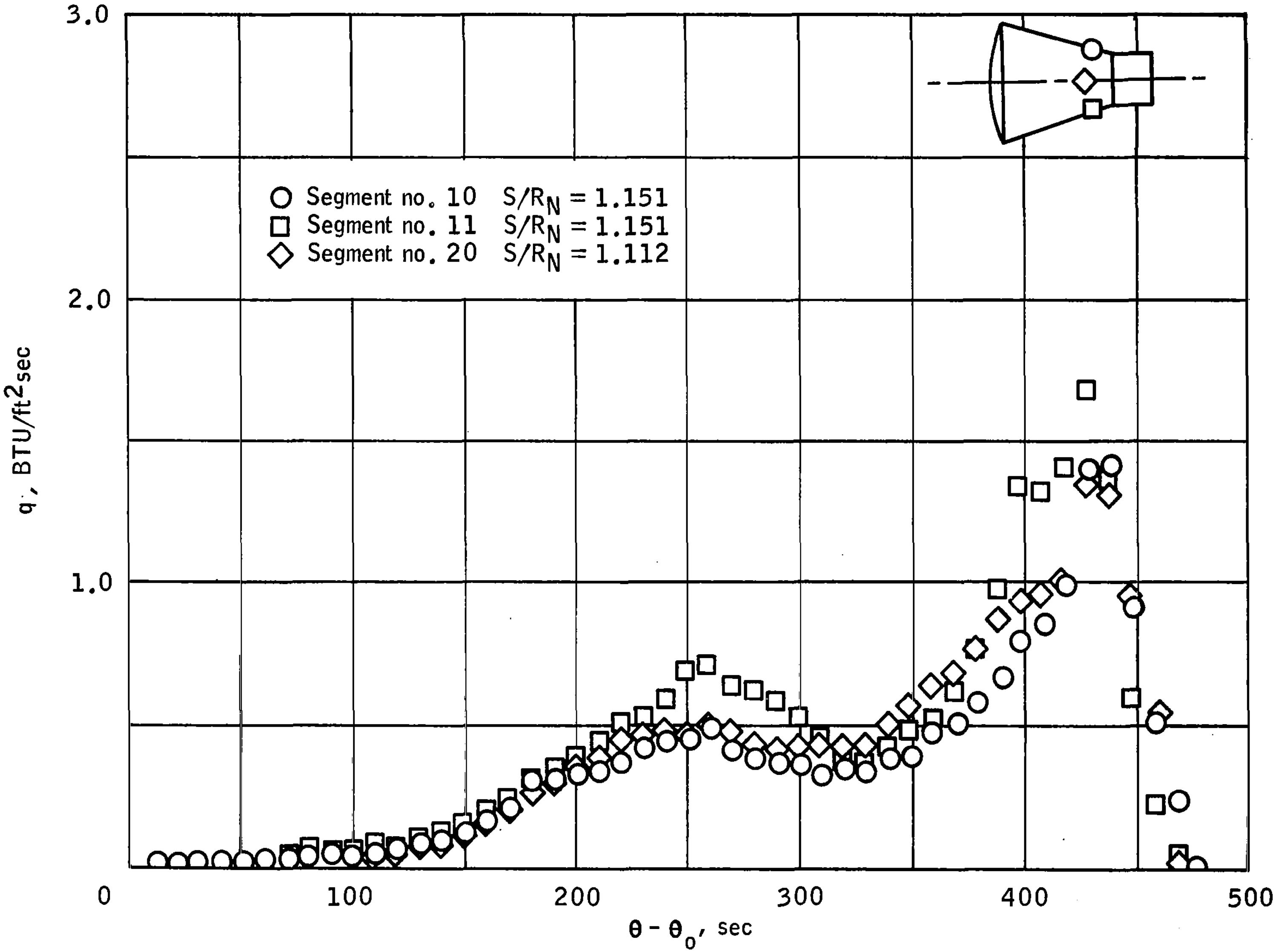

Figure 8e. - Experimental convective heating rate - mission MA-8.

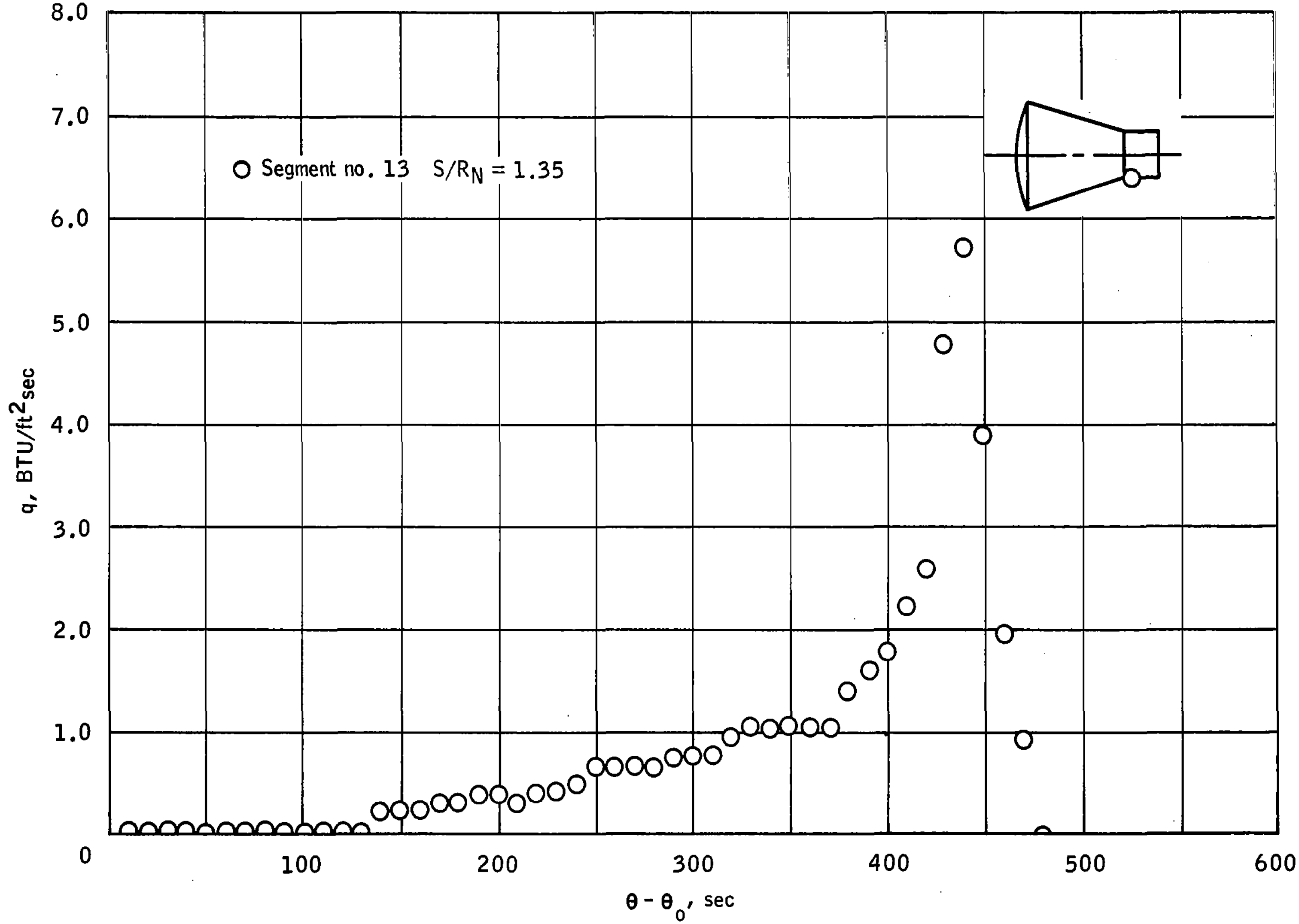

Figure 8f. - Experimental convective heating rate - mission MA-8.

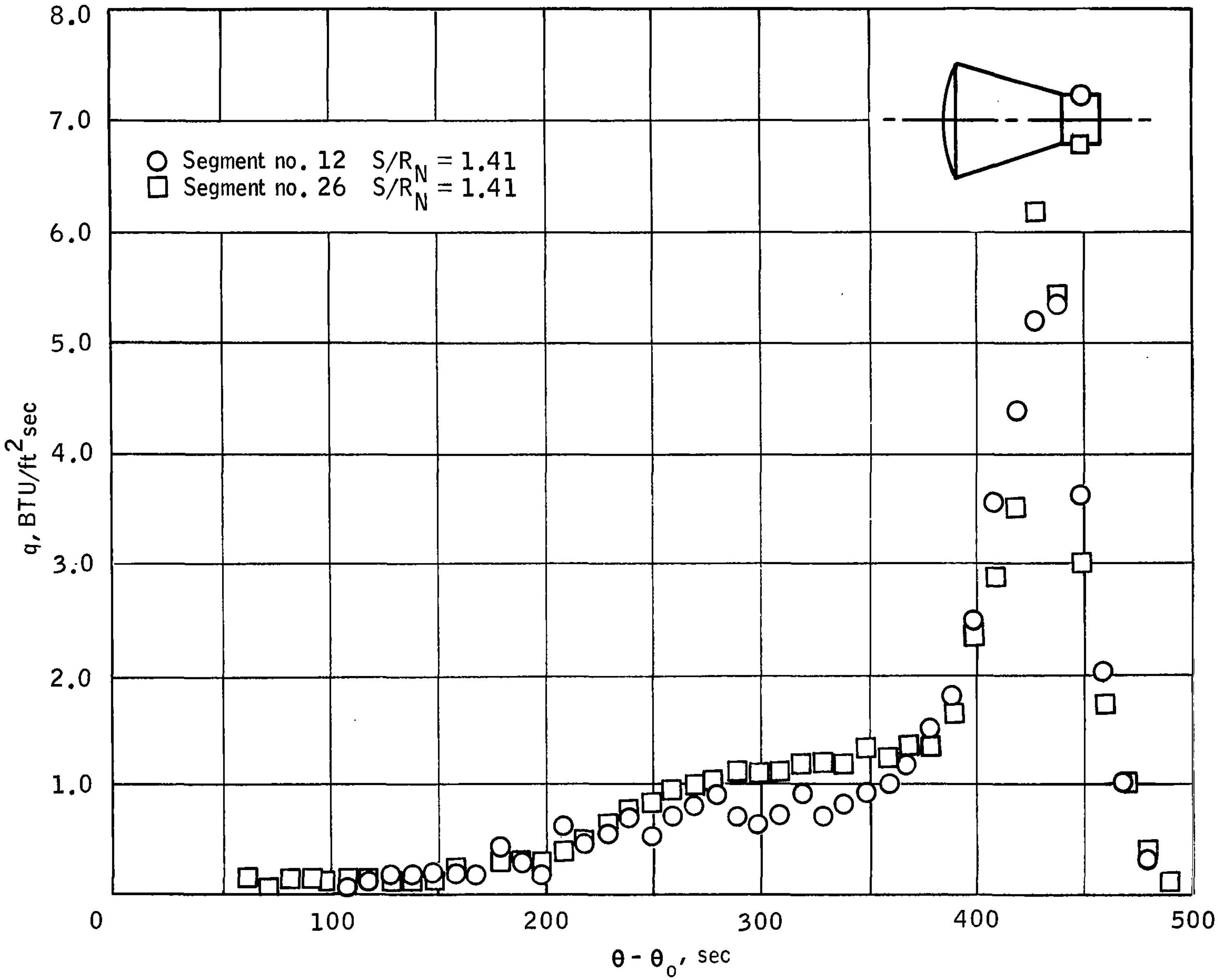

Figure 8g. - Experimental convective heating rate - mission MA-8.

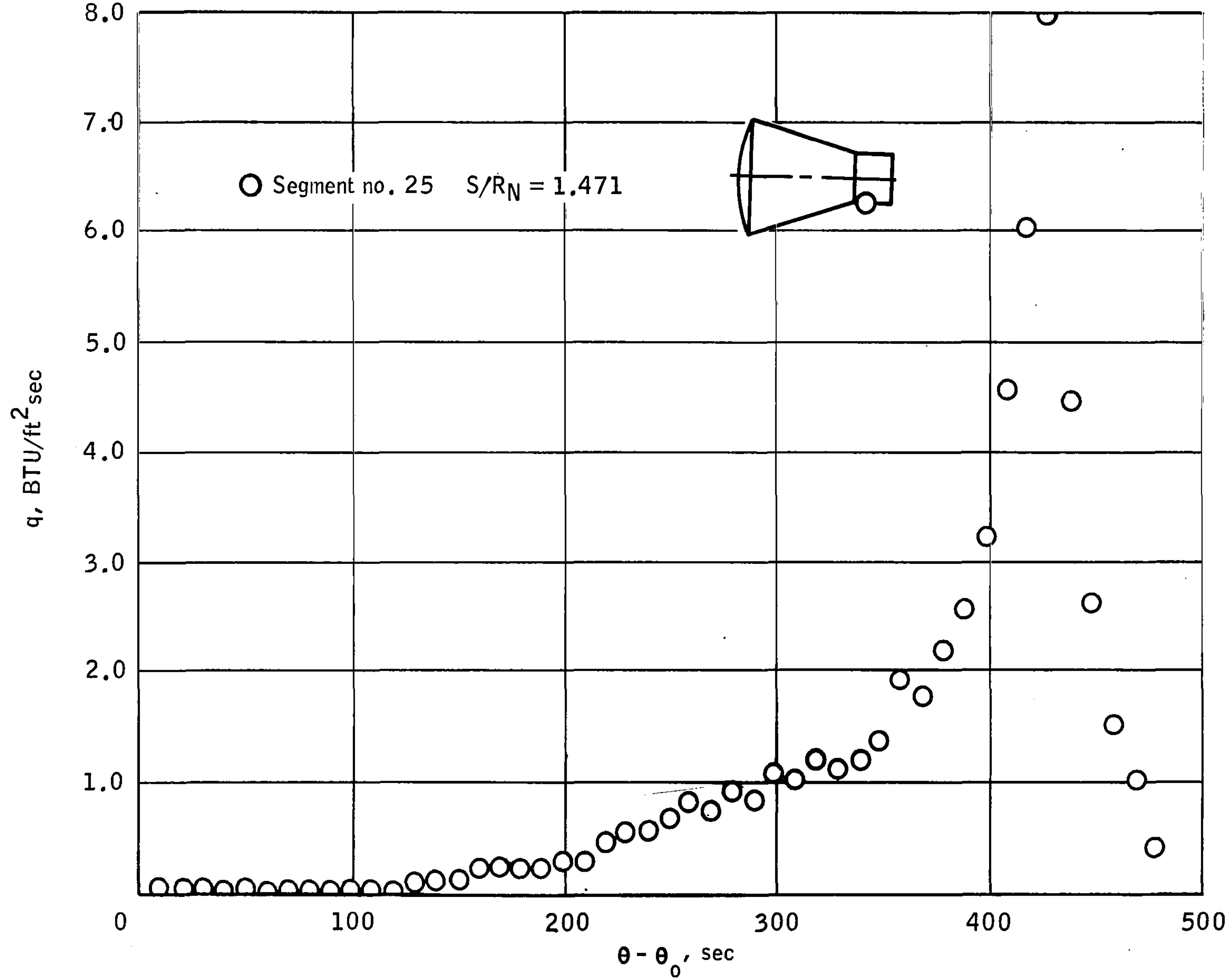

Figure 8h. - Experimental convective heating rate - mission MA-8.

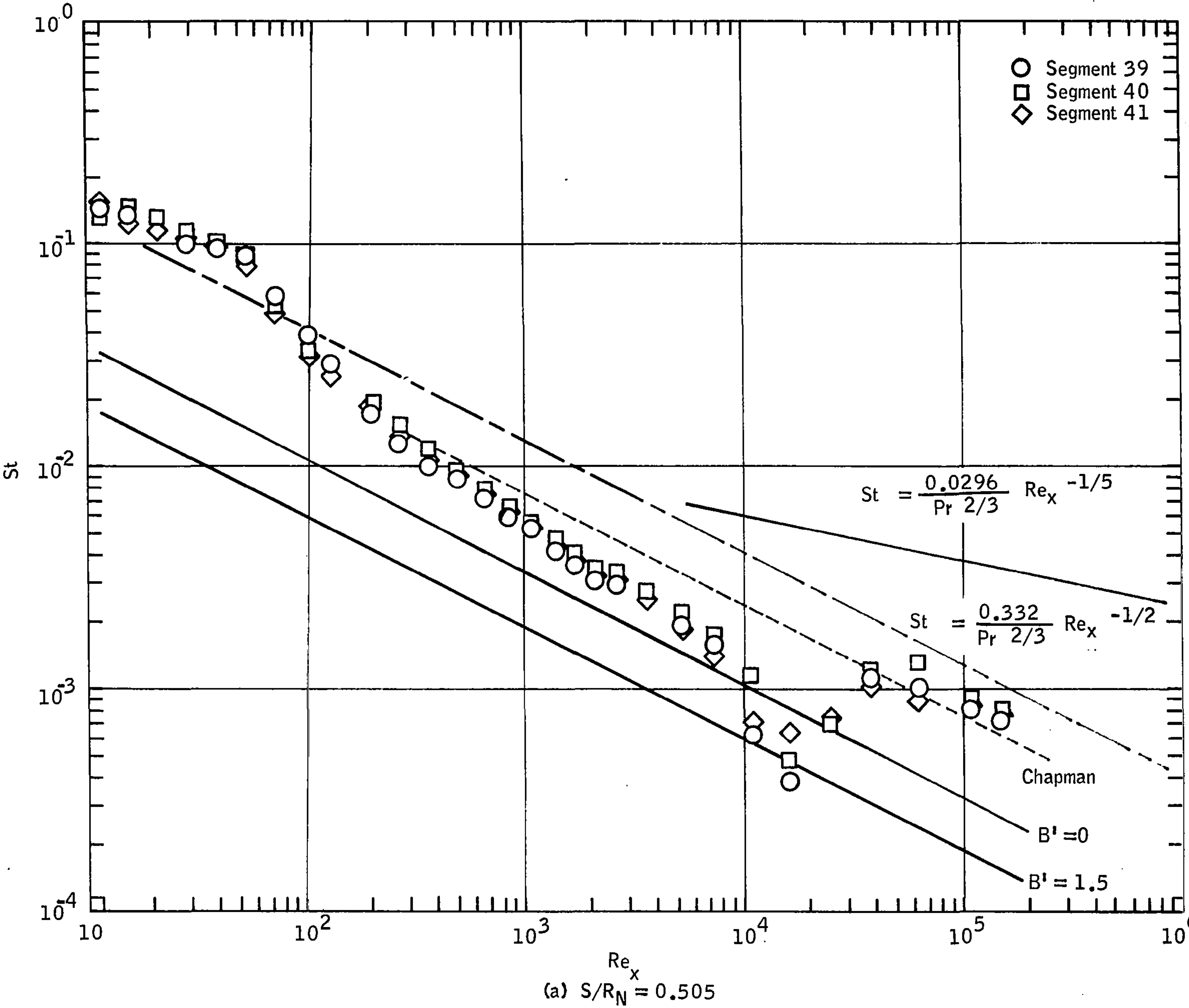

Figure 9. - Comparison of predicted and experimental afterbody heating rates obtained on the spacecraft of MA-5.

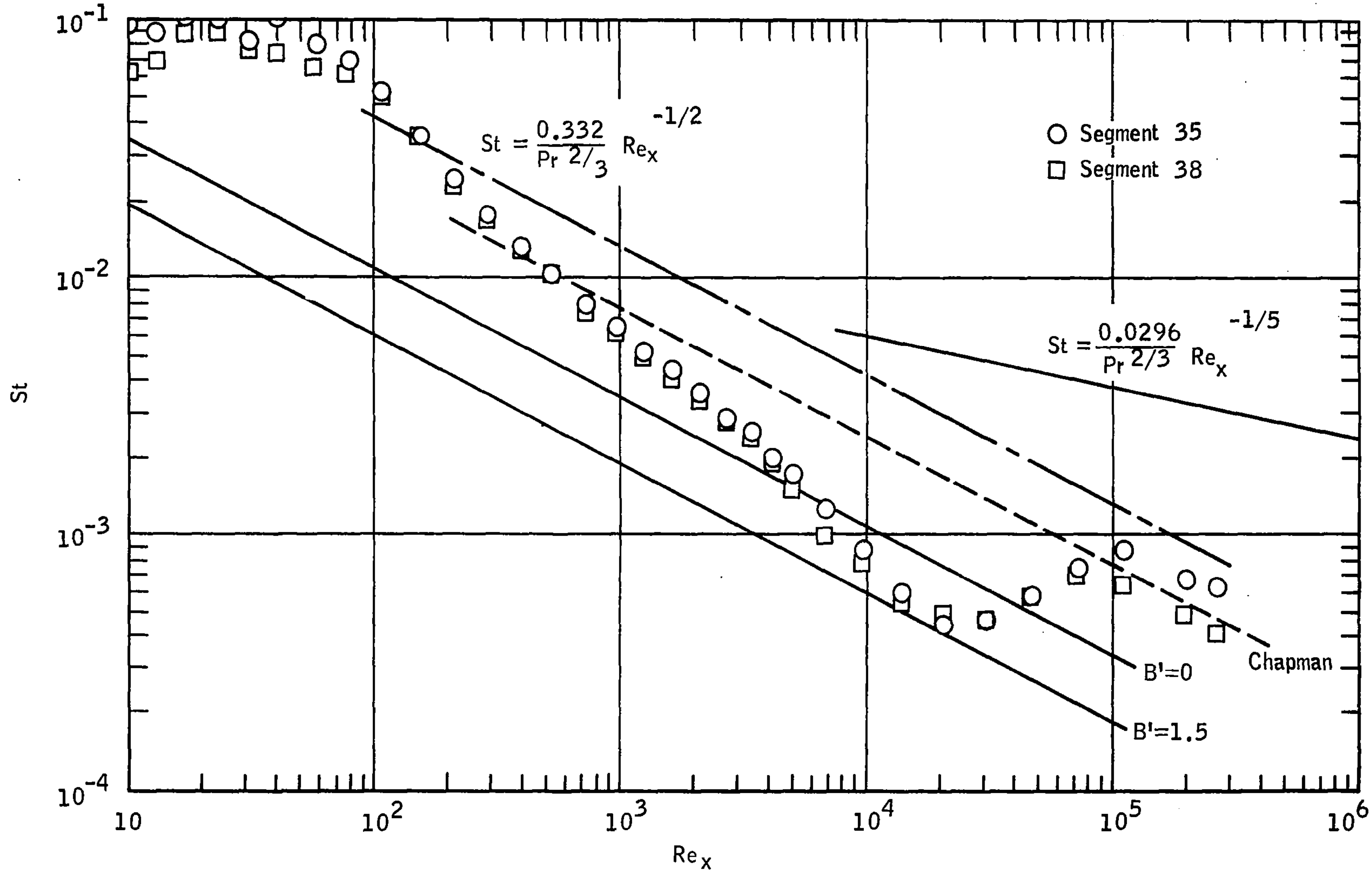

(b) $S/R_N = 0.76$

Figure 9 . - Comparison of predicted and experimental afterbody heating rates obtained on the spacecraft of MA-5.

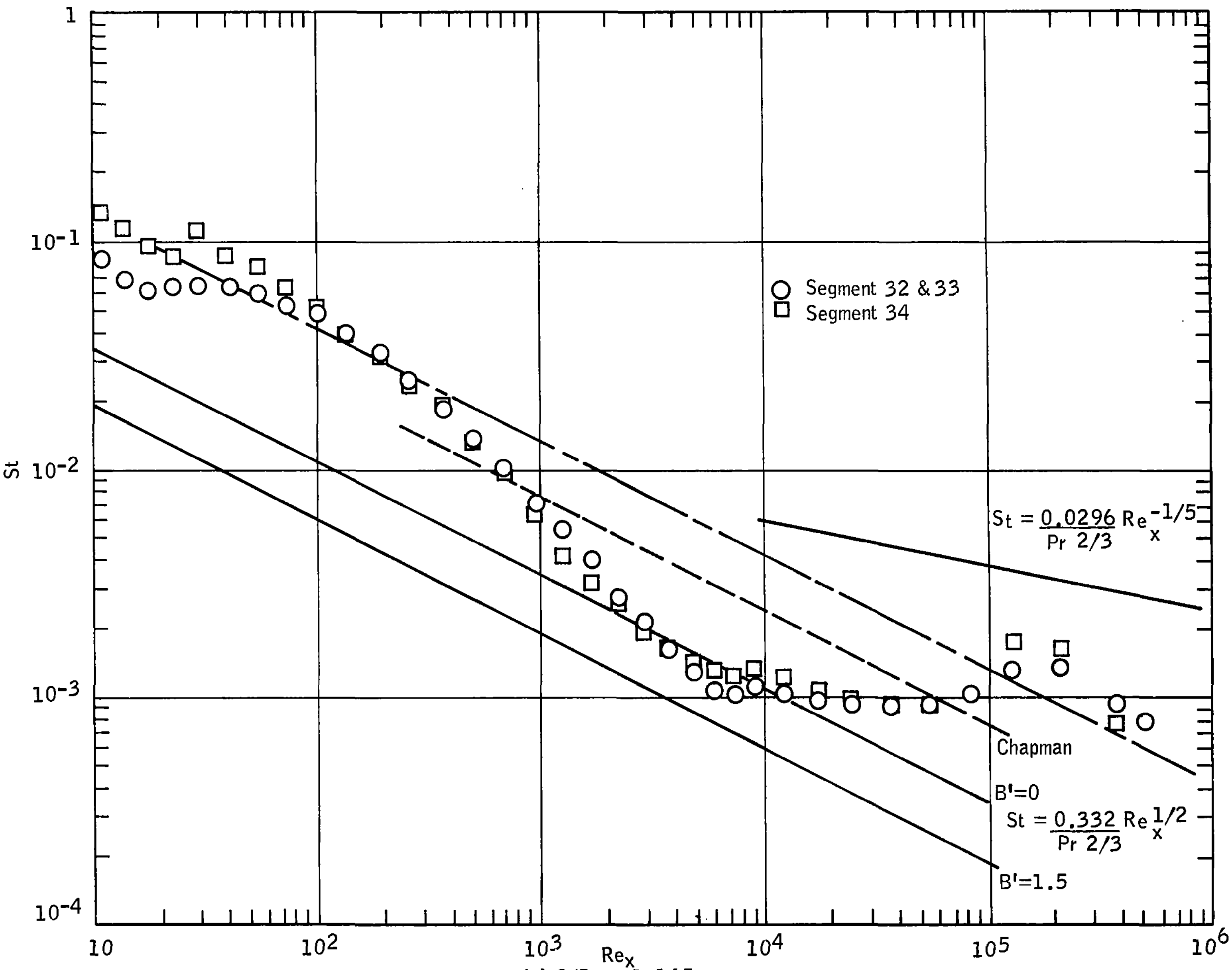

(c) $S/R_N = 1.145$

Figure 9 . - Comparison of predicted and experimental afterbody heating rate obtained on the spacecraft of MA-5.

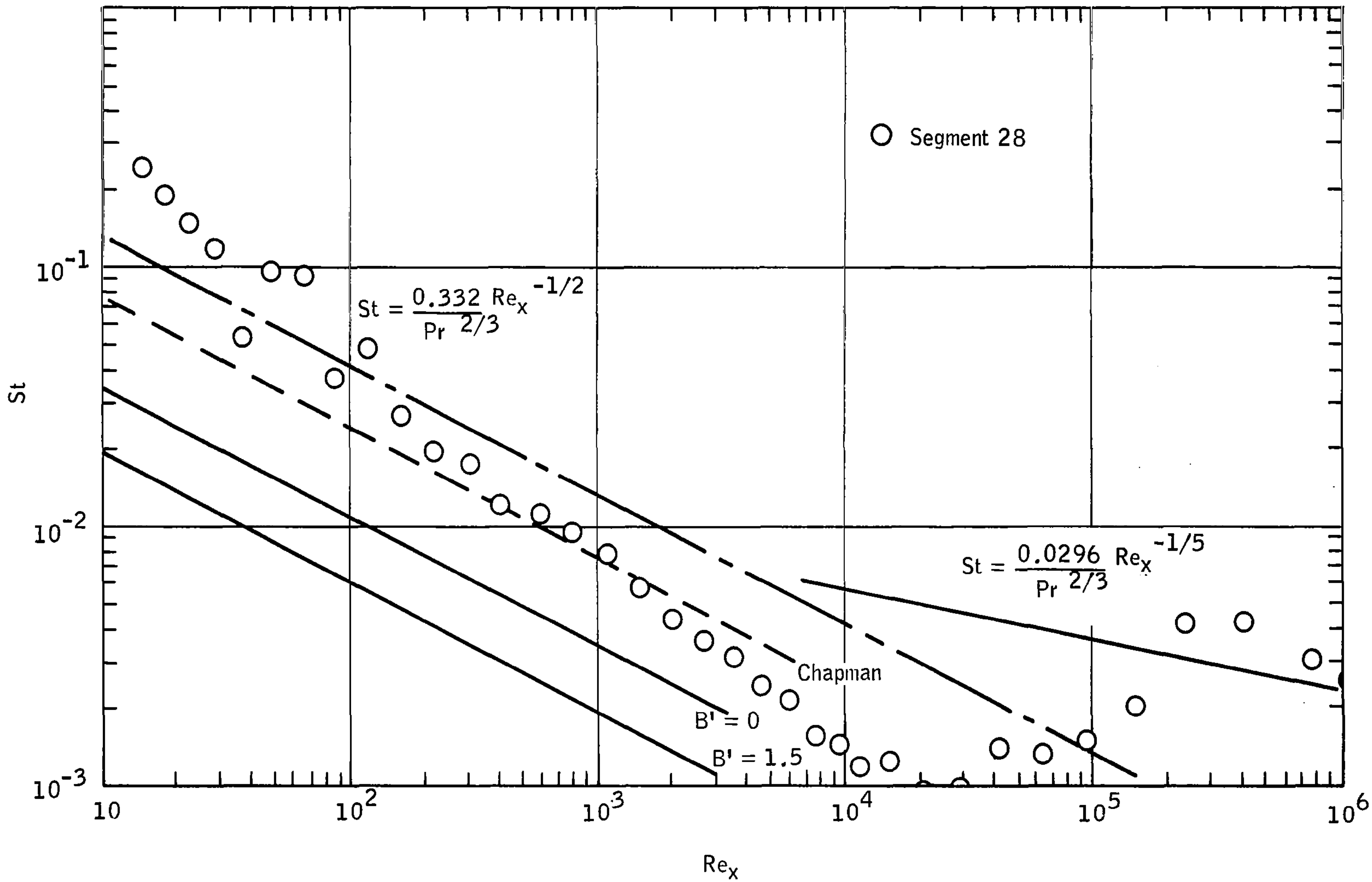

(d) $S/R_N = 1.45$

Figure 9. - Comparison of predicted and experimental afterbody heating rates obtained on the spacecraft of MA-5.

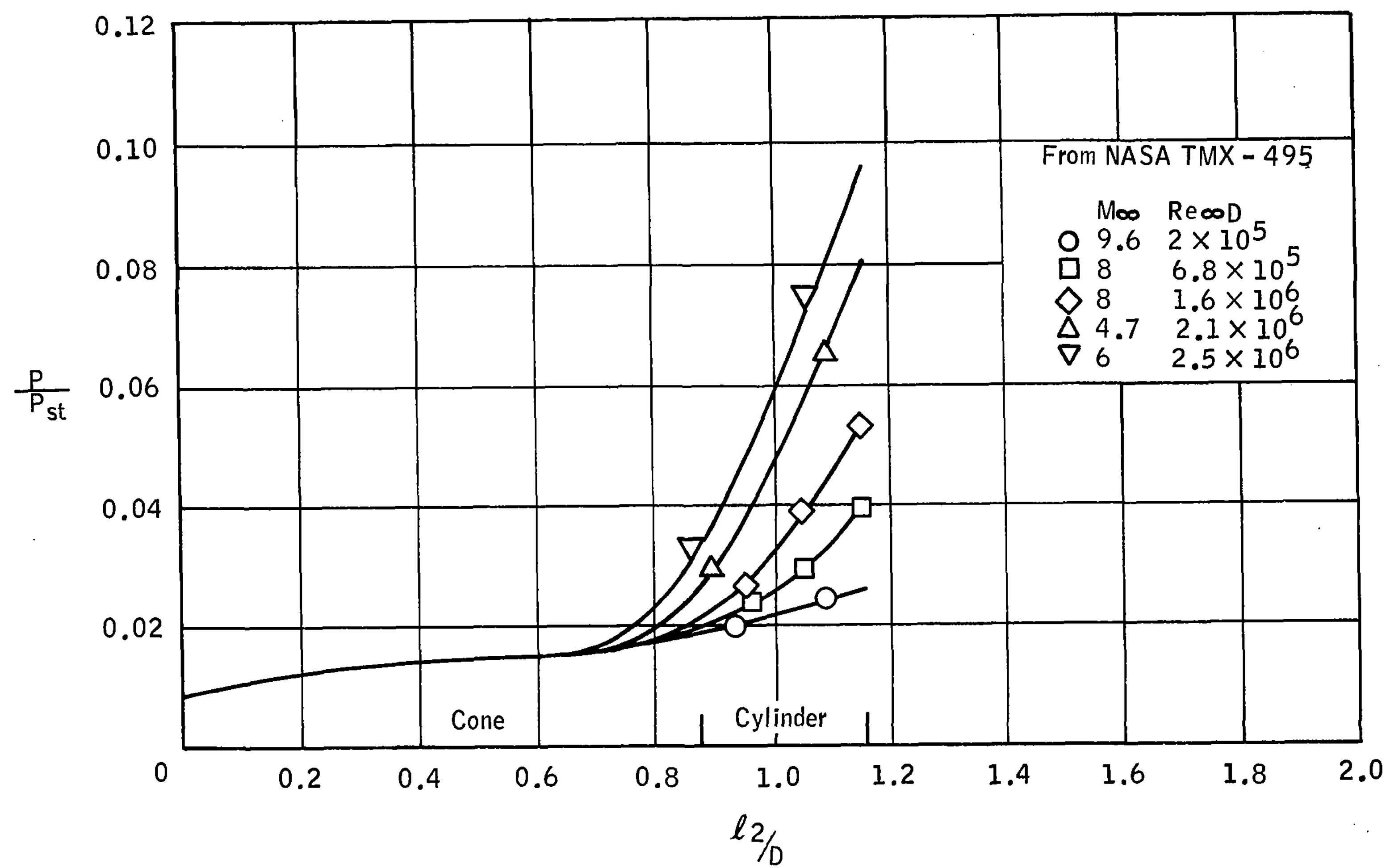

Figure 10. - Experimental pressure distribution on Project Mercury capsule afterbody at zero incidence ~ from Weston & Swanson.

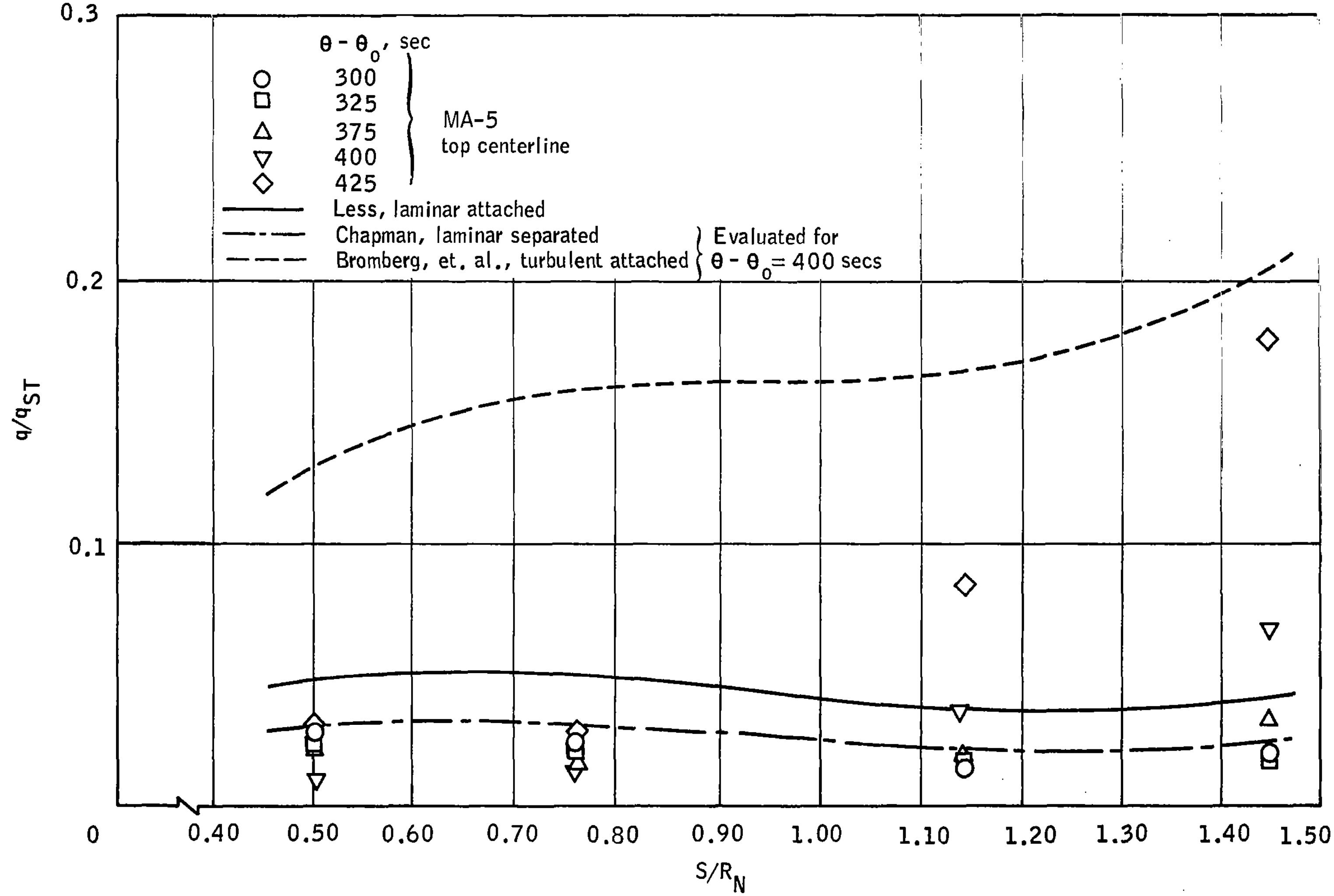

Figure 11. - Comparison of streamwise distribution of experimental heating with applicable theoretical predictions.

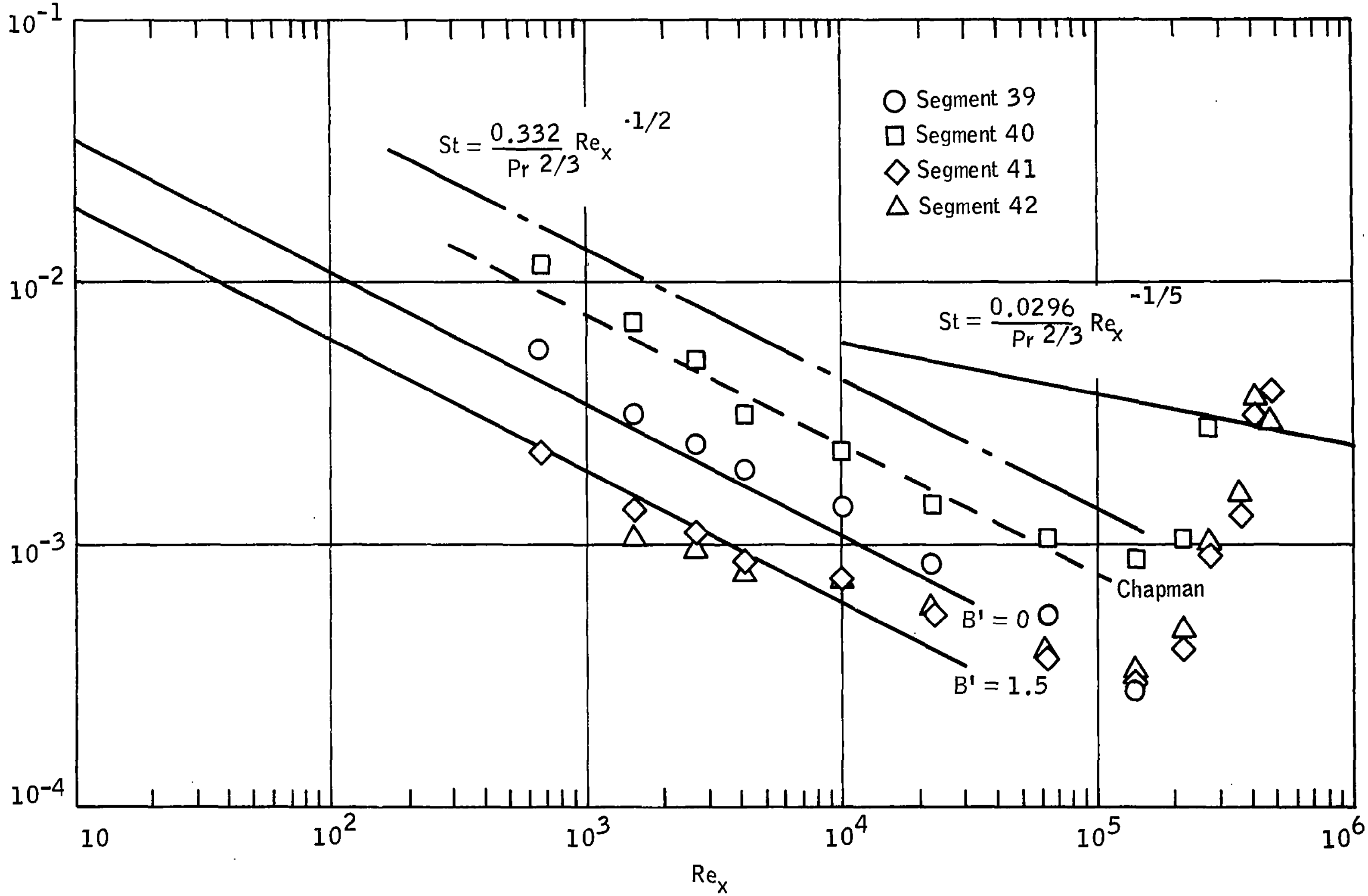

(a) $S/R_N = 0.503$

Figure 12. - Comparison of predicted and experimental afterbody heating rates obtained on the spacecraft of MA-2.

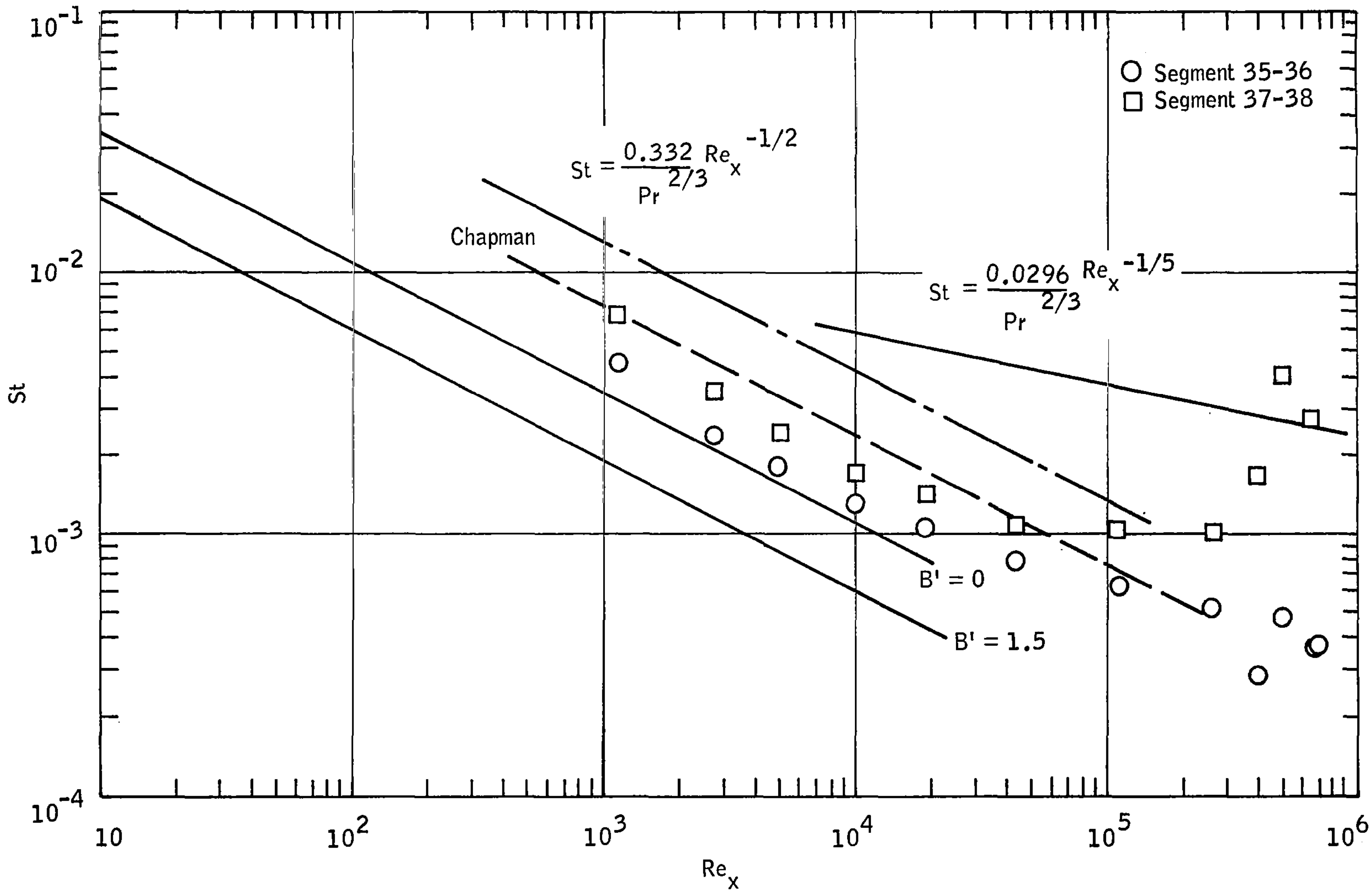

(b) $S/R_N = 0.76$

Figure 12. - Comparison of predicted and experimental afterbody heating rates obtained on the spacecraft of MA-2.

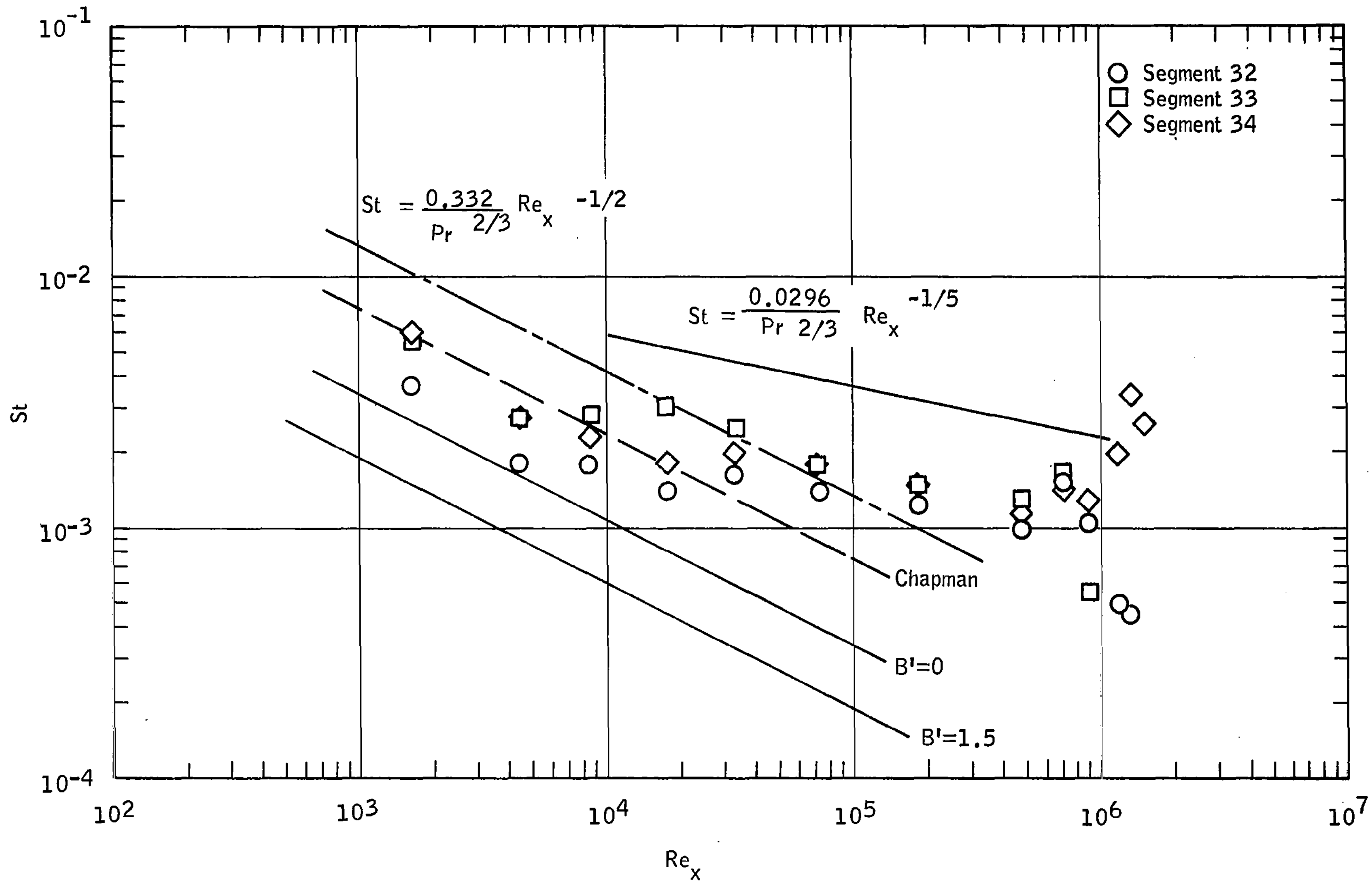

(c) $S/R_N = 1.145$

Figure 12. - Comparison of predicted and experimental afterbody heating rates obtained on the spacecraft of MA-2.

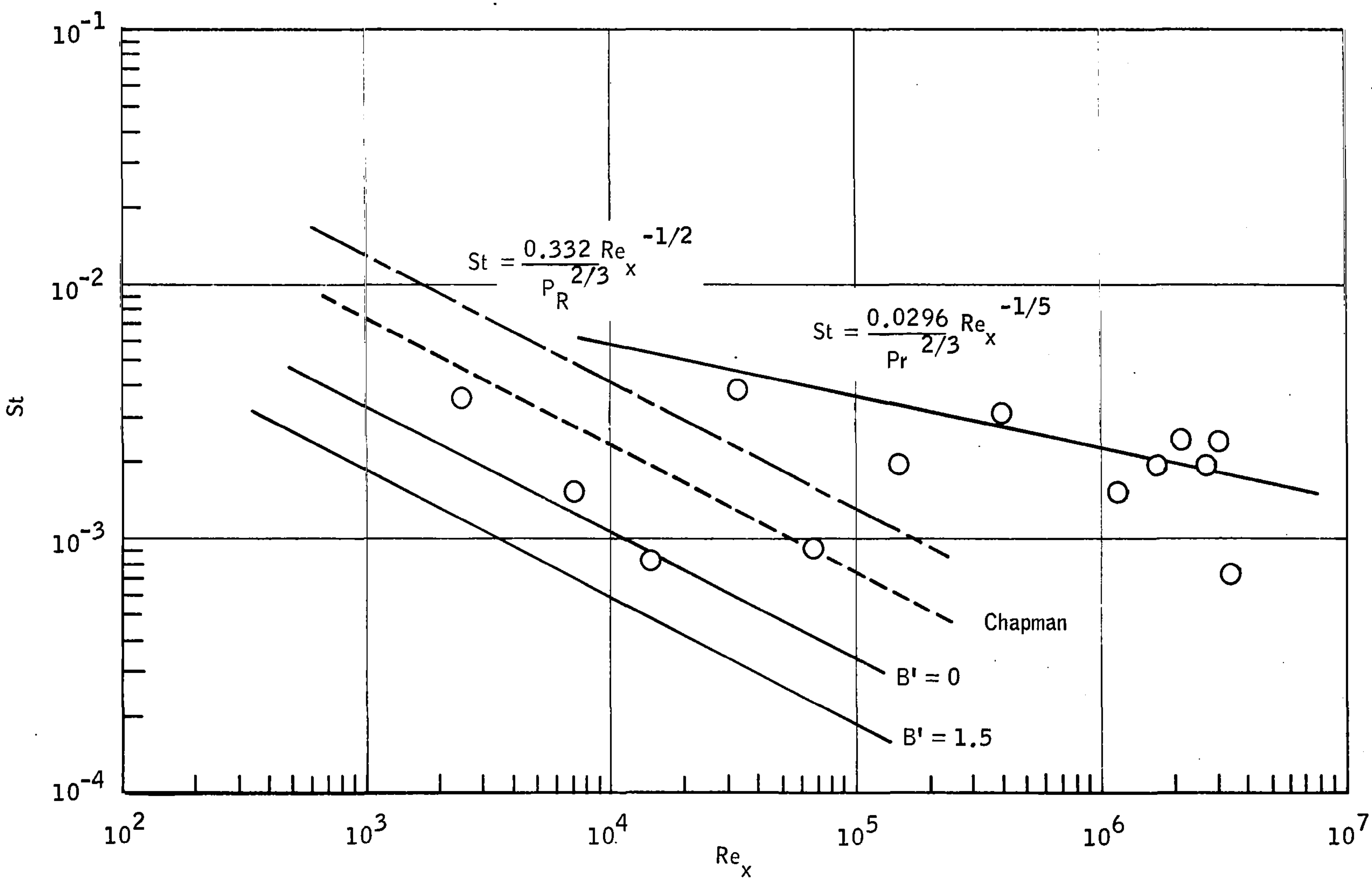

(d) $S/R_N = 1.45$

Figure 12. - Comparison of predicted and experimental afterbody heating rates obtained on the spacecraft of MA-2.

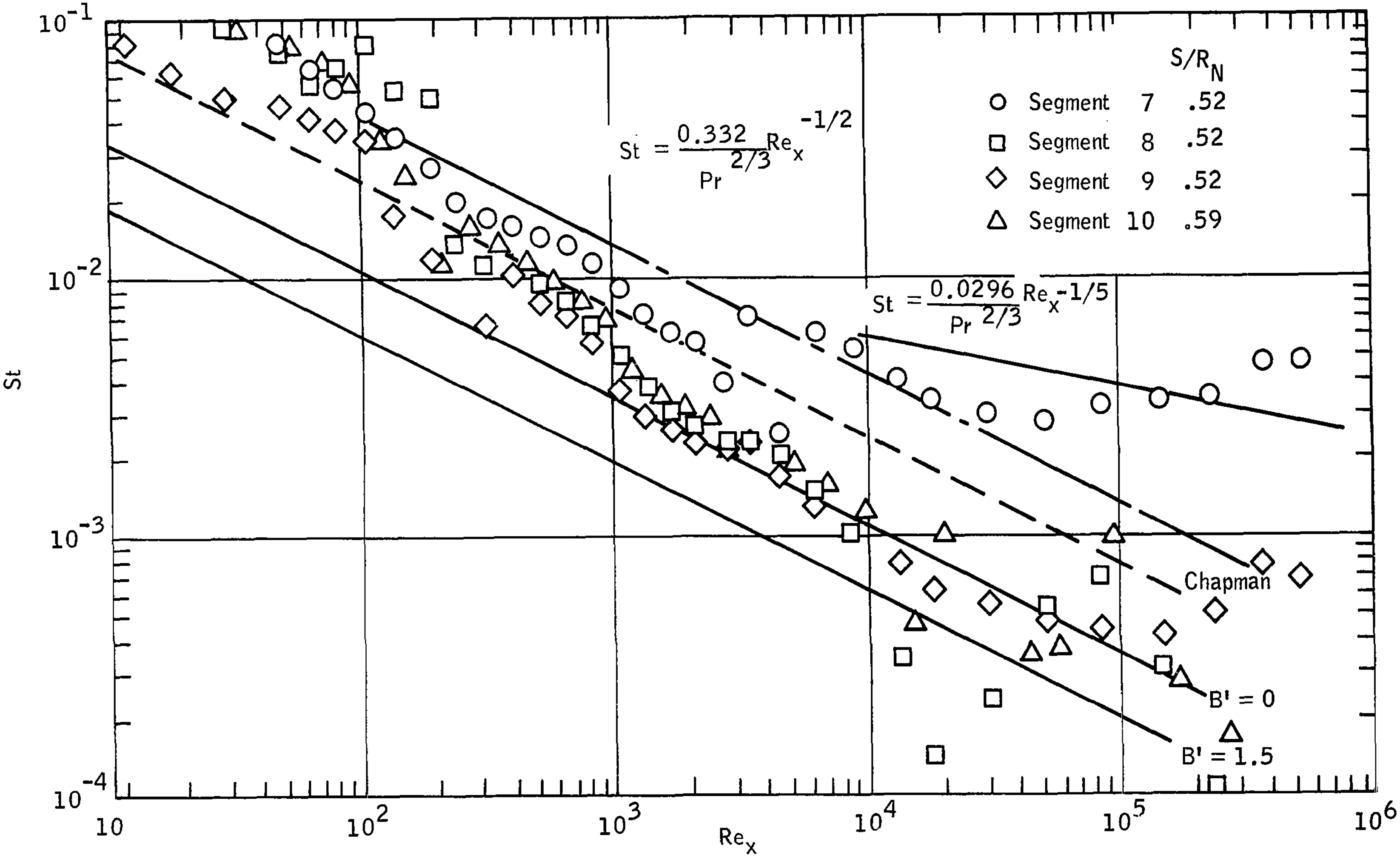

(a) Forward cone.

Figure 13. - Comparison of predicted and experimental afterbody heating rates obtained on the spacecraft of MA-7.

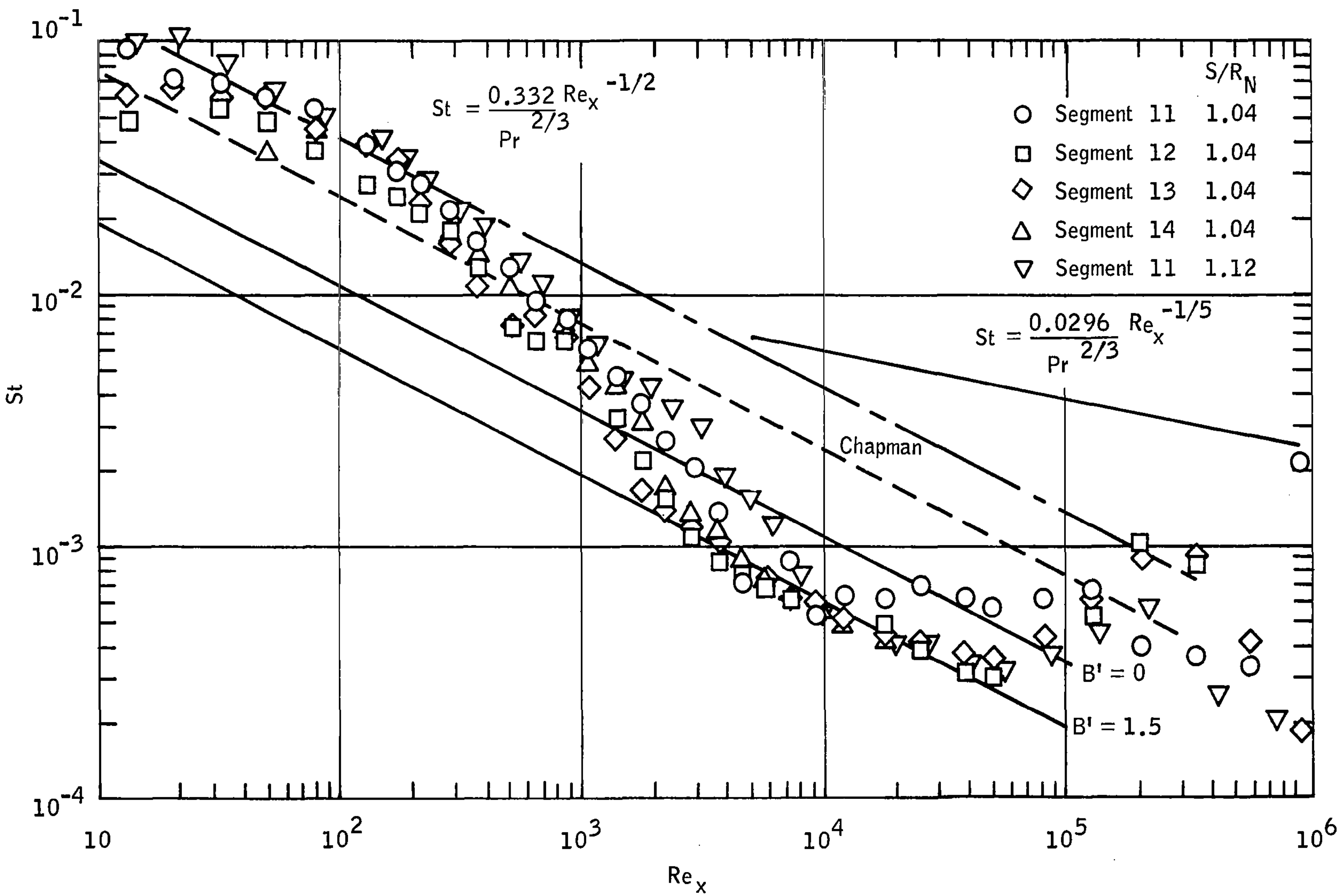

(b) Aft cone.

Figure 13. - Comparison of predicted and experimental afterbody heating rates obtained on the spacecraft of MA-7.

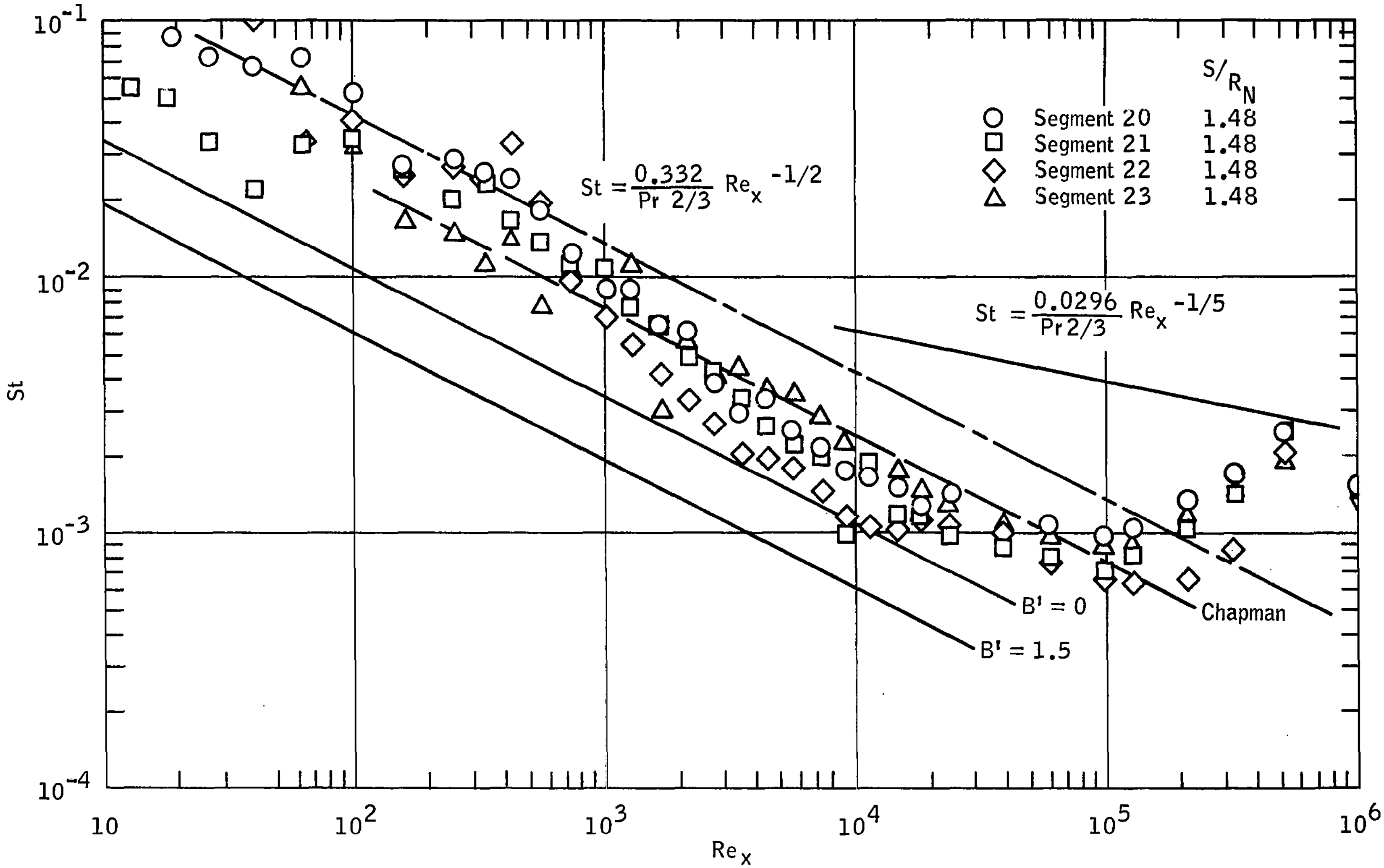

(c) Cylinder.

Figure 13. - Comparison of predicted and experimental afterbody heating rates obtained on the spacecraft of MA-7.

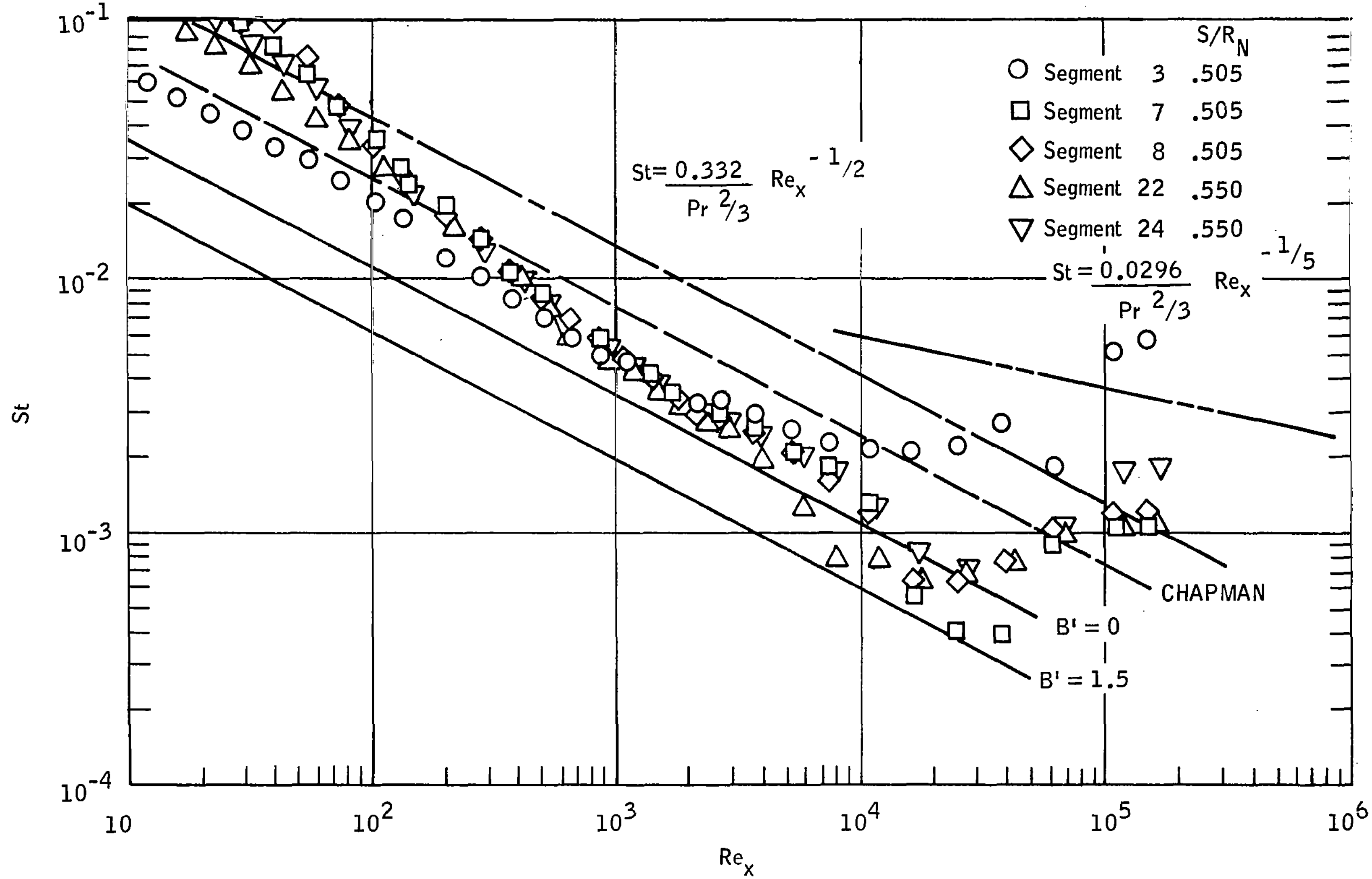

(a) Forward cone.

Figure 14. - Comparison of predicted and experimental afterbody heating rates obtained on the spacecraft of MA-8.

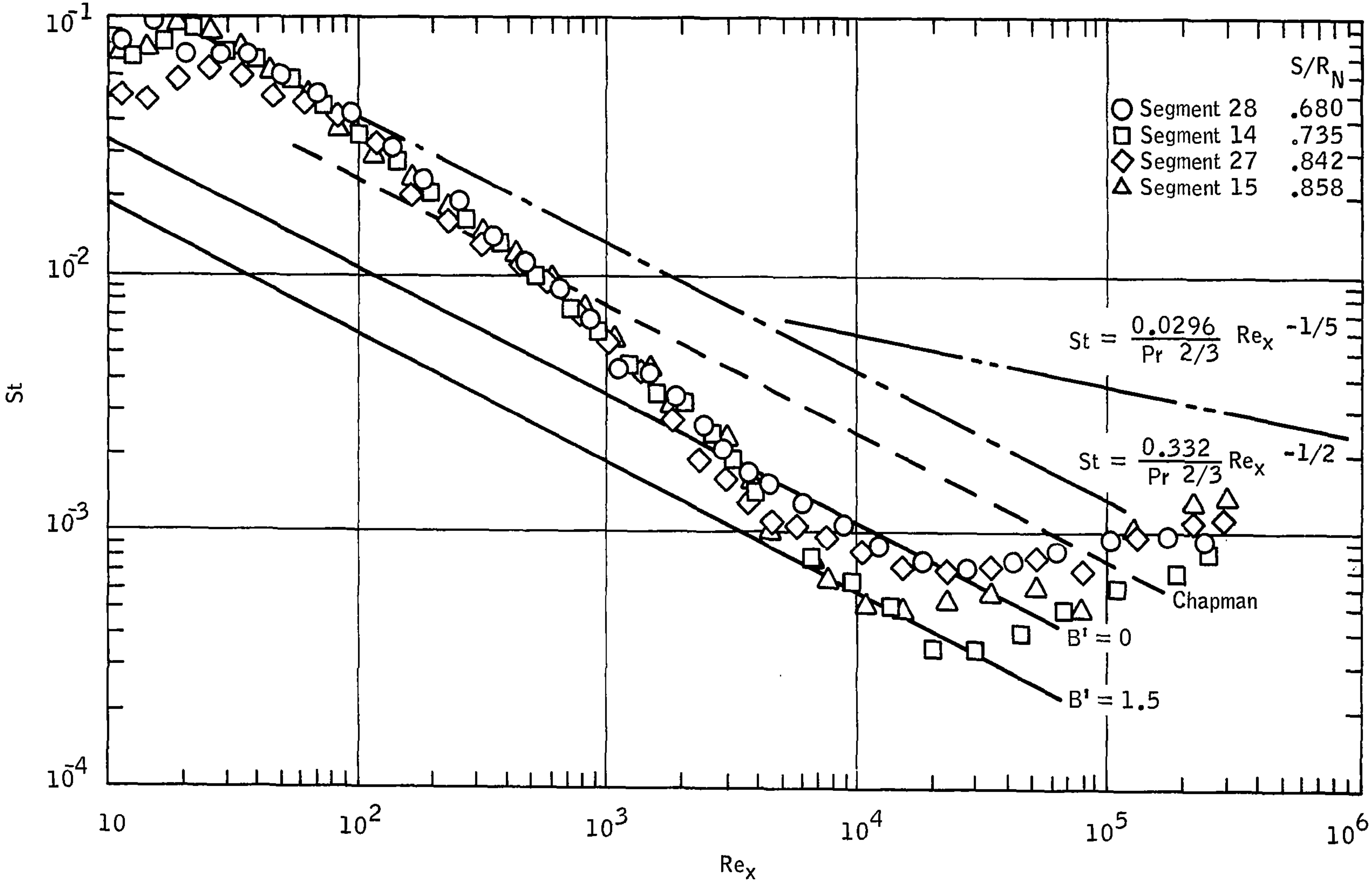

(b) Mid cone

Figure 14. - Comparison of predicted and experimental afterbody heating rates obtained on the spacecraft of MA-8.

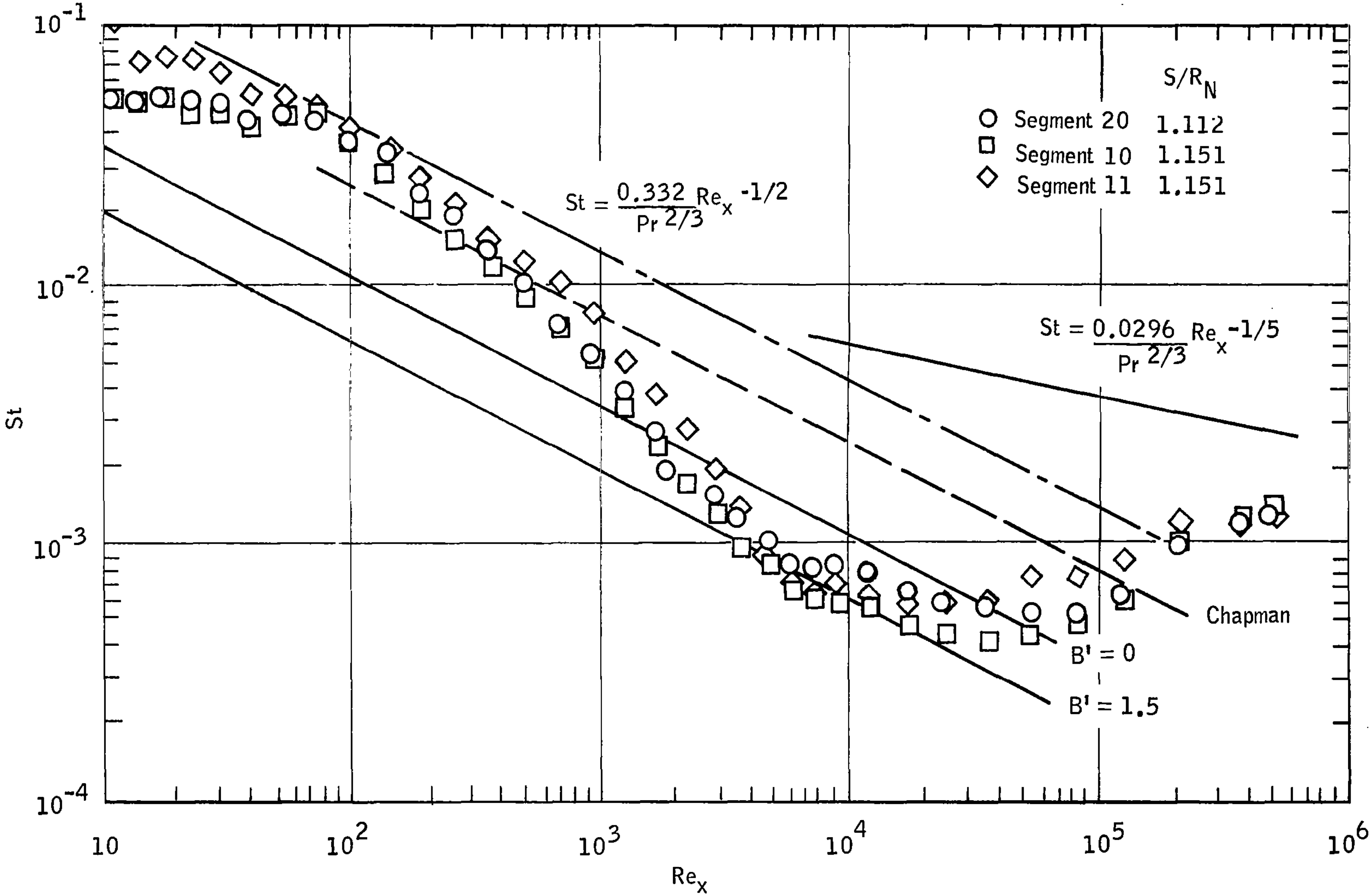

(c) Aft cone.

Figure 14. - Comparison of predicted and experimental afterbody heating rates obtained on the spacecraft of MA-8.

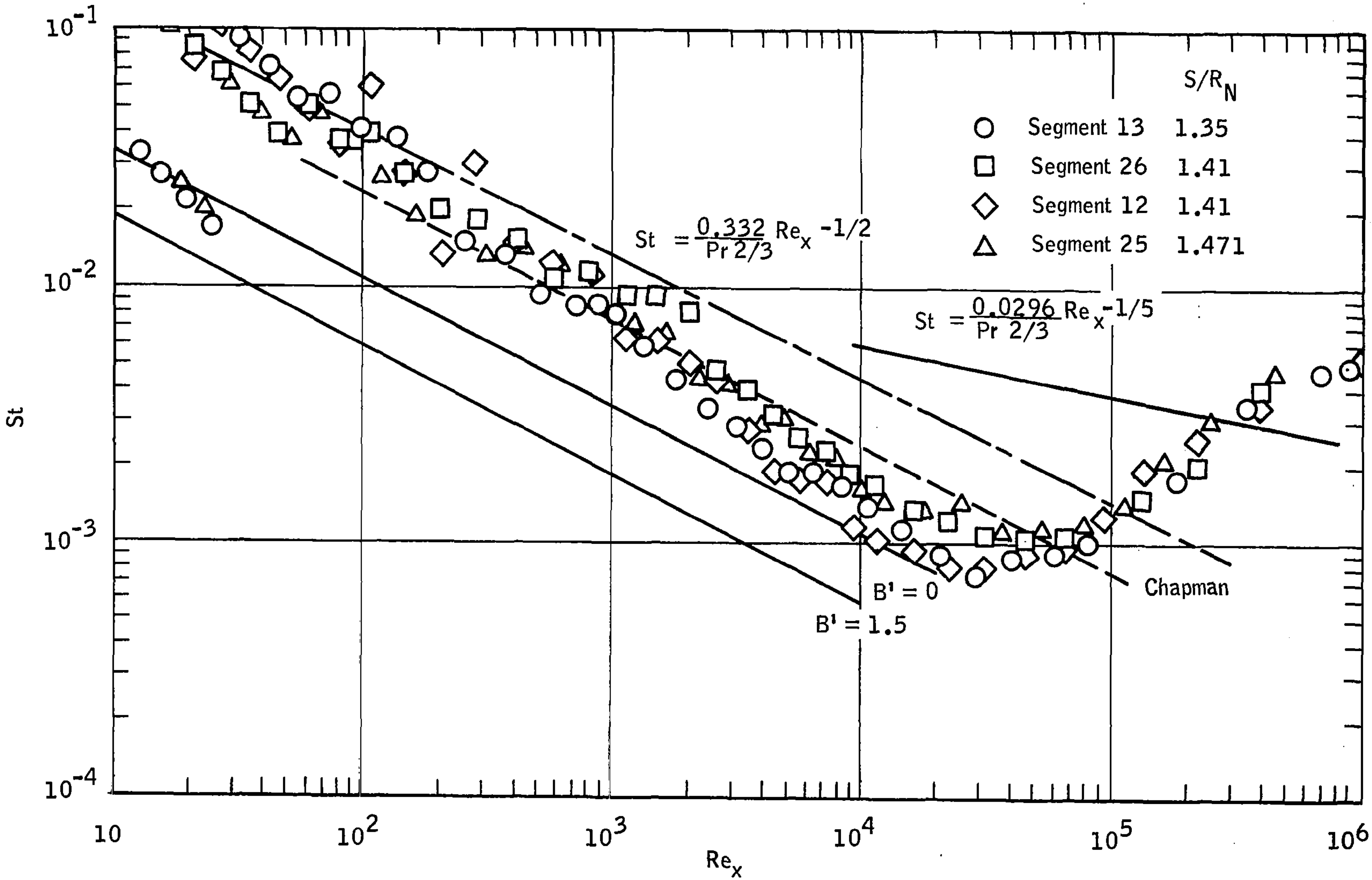

(d) Cylinder.

Figure 14. - Comparison of predicted and experimental afterbody heating rates obtained on the spacecraft of MA-8.

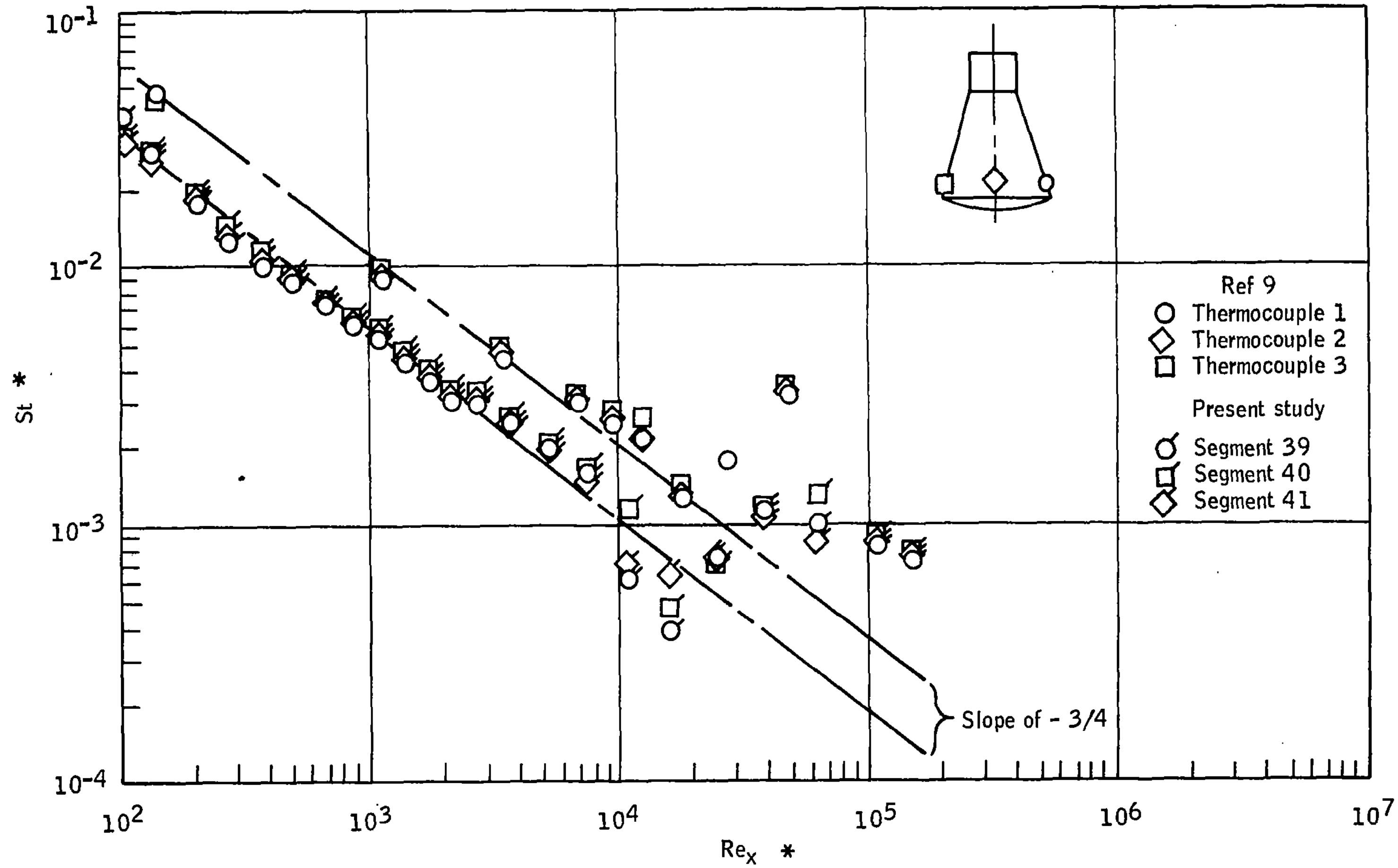

$S/R_N = .505$

Figure 15. - Comparison of NASA and LMSC data obtained from the spacecraft of Mercury-Atlas no. 5.

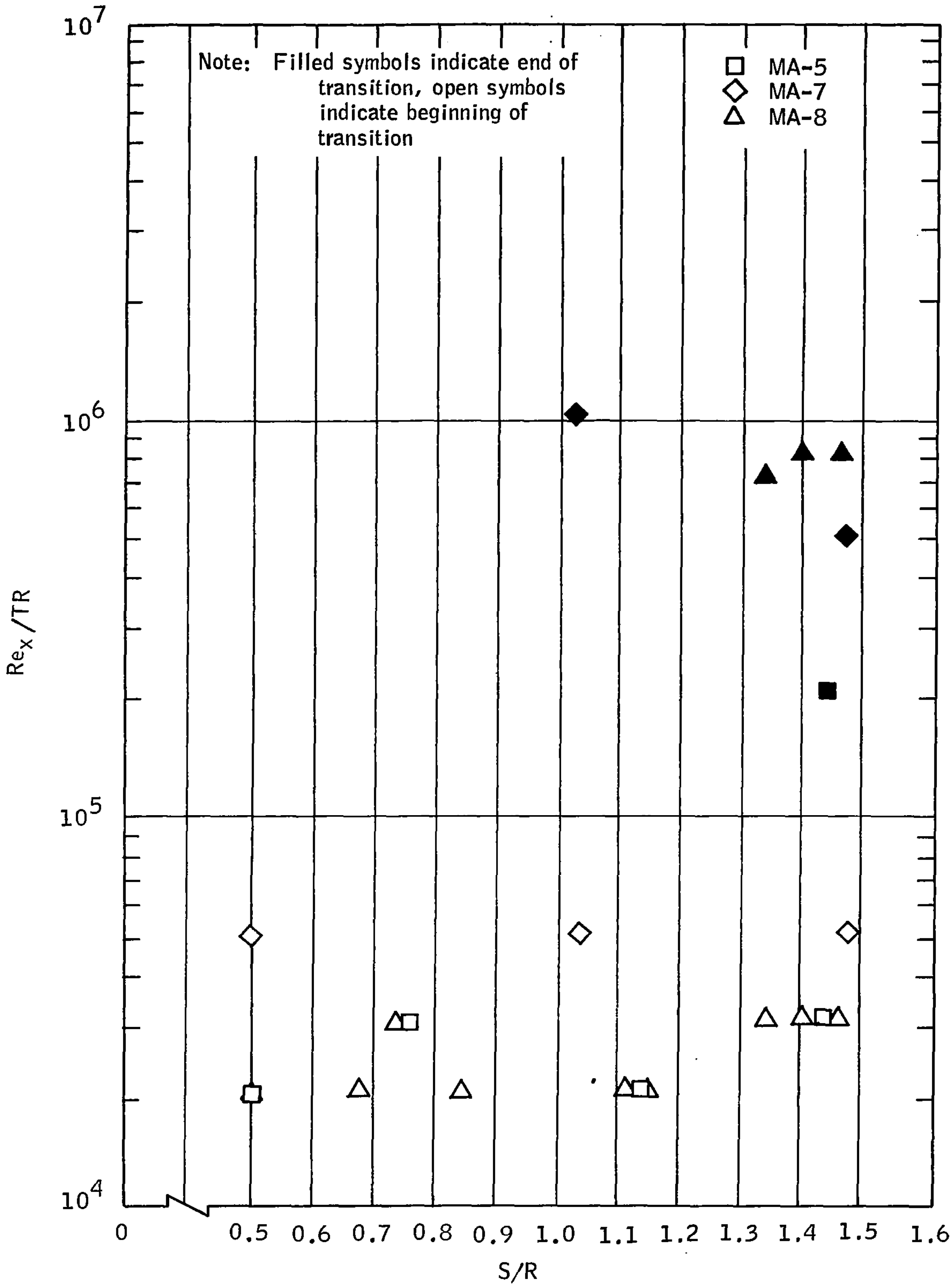

Figure 16. - Range of transitional Reynolds numbers inferred from Mercury afterbody data.

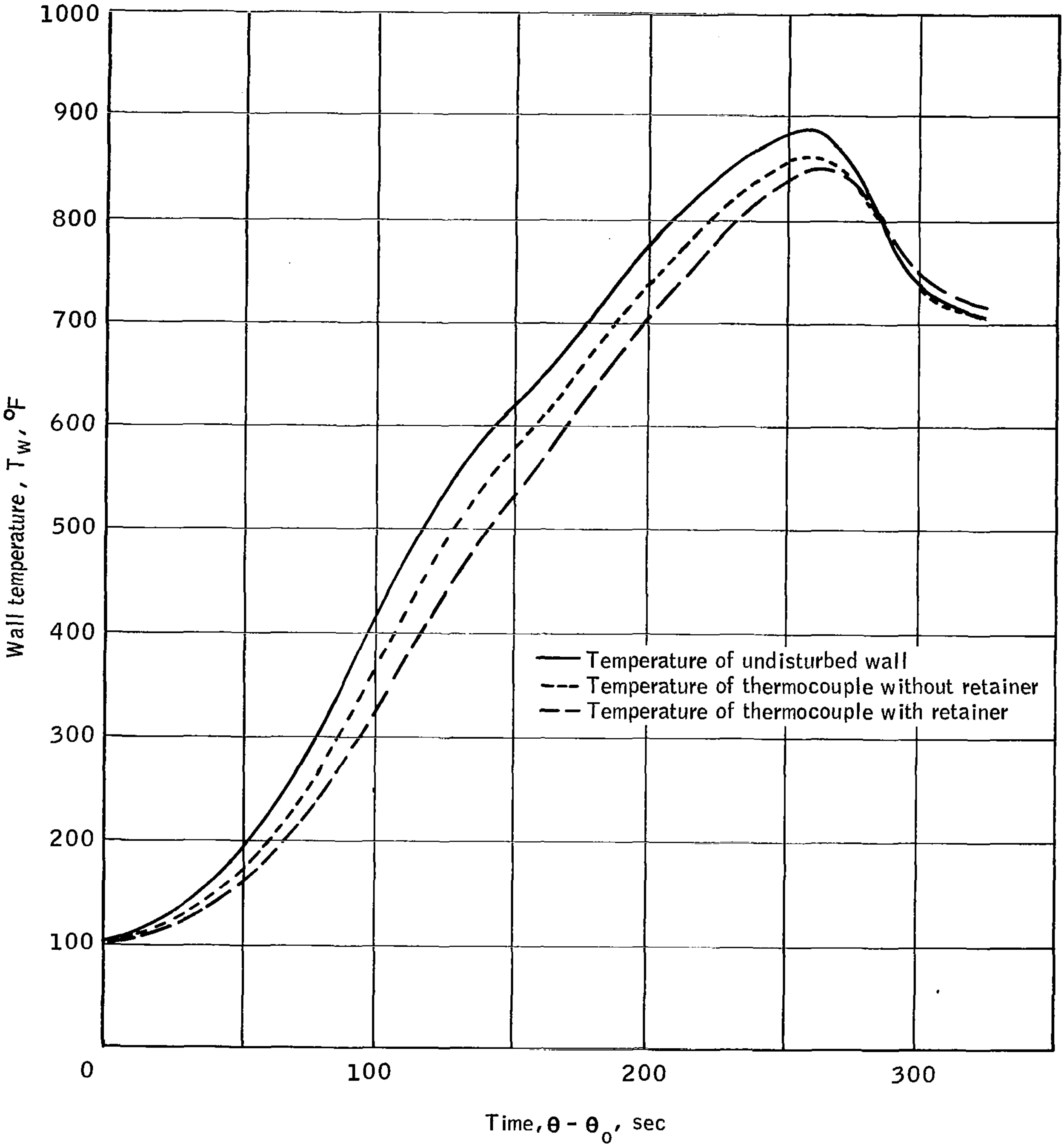

Figure 17. - Effect of thermocouple installation on wall temperature for a prescribed heating rate.

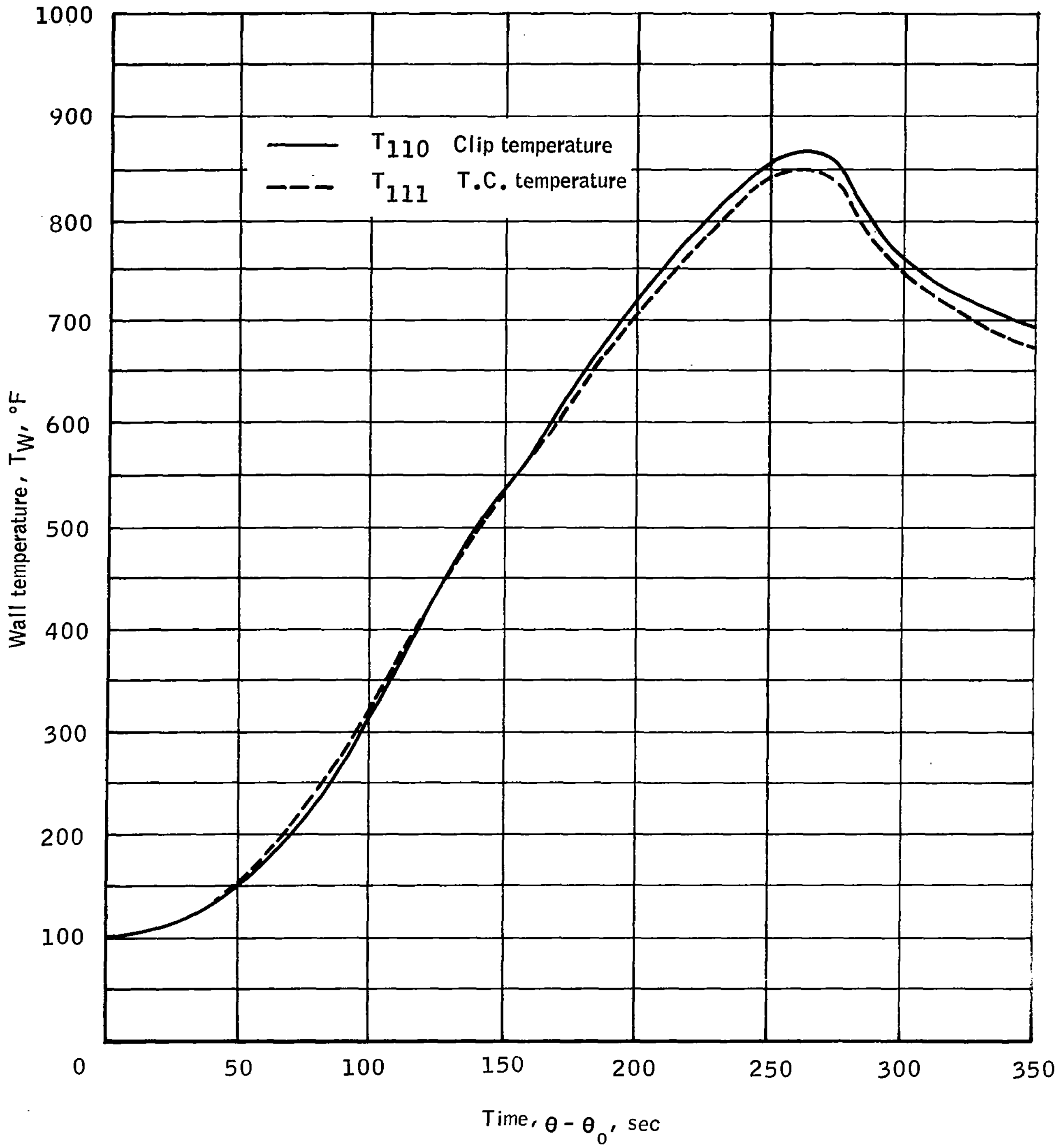

Figure 18. - Comparison of thermocouple and retainer clip temperatures for Mercury thermocouple installation.

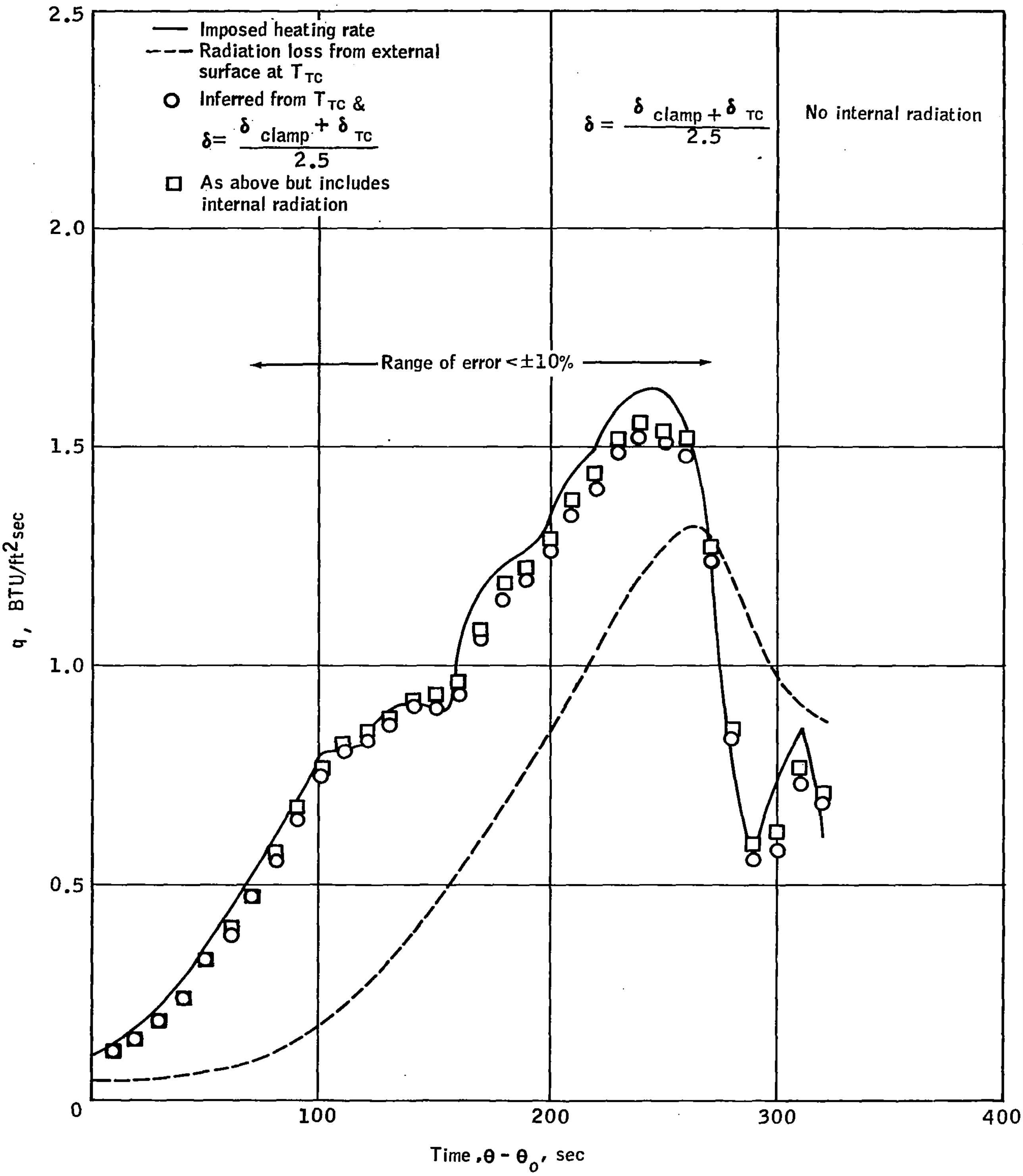

Figure 19.- Comparison of input and inferred heat flux histories with and without internal radiation

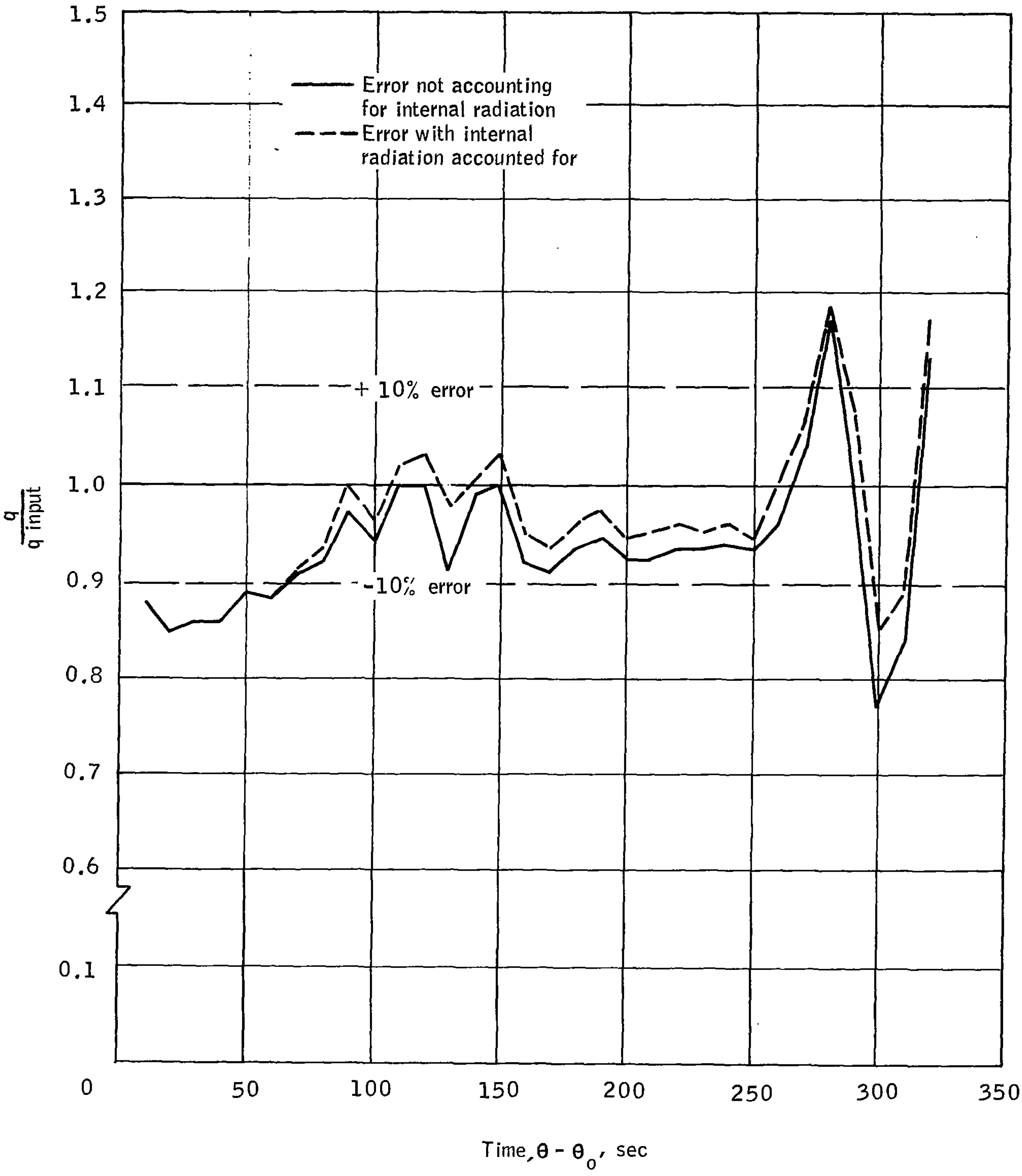

Figure 20. - Relative error in heating rate inferred from thin skin data reduction.

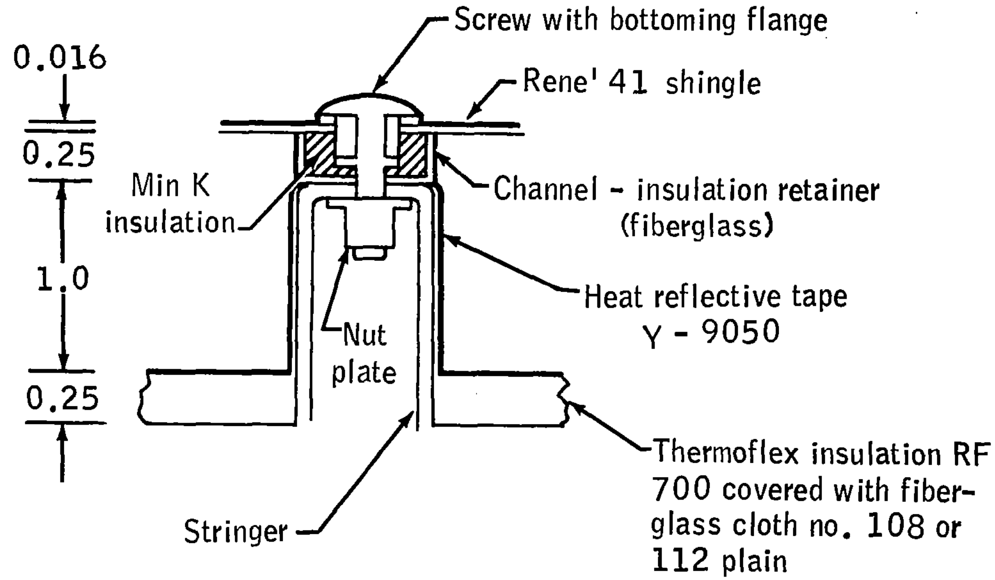

Figure 21. - Typical shingle installation conical section Mercury capsule afterbody.

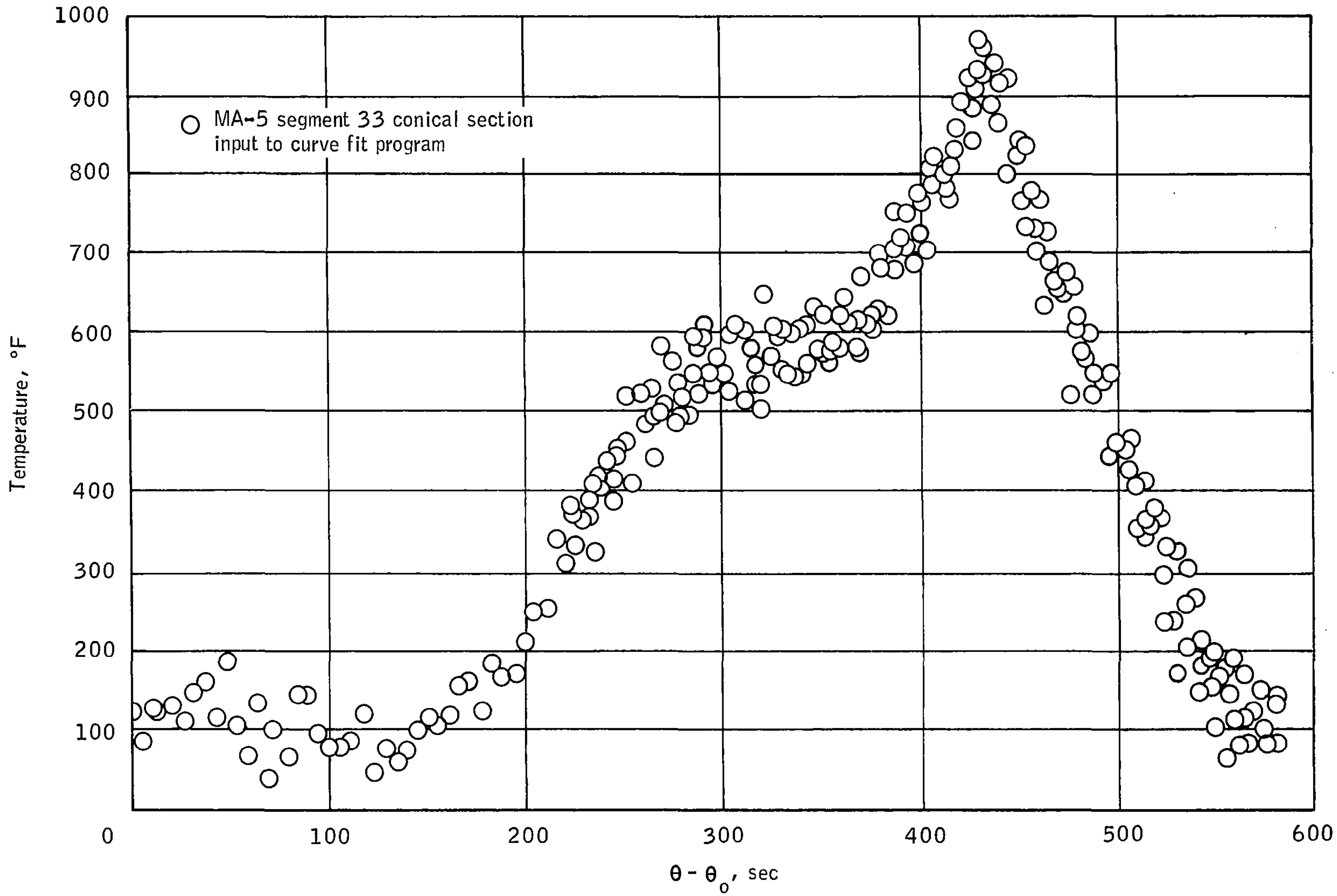

Figure 22.- Raw telemetered temperature data of segment 33 project Mercury flight MA-5.

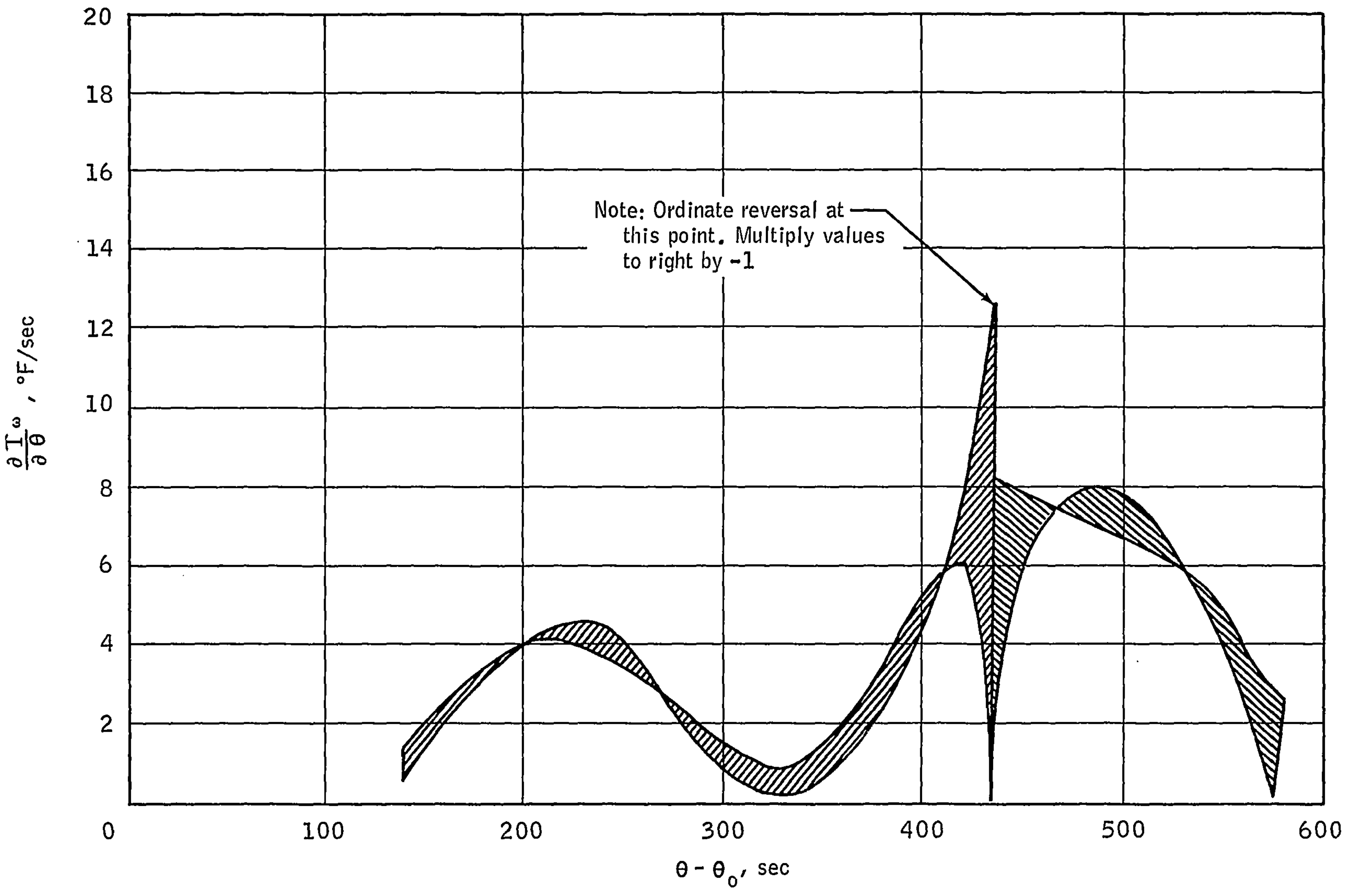

Figure 23 - Envelope of wall temperature derivative as obtained from several data smoothing procedures.

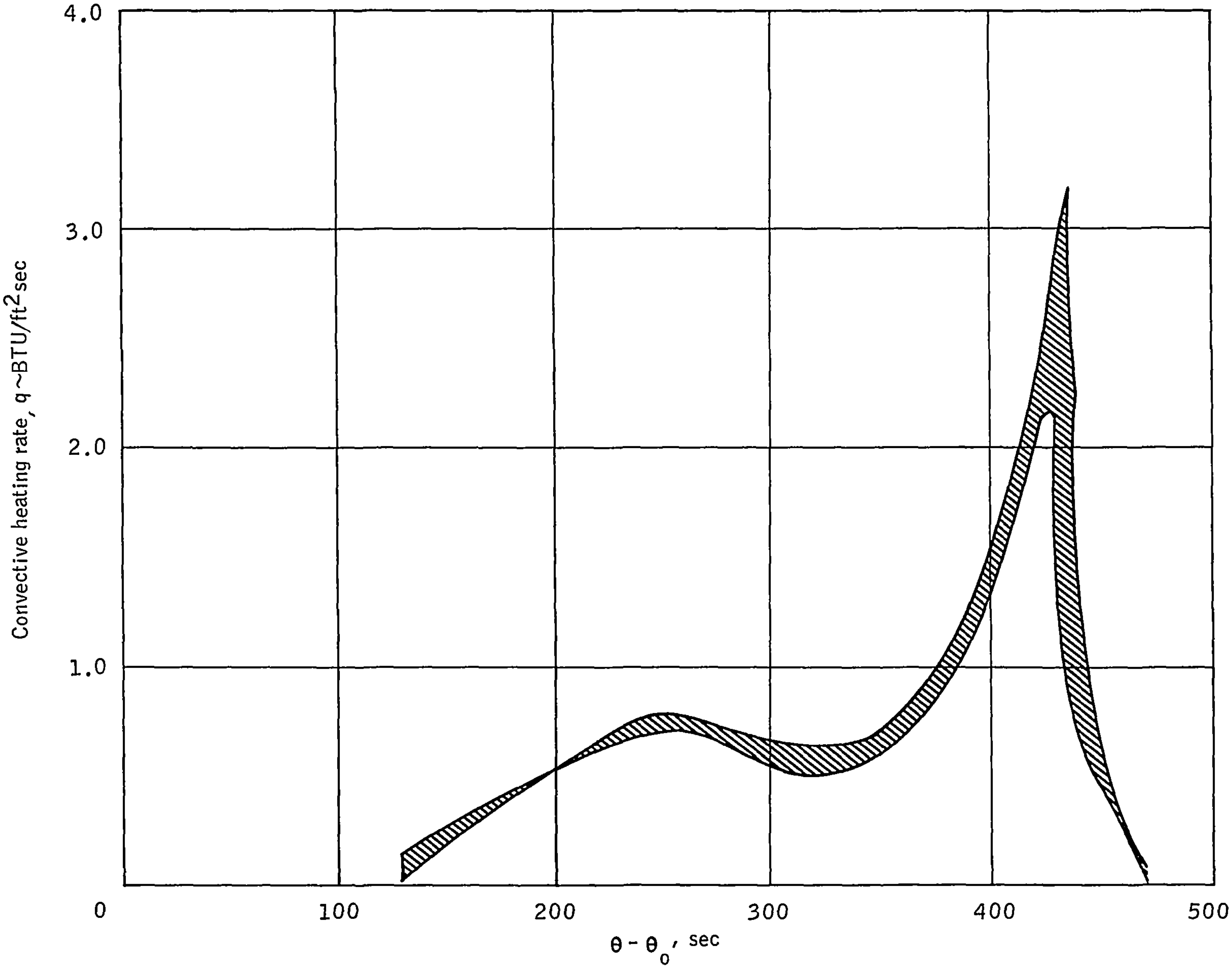

Figure 24. - Envelope of uncertainty in wall heating rate due to errors in $\partial T/\partial \theta$ ~ flight MA-5, segment 33.

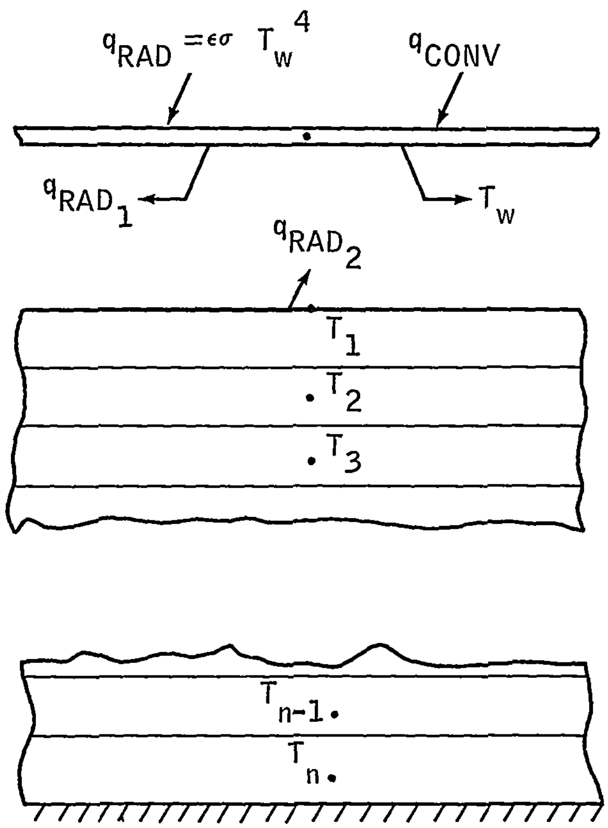

Figure 25. - Configuration of a section through the Mercury capsule afterbody.

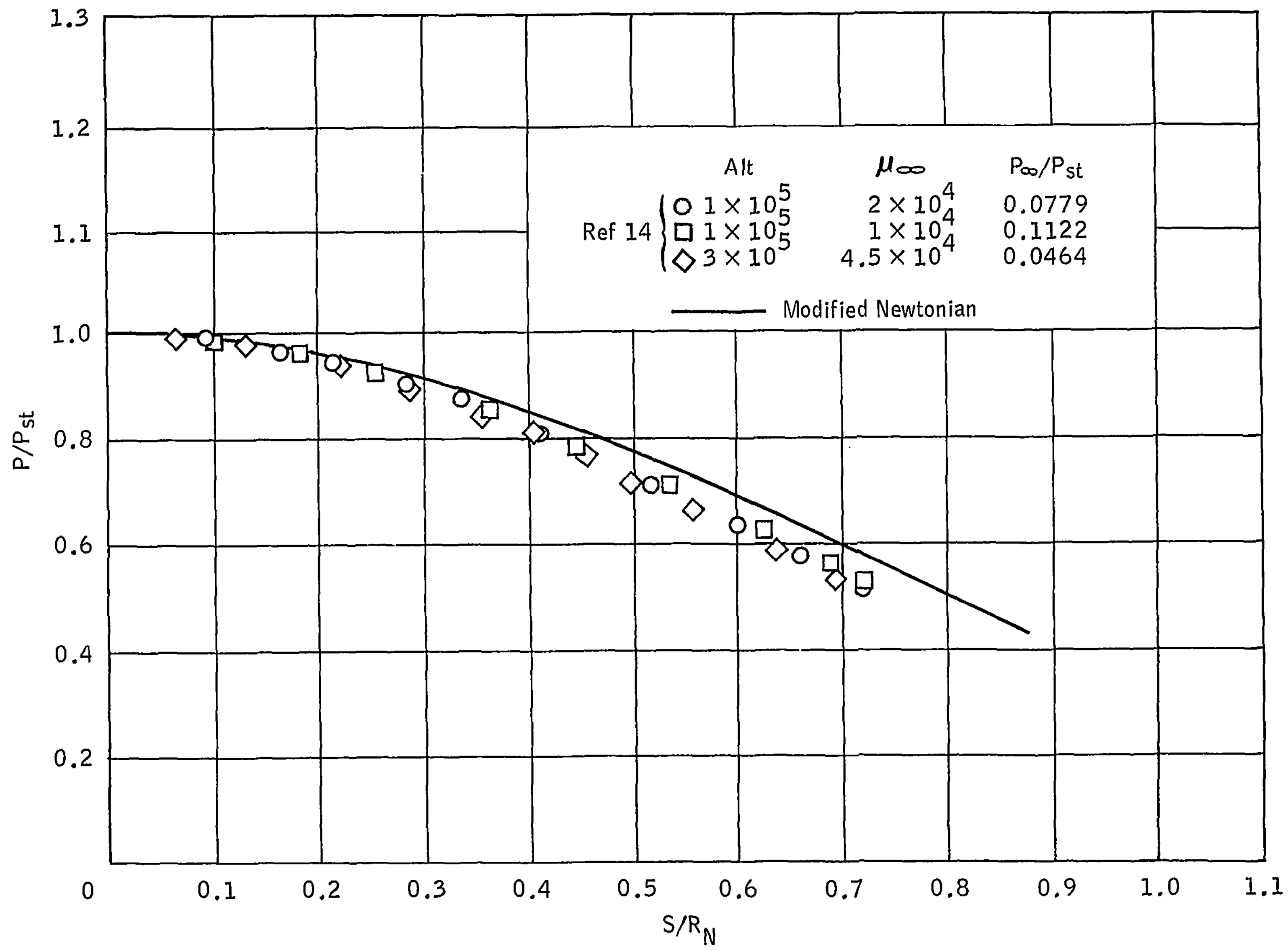

Figure 26. - Pressure distribution over spherically blunted bodies at various velocities and altitudes.

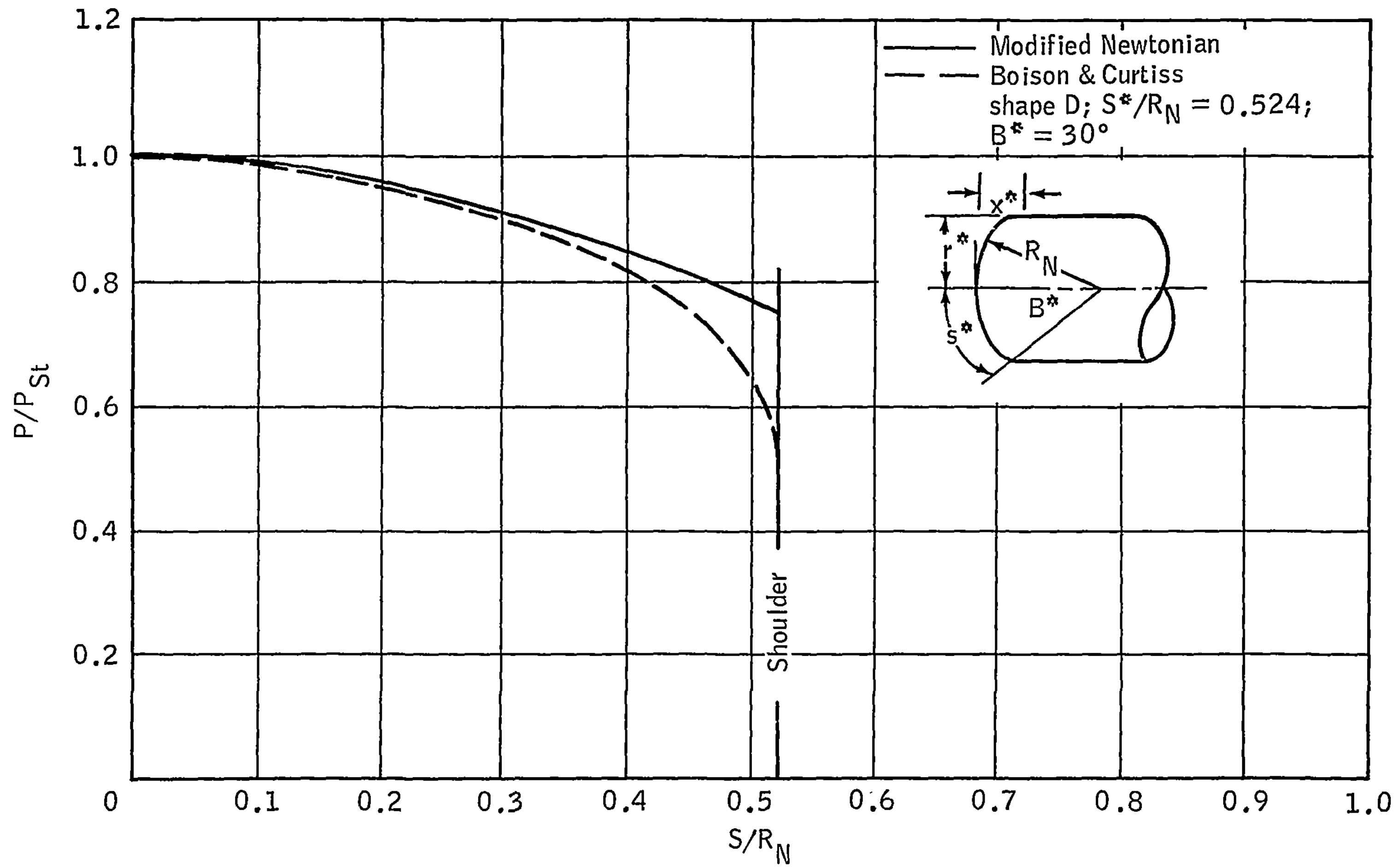

Figure 27. - Comparison of measured pressure distribution over a spherical segment with the modified Newtonian approximation.

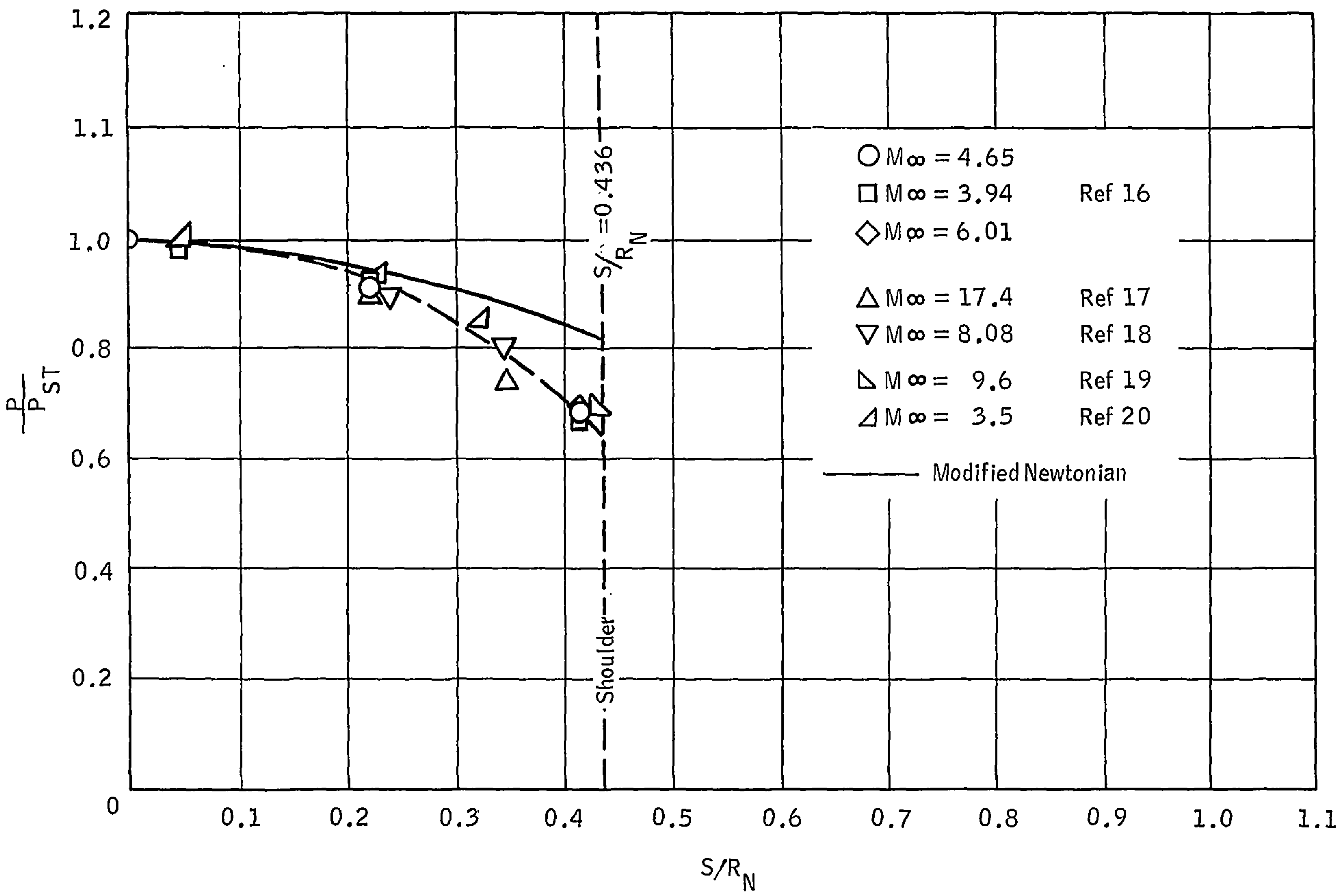

Figure 28. - Compilation of forebody pressure distributions on the project Mercury capsule.

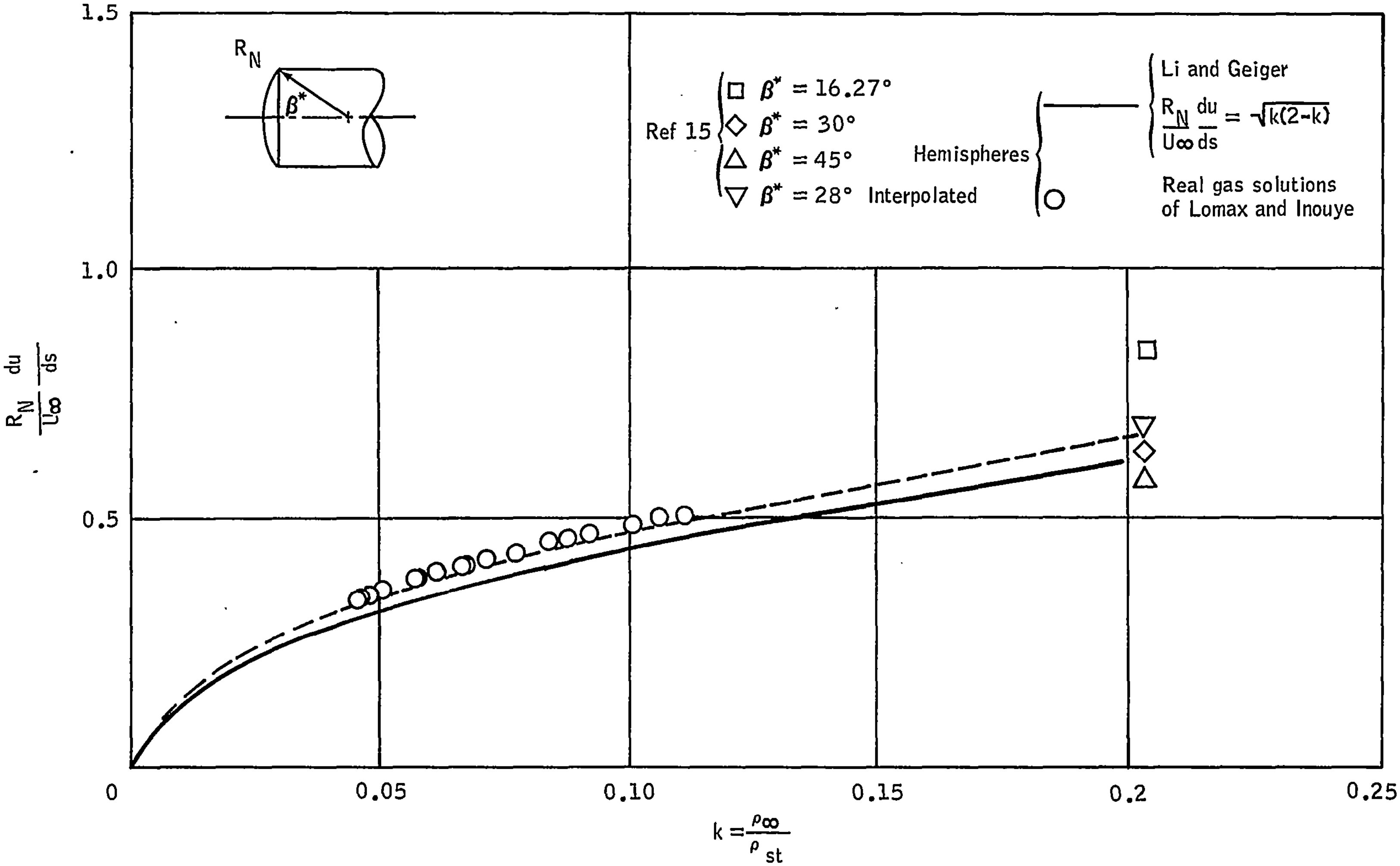

Figure 29. - Stagnation point velocity gradient on sphere and spherical segments.

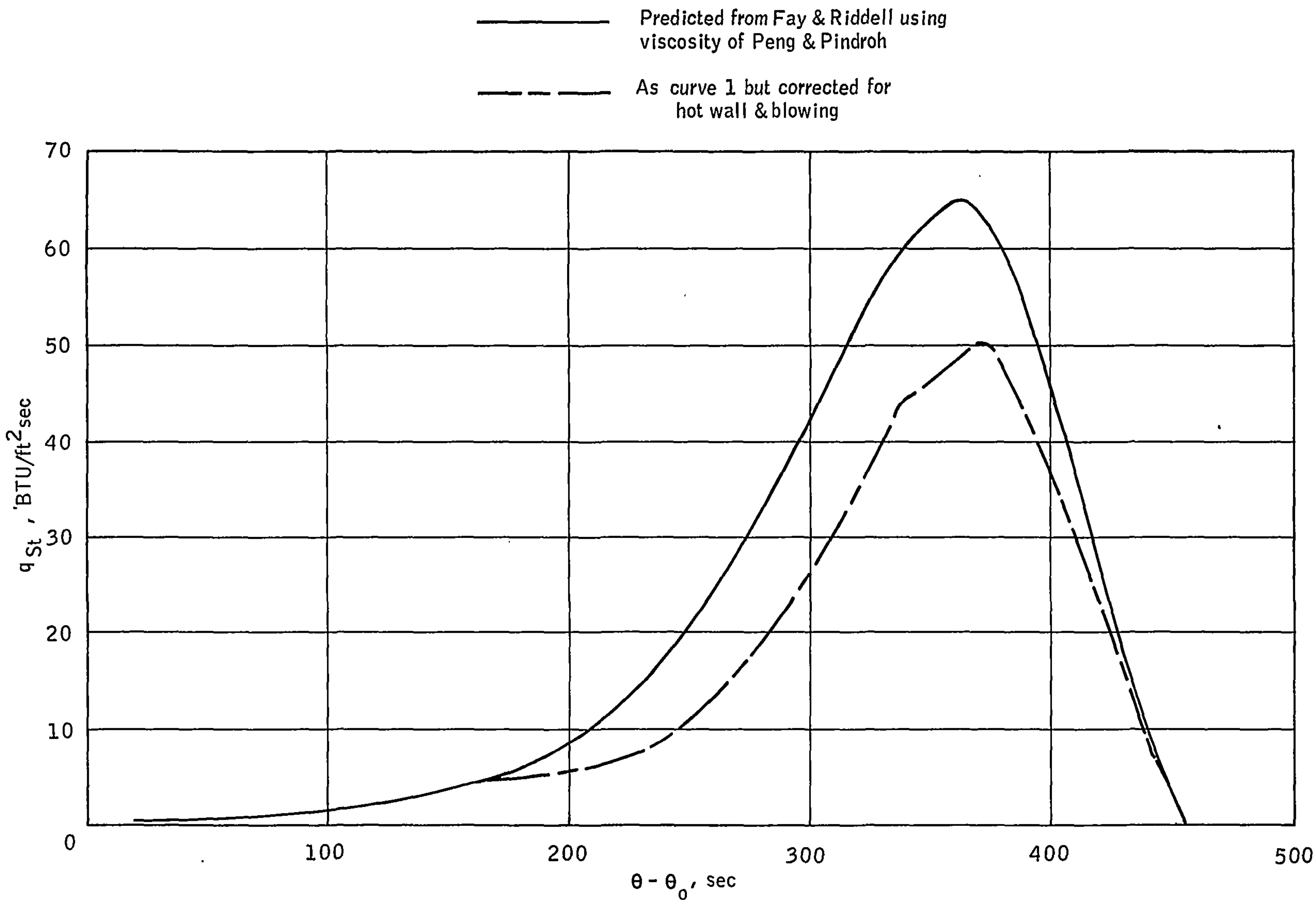

Figure 30. - Predicted stagnation point heat rate history for flight MA-5.

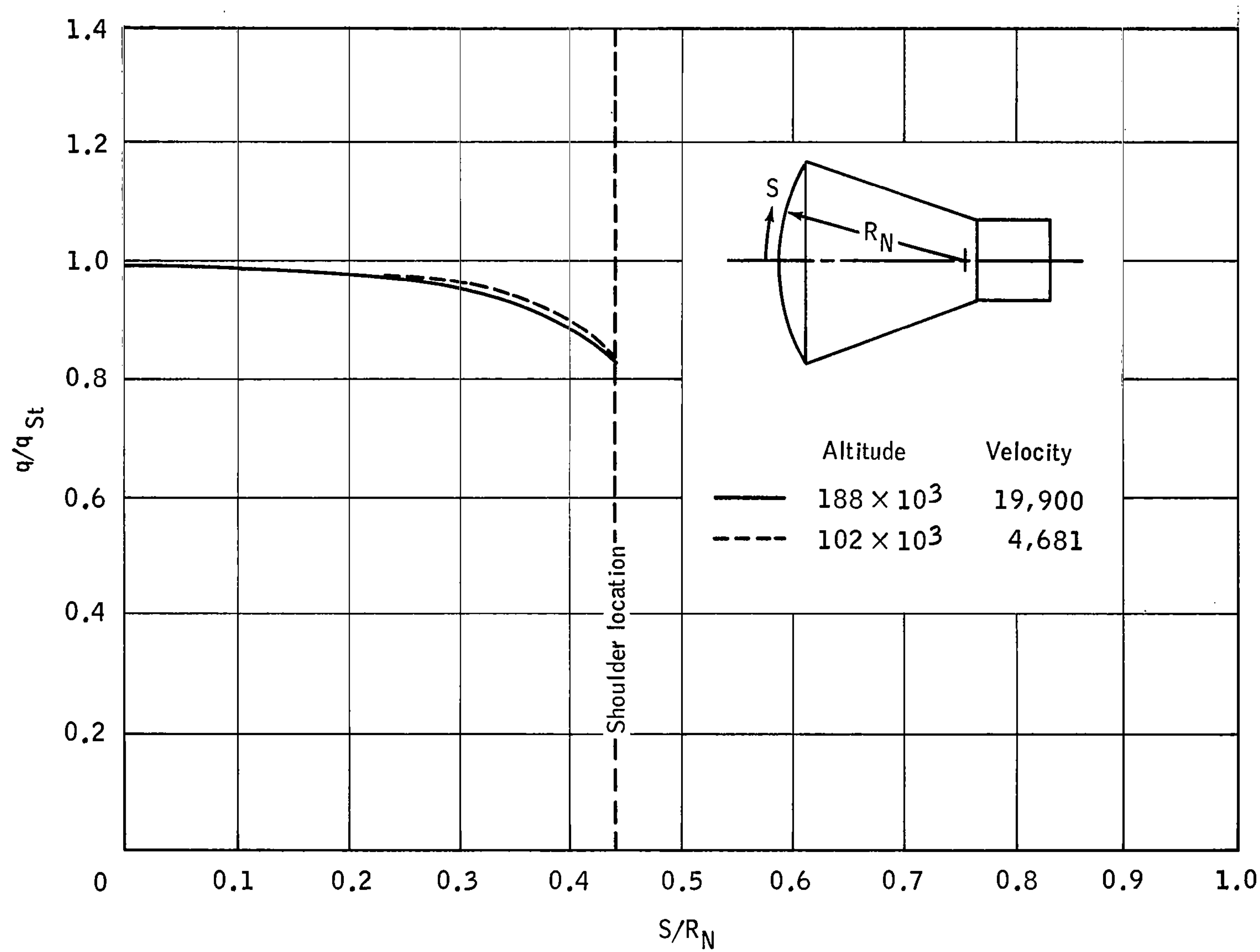

Figure 31.- Predicted distribution of laminar boundary layer heat transfer on Project Mercury capsule forebody ~ no blowing ~ $\alpha = 0$

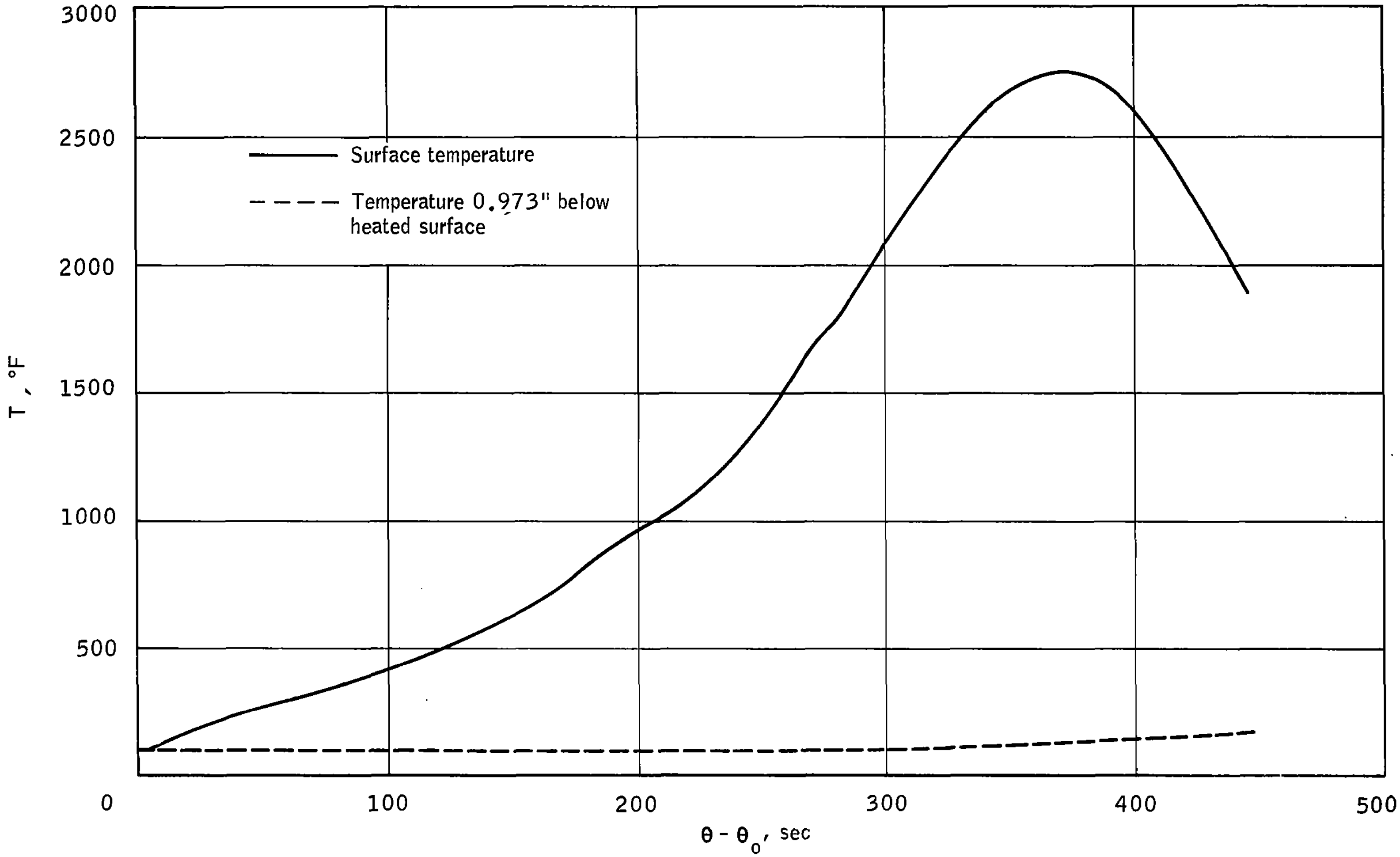

Figure 32. - Stagnation point wall temperature history -mission MA-5.

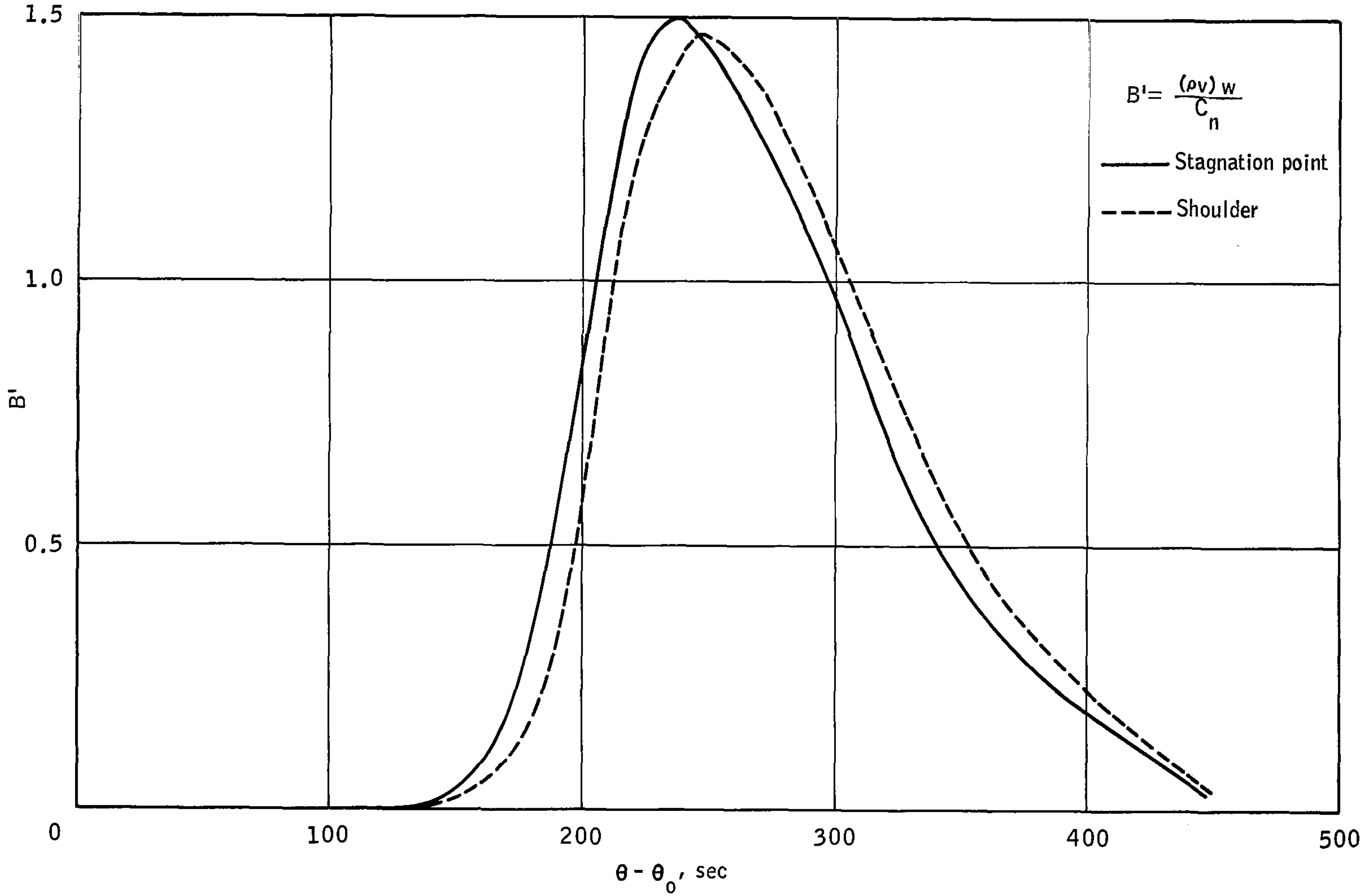

Figure 33. - History of blowing parameter B' for flight MA-5.

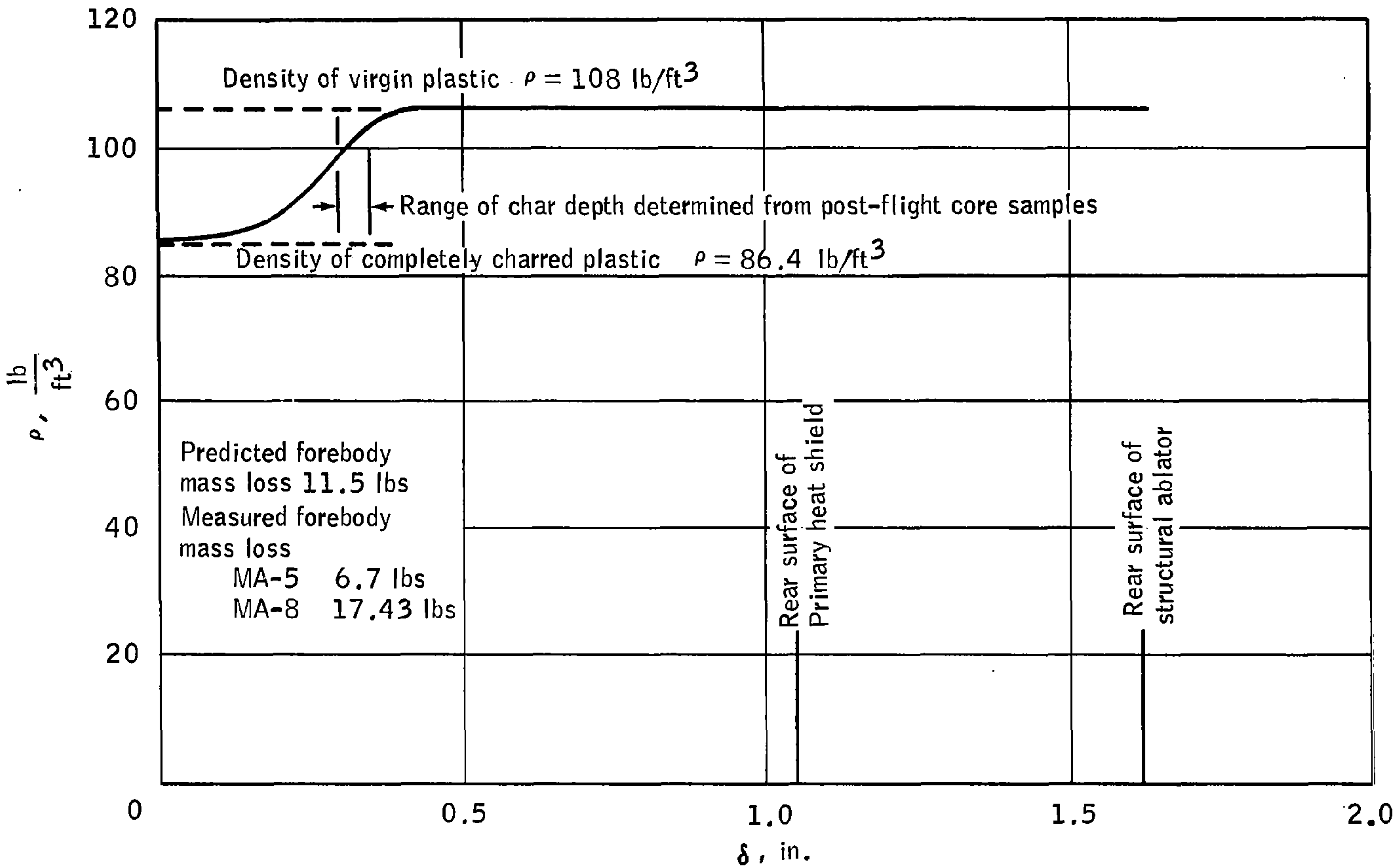

Figure 34. - Distribution of density through the Mercury heat shield at the end of reentry for flight MA-5.

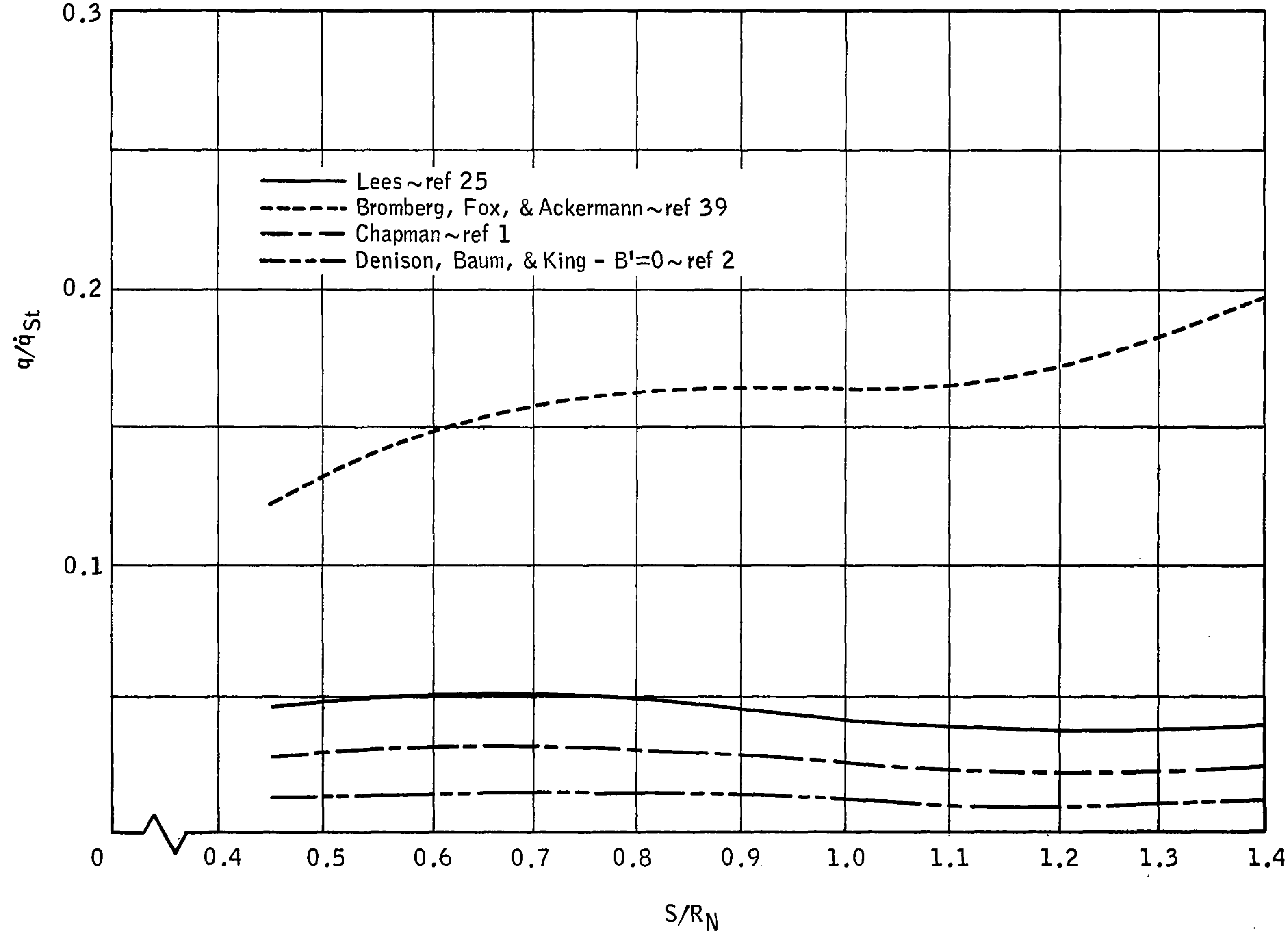

Figure 35.-Comparison of afterbody heat transfer predicted from the several theories - MA-5, $\theta - \theta_0 = 340$ sec.

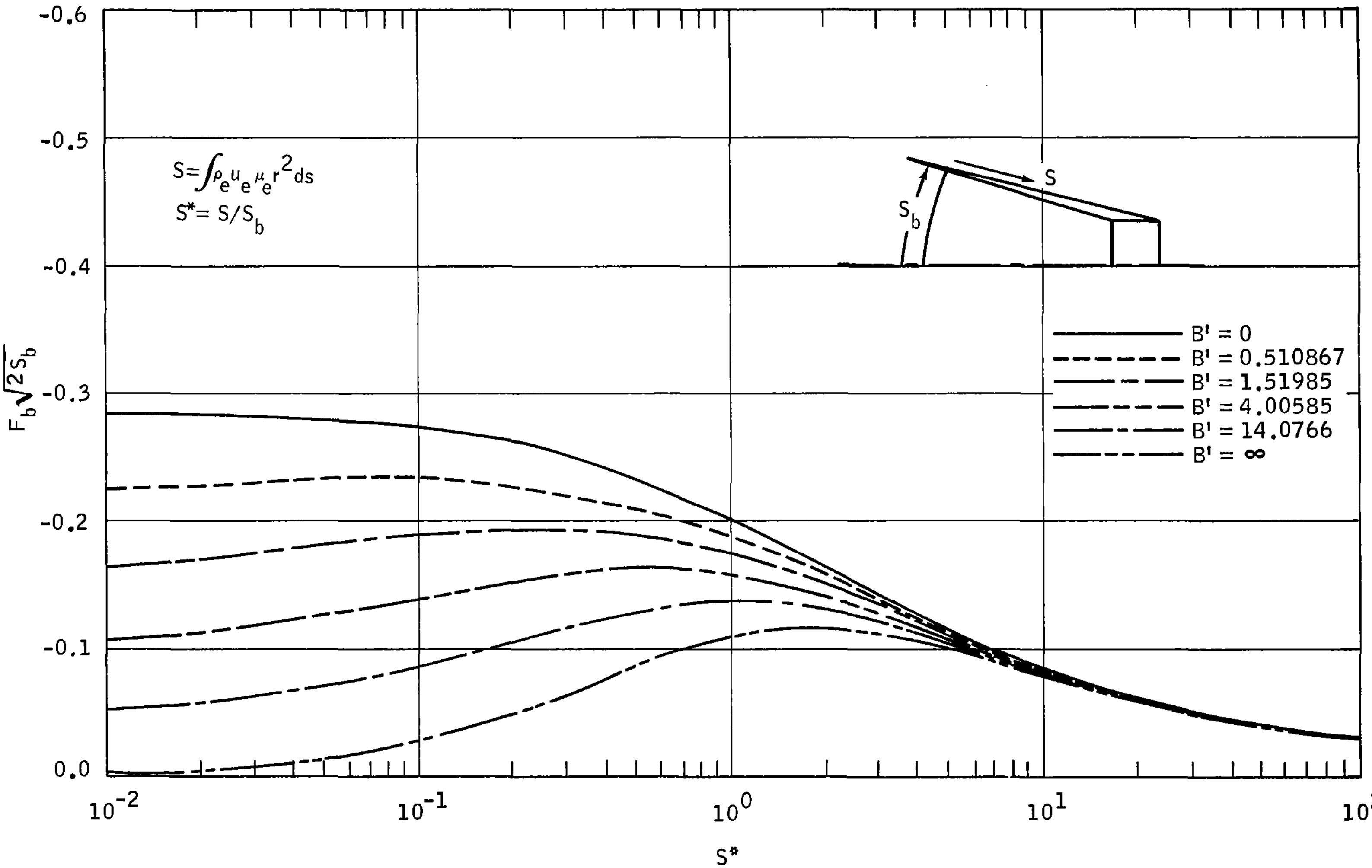

Figure 36. - Dimensionless shear function on the dividing streamline as a function of streamwise distance from separation point for various levels of forebody blowing.

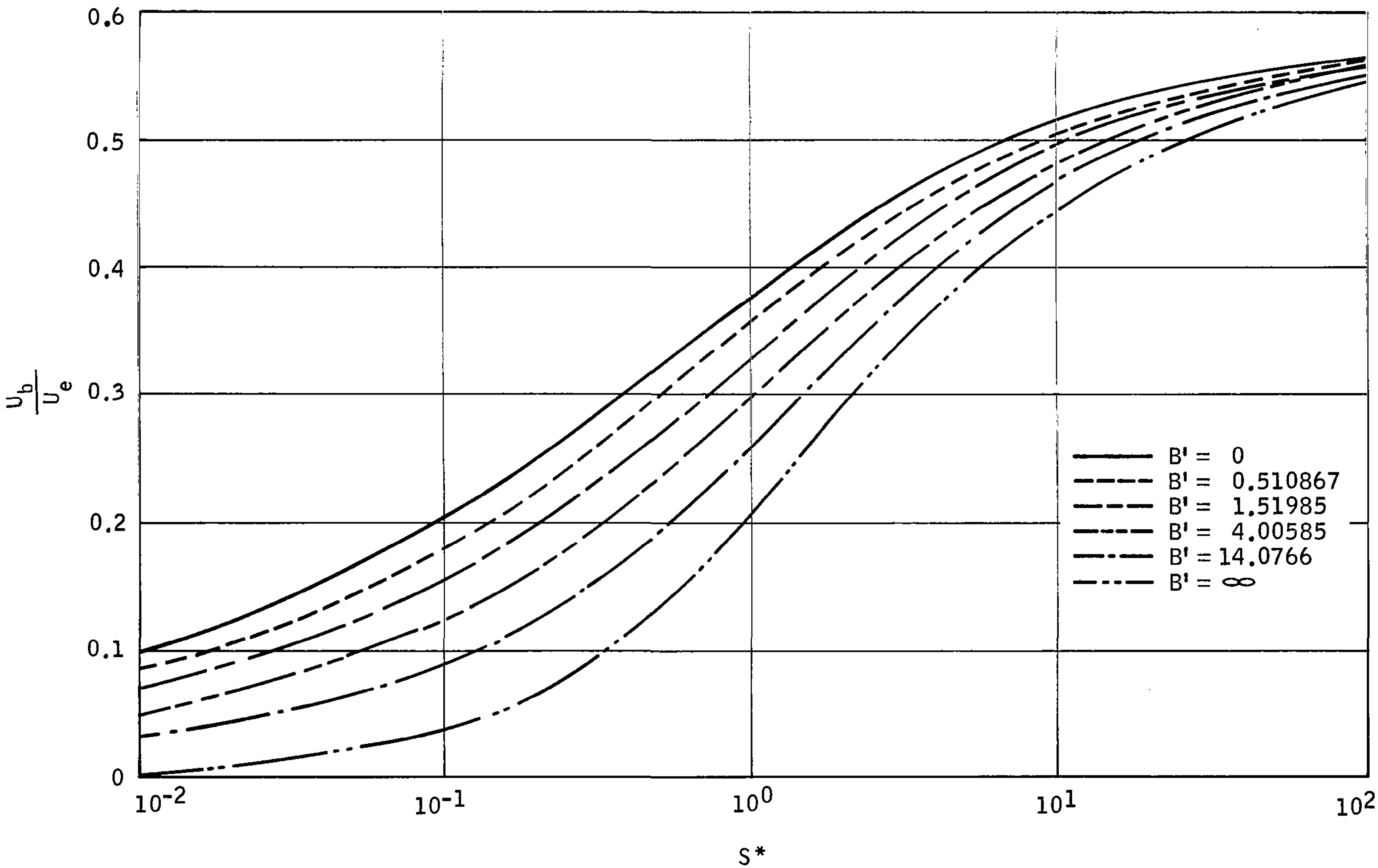

Figure 37.- Dimensionless velocity on the dividing streamline as a function of streamwise distance from separation point for various levels of forebody blowing.

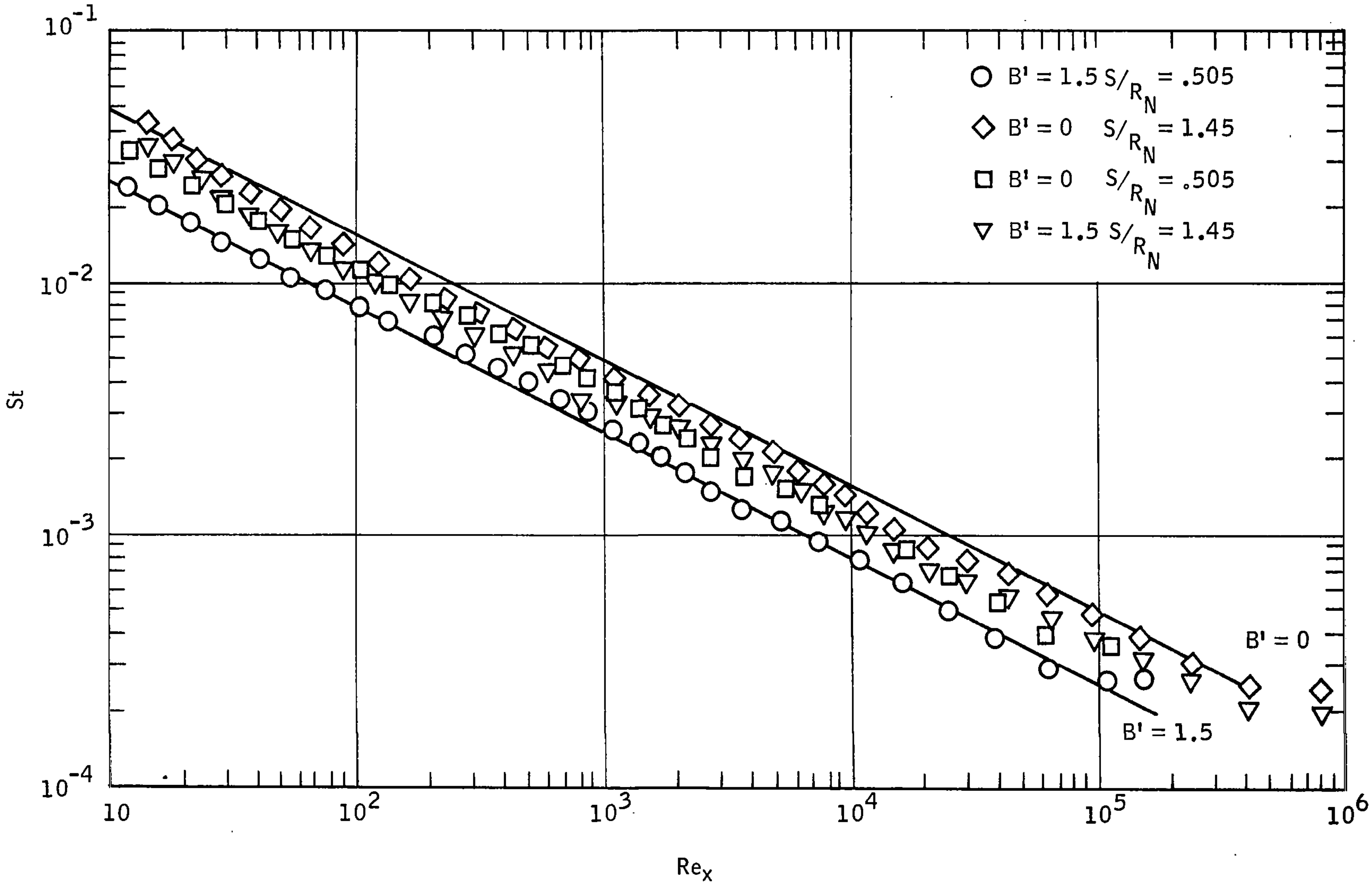

Figure 38. - Variation of predicted Stanton number with length Reynolds number using modified theory of Denison, Baum, and King for trajectory for MA-5.

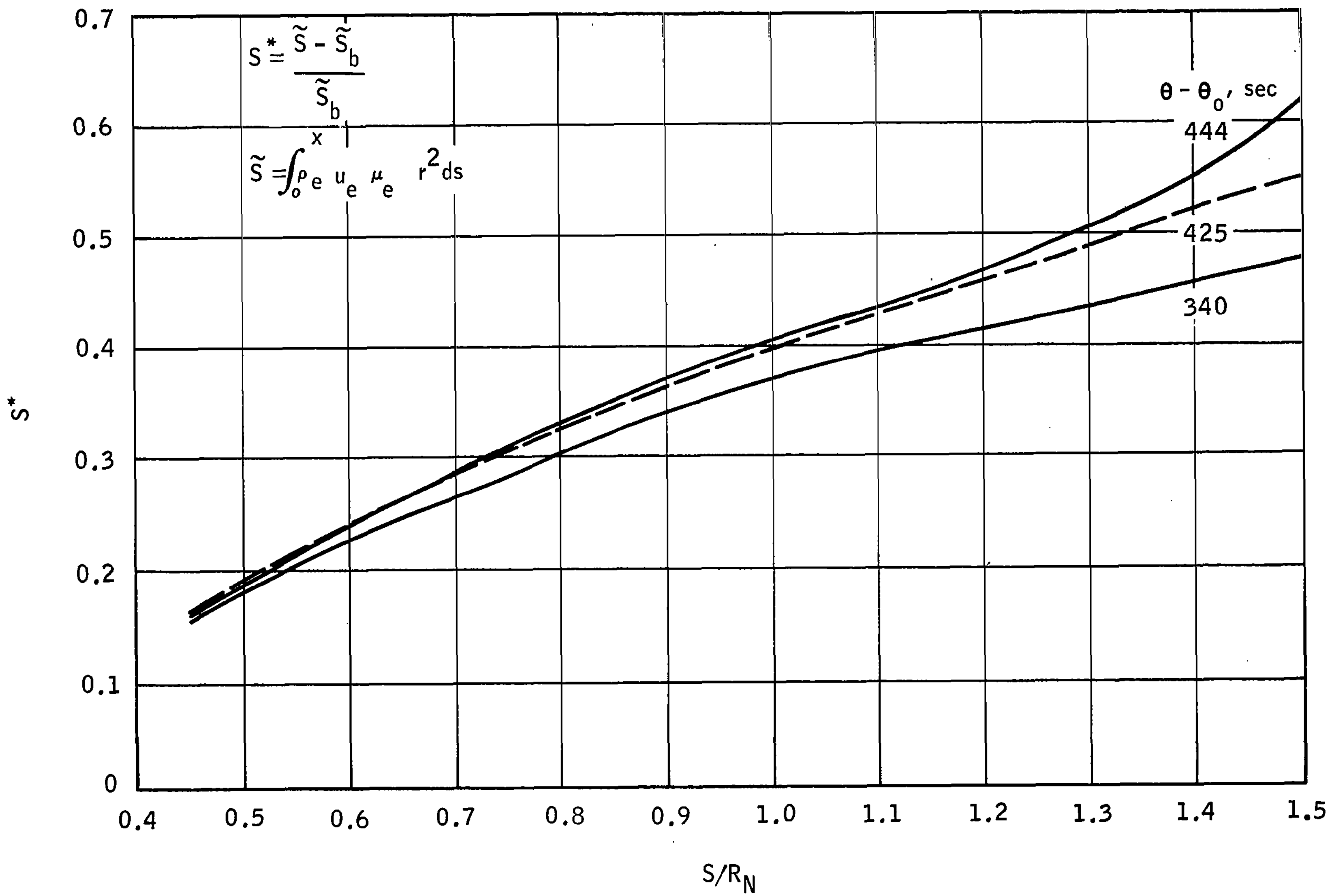

Figure 39.- Variation of S^* with S/R_N for the project Mercury configuration.

NASA-Langley, 1967 — 33